Design, Fabrication, and Assembly of Multi-chip Walking Silicon Microrobots

Hani Gomez

Electrical Engineering and Computer Sciences
University of California at Berkeley

Technical Report No. UCB/EECS-2020-229
http://www2.eecs.berkeley.edu/Pubs/TechRpts/2020/EECS-2020-229.html

December 18, 2020

Copyright © 2020, by the author(s).
All rights reserved.

Permission to make digital or hard copies of all or part of this work for personal or classroom use is granted without fee provided that copies are not made or distributed for profit or commercial advantage and that copies bear this notice and the full citation on the first page. To copy otherwise, to republish, to post on servers or to redistribute to lists, requires prior specific permission.

Design, Fabrication, and Assembly of Multi-chip Walking Silicon Microrobots

by

Hani C. Gomez

A dissertation submitted in partial satisfaction of the

requirements for the degree of

Doctor of Philosophy

in

Engineering – Electrical Engineering and Computer Sciences

in the

Graduate Division

of the

University of California, Berkeley

Committee in charge:

Professor Kristofer S.J. Pister, Chair
Professor Ana C. Arias
Professor Dorian Liepmann

Fall 2020

Design, Fabrication, and Assembly of Multi-chip Walking Silicon Microrobots

Copyright 2020
by
Hani C. Gomez

Abstract

Design, Fabrication, and Assembly of Multi-chip Walking Silicon Microrobots

by

Hani C. Gomez

Doctor of Philosophy in Engineering – Electrical Engineering and Computer Sciences

University of California, Berkeley

Professor Kristofer S.J. Pister, Chair

Microrobots can someday be used as a tool to further expand investigative capabilities– for example, archeologists could use them to research buried cities such as the one in Tiwanaku, Bolivia, or emergency response workers could send robots ahead in search-and-rescue operations. The anatomy of a microrobot can be broken down into its body, brain and power. Typically, each subsystem is fabricated using a different process, creating the need for multi-chip assembly. Microrobots in the literature are often assembled post-process using methods such as wire bonding, silver epoxy, and flip-chip bonding. These approaches tend to be time consuming, tedious and may even harm the devices. Additionally, not all of them provide the necessary mechanical robustness needed for a moving walking microrobot.

This work presents a zero-insertion force (ZIF) socket as a solution to achieving robust electrical, and mechanical assembly of a walking silicon microrobot. The ZIF socket and body of the microrobot are composed of various micro-electro mechanical systems (MEMS) fabricated using a three-mask silicon-on-insulator (SOI) process. First, successful MEMS-MEMS assembly using a ZIF socket is presented, as well as important design considerations. Subsequently, proof-of-concept and first results for MEMS-CMOS assembly is shown, integrating a complimentary metal-oxide semiconductor (CMOS) chip into a ZIF socket. Finally, the full system design of a walking silicon microrobot (not yet fabricated) using the Single Chip micro Mote (SCμM) CMOS chip as a brain, and a solar cell chip (Zappy2) for power is introduced.

To the little girls and children of the world who dream of making the world a better place by becoming engineers, scientists, researchers, and mathematicians. May the child inside us never outgrow our dreams and imaginations.

Contents

Contents ii

List of Figures iv

List of Tables viii

1 Introduction 1
1.1 Defining Microrobots and Potential Applications . . . 1
1.1.1 Miniaturization: A Solution to Macro-scale Problems . . . 1
1.2 Anatomy of a Microrobot . . . 2
1.2.1 The Importance of On-board Power and Control . . . 4
1.3 State-of-the-Art Walking Microrobots . . . 4
1.4 This Work . . . 6
1.4.1 Three-Mask SOI Fabrication Process . . . 7
1.4.2 Process Limitations and Assembly Challenges . . . 8

2 Zero Insertion Force MEMS Socket 9
2.1 System Overview . . . 9
2.1.1 Assembly Process . . . 11
2.1.2 Clamp and Spring Subsystem . . . 13
2.1.3 Latch and Release Subsystem . . . 14
2.1.4 Probe Subsystem and Design . . . 15
2.2 Contact Resistance Characterization . . . 17
2.2.1 Holm's Contact Resistance Model . . . 17
2.2.2 Resistance vs Force Test Structures . . . 18
2.2.3 Results . . . 21
2.3 MEMS-MEMS Assembly and Results . . . 23
2.3.1 Electrostatic Inchworm Motors . . . 24
2.3.2 Silicon Legs and Steps Towards a Walking Microrobot . . . 26

3 Modular Integration Platform for Autonomous Microrobots 31
3.1 MEMS-CMOS Assembly . . . 31

3.2 Components and Specifications for a Wireless System 31
3.2.1 SCμM: Single Chip Micro Mote 32
3.2.2 Zappy2: A Solar-Cell Solution to Wireless Power 33
3.2.3 Parameter Considerations for ZIF Socket Design 35
3.3 First ZIF Socket Designs and Assembly Challenges 35
3.4 MEMS Cassette: a Solution to Vertical Alignment 37
3.5 Modular Silicon Integration Platform for Autonomous Microrobots . . . 40
3.5.1 System Description 40
3.5.2 Methodology and Results 41

4 Walking Silicon Microrobot **46**
4.1 Full System Overview 47
4.1.1 Full System Circuit 48
4.2 Hub Chip 49
4.2.1 Antenna Design 50
4.2.2 Assembly and External Components 50
4.3 Leg Chips 52
4.3.1 ZIF Sockets and Silicon Jumpers 54
4.3.2 Substrate Latches 54

5 Conclusion **59**
5.1 Seven-Mask SOI Process 60
5.2 Microrobot and IoT Researcher Responsibilities and Considerations 61

Bibliography **66**

List of Figures

1.1 The anatomy of a microrobot can be broken into three simple parts: its body [5], power [6] and brain [7] . . . 3
1.2 A silicon walking microrobot with: a) MEMS legs b) a CMOS chip, c) solar cells, and d) a MEMS hub chip for integration. . . . 3
1.3 Five state-of-the-art walking microrobots [16, 17, 18, 19, 5] are compared based on: robot body length, whether it has on-board power, whether is has on-board control, the number of manual assembly parts, and the fabrication process used to create the parts. . . . 5
1.4 Cross-sections of the main steps in the three-mask silicon-on-insulator fabrication process used in this work. . . . 7

2.1 A first iteration of the ZIF socket can be seen on top of a gold coated US penny. 9
2.2 A 3D model of the socket and inserted chip assembly. The red arrows are used to indicate the correlation between the socket in the model and the socket from Fig. 2.1. The inserted chip in this model is a MEMS silicon microrobot leg based on the silicon hexapod legs [5]. . . . 10
2.3 a.) Motor chip and ZIF MEMS socket in their initial, neutral state. b.) Clamp is pulled back and latched. c.) Motor chip is slowly inserted into socket. d.) Chip is inserted all the way into the socket, reaching horizontal alignment between the socket probes and the chip pads. e.) The unlatch structure is engaged: the clamp closes on the chip, providing the system with electrical contact and mechanical integrity. . . . 11
2.4 A top-down microscope image of the ZIF socket and its subsystems at the stage shown in Fig. 2.3b. . . . 12
2.5 A cross-section of the final ZIF socket and motor chip assembly. . . . 13
2.6 A top-down microscope image of the clamp and spring subsystem. . . . 13
2.7 A top-down microscope image of the latch before and after engaging. . . . 14
2.8 A zoomed-in microscope image of the engaged latch from Figs. 2.4 and 2.6. 15
2.9 A top down microscope image of the six probes in the ZIF socket used to electrically connect to the motor chip. Left: the probes before assembly. Right: probes after assembly. . . . 16

2.10 Two scanning electron microscope (SEM) images of a probe tip making contact with a pad. Left: zoomed-out. Right: zoomed-in to tip. 16
2.11 A drawn cross-section of a single ZIF socket probe against one pad on the inserted chip. 17
2.12 A 3D model of the resistance versus force test structures and assembly. a.) Two probes side by side on clamped-clamped beams. b.) A leg chip with pads on side tabs that can be inserted into the device from a). c.) The final assembly of the two chips used to take resistance vs force measurements. . . 19
2.13 A top down microscope picture of the clamped-clamped test structure probes shown in Fig. 2.12a. 19
2.14 A top down microscope picture of the connected pads on the inserted chip. These pads are also on the side tabs of the leg chip in Fig. 2.12b. 20
2.15 A top down representation of the Gold Palladium coated test chips with two probes attached to two beams in parallel. The gray block represents the inserted chip coming out of the page. 20
2.16 A top down microscope image of the AuPd sputtered probes before and after engagement. Notice the reflection due to the orthogonal chip. 21
2.17 Plot of resistance vs force for Tungsten sputtered chips. 22
2.18 Plot of resistance vs force for Gold evaporated chips. The trace resistance is almost equivalent to the Holm's plastic regime resistance, and therefore not easily visible in this plot. 22
2.19 Plot of resistance vs force for AuPd sputtered chips. 23
2.20 a) Microscope image of the Tungsten sputtered pad. The ZIF socket probe scratched against the pad. b) Scanning electron microscope (SEM) image of the Tungsten covered triangular probe tip. c) SEM image of the Gold evaporated pad. 23
2.21 Microscope top-down picture of the linear electrostatic inchworm motor used for the first test assembly setup. 24
2.22 SEM of the motor chip and ZIF socket assembly. 25
2.23 Cross-section of the top-down microscope setup used to see the motor chip and ZIF socket assembly from Fig. 2.22. 26
2.24 SEM of the motor chip and ZIF socket assembly from Fig. 2.22 next to the microscope image of the motor in Fig. 2.21. 26
2.25 A top-down microscope image of the six ZIF socket probes engaged and reflecting off the vertical chip. 27
2.26 Snapshots of a video of the motor shuttle actuated through the ZIF socket. The video was taken using the setup in Fig. 2.24. The measured times and total shuttle displacements are noted. Displacement of the shuttle and the support springs is visible. 27
2.27 SEM image of the ZIF socket probes against the inserted chip pads, with a horizontal misalignment of 20µm. 28

2.28 a.) A microrobot leg similar to the one presented in [36] assembled inside a ZIF socket. The leg is pointing up in this case. b.) A 3D model of the ZIF socket design and robot leg chip assembly seen in part a.). 28
2.29 A picture of the double ZIF socket on a gold coated US penny. 29
2.30 A double ZIF socket chip assembled with a chip containing two silicon legs. 29
2.31 A fully assembled quadruped microrobot using two double ZIF socket assembly subsystems: one for the right legs, and one for the left legs. 30

3.1 The single chip micro mote (SCμM) designed for microrobot control and communication [7, 38]. 32
3.2 Pad alignment measurements for SCμM to assemble with the ZIF socket probes [7, 38]. 33
3.3 Zappy2: the solar-cell and high-voltage CMOS chip designed to power both SCμM and silicon MEMS actuators [6]. 33
3.4 Pad alignment measurements for Zappy2 to assemble with the ZIF socket probes [6]. 34
3.5 The first iteration of a ZIF socket assembled with a CMOS chip. 36
3.6 A cross-section model depicting the vertical misalignment between the SCμM chip pads and the MEMS ZIF socket probes. 36
3.7 A top-down model of the proposed MEMS cassette. 37
3.8 A cross-section model of the proposed MEMS cassette. SOI and substrate are not to scale for the MEMS cassette or ZIF socket. 38
3.9 Top: A 3D model of the SCμM chip in the MEMS cassette. Bottom: A picture of the SCμM chip in the MEMS cassette, which was designed with a MEMS linear motor. 39
3.10 Full MEMS ZIF socket system designed for wireless microrobotic platforms. It can integrate with CMOS chips, solar chips, MEMS motors, and 0402 capacitors. 40
3.11 a) MEMS-CMOS assembly using a MEMS cassette to hold a CMOS chip, inserted into a ZIF socket. b) The system is being held up by a tweezer at one end of the cassette. The two clamps exert enough force on the cassette for the system to not disassemble. 41
3.12 A 3D model of the MEMS-CMOS assembly using a MEMS cassette to hold a CMOS chip, inserted into a ZIF socket. 42
3.13 Top down microscope image of the 32 probe tips and the clamp on the CMOS compatible ZIF socket. 42
3.14 a) The test setup used to confirm alignment between the probes and pads. The 45º mirror is slightly angled with tape to be able to see the connection. b) The engaged ZIF socket probes after assembly. The probe tips at the top of the image are simply the reflection of the vertical CMOS chip. c) Microscope image from the setup in a). The SCμM pads are 53μm by 65μm pads on an 80μm pitch. The image is shown in grayscale to more easily recognize the probes. 43
3.15 A schematic of the setup used to read a CLK signal from the SCμM chip. . . 44

3.16 The 3.6MHz clock signal seen out of SCμM's GPIO 12 pin. 45

4.1 A 3D model of the walking silicon microrobot designed in this chapter. All the 3D renderings in this chapter were made using Blender. 46
4.2 A copy of the 3D model in Fig. 4.1 with each individual component labelled. 47
4.3 A complete electrical circuit schematic for the walking microrobot system. . 49
4.4 3D Model: A top down view of the hub chip without external components. . 50
4.5 3D Model: A top down view of the device layer antenna on the hub chip, designed to connect to SCμM. 51
4.6 3D Model: A top down view of the hub chip with the assembled external components and two leg panels. 51
4.7 3D Model: A top down view of the bottom portion of right leg panel. 52
4.8 A drawing of the foot cross-section, A-A' from Fig. 4.7. 53
4.9 3D Model: A top down view of the sockets, probes and assembly latches designed into the right leg. Top: before assembly with the hub chip. Bottom: after assembly with the hub chip, SCμM and Zappy2. 55
4.10 Left: a microscope picture of a fabricated latch. Right: a corresponding schematic. The 40μm gold marking indicates that the beam width of this latch was designed as 40μm wide. 56
4.11 Left: a camera picture of the fabricated latch test structures, with the first latch engaged. Right: a microscope image of the bottom ends of the first latch poking through the hub chip, as well as reflecting off of it. 56
4.12 A summary of the results from testing the latch test structures. 57
4.13 A plot of the calculated strains and theoretical applied forces on the latches vs the increasing latch beam widths. 58

5.1 A step-by-step cross section of the seven-mask SOI process designed to add an additional routing and device layer, part 1. 62
5.2 A step-by-step cross section of the seven-mask SOI process designed to add an additional routing and device layer, part 2. 63
5.3 A step-by-step cross section of the seven-mask SOI process designed to add an additional routing and device layer, part 3. 64
5.4 A step-by-step cross section of the seven-mask SOI process designed to add an additional routing and device layer, part 4. 65

List of Tables

4.1 Summary of system payload. 48

Acknowledgments

I am not self-made. I am the product of the support given to me by my community, of the hard work of the generations that came before me and of those currently around me. I apologize if I have missed anyone, I appreciate you nonetheless!

Thank you to Kristofer Pister, for being a supportive and welcoming advisor from the first time I ever visited UC Berkeley. Never before had I allowed myself to imagine the possibility of working on technology as cool as microrobots. Thank you for making it a possibility and challenging us to grow into the engineers that we can become.

Thank you to my dissertation and qualifying committee members, professors Ana Arias, Ming Wu, and Dorian Liepmann for your support throughout the last few years. Especially thank you to Ana Arias for, perhaps unknowingly, being a role model I could look up to all these years– to inspire me to keep going when things felt too difficult.

Thank you to the National Science Foundation and the UC Berkeley Chancellor's Fellowship, for funding my education the last five years and making all this possible. Thank you to the Marvell Nanofabrication Laboratory staff and engineers, for your constant support, patience, and understanding. It was a privilege to be able to work with such a helpful and kind team of engineers and scientists in a clean room with a view of the Golden Gate Bridge.

Thank you to the Pister group for the friendships we have formed and the experiences we have shared.

Thank you to Craig Schindler, for always being there. Thank you for being not just a research colleague but also a friend, an ally, and a partner-in-crime. Thank you both Craig and Brian Kilberg for making the normally lonely PhD experience so much more enjoyable and fun. Thank you for the fun we had in Swarm Lab with Enrique, for everything you have taught me, and for always being willing to help.

Thank you to Alex Moreno for the daily virtual writing sessions, for pushing me to keep writing as we go through a global pandemic so that I can graduate. I really appreciate you! Thank you to Alexander Alvara, for reminding me to keep dreaming big and to plan ahead, for showing me how to show extraordinary resilience and courage during some of the most arduous times. Thank you to Nathan Lambert for the weekly check-ins on Slack, and showing me I had another friend in you. Thank you to Lydia Lee for always being so kind and caring.

Thank you to Joey Greenspun and Dan Contreras for being my mentors and teaching me everything you know. I appreciate all of your time and value your friendships. Thank you to David Burnett, Fil Maksimovic and the rest of the generation of Pister students that came before me for the advice, knowledge, friendship and support all these years. Thank you to Wei Li, Rachel Zoll, Daniel Teal, Dillon Acker-James, Ahad Rauf, Lizzette Corrales, Meera Lester, Harry Clark, Austin Patel, Felipe Campos and the other undergraduate students that worked with me. You all taught me to see technology, research, and the world in new and fresh ways.

Thank you to my Swarm Lab and EECS friends including Travis Massey, Maggie Payne, Alyssa Zhou, Austin Murdock, Oliver Chen, Arda Ozilgen, Josh Kay, Leticia Ibarra, Claire Lochner, Jodi Loo, Stefanie Garcia, and Sahar Mesri for keeping me company and supporting

me with kind words, chocolate, tea, and sweet notes. Thank you to Carlos Biaou, and JP Llinás for always being such good friends to me, for guiding me through the pains of graduate school, and for helping make my time at UC Berkeley as welcoming and comforting as possible.

Thank you to Sheila Humphreys, Audrey Sillers, Shirley Salanio, and Meltem Erol. The four of you have all had a large impact on my graduate career and the last few years of my life. Thank you for always making me feel welcomed and like I not only belonged, but also deserve to be where I am. Thank you to professors Armando Fox and Dan Garcia for being role models to me and the Latinx community.

Thank you to Bias Busters, for the work I did with the organization many times was one of the few things keeping me going and motivated. Thank you to Regina Eckert, Alyssa Morrow, and Esther Rolf for the strong friendships, venting sessions, and party times.

Thank you to LAGSES, Humberto Bátiz, Gabriel Lopez and the outreach team members Dana Hernandez, Daniel Ocasio, Miguel Rodriguez for providing me with a Latinx community that I can be a part of. Thank you to Edy Cardona for being one of my best friends, for always being there for me and being willing to listen. I really cherish our tea time together.

Thank you to my Mami for everything she has ever done for me. I know I wouldn't be here without you, and I could have not asked for a better, more loving and kind mom. Te amo mami. To my sister Flor, gracias por todo! You are my soul sister, my best friend, and have helped me so much to get here. I am so proud of you and everything you have accomplished. Thank you to my partner Natan for always being there for me, especially the last few months trying to graduate. You have shown me unconditional love and support beyond measure, and I appreciate you so much.

Thank you to my cousin Kevin and Danny, for all the fun times, love, and support you gave me the last few years. Thank you to my grandpa Kent and grandma Laura for helping fund and support my education. I wouldn't be here without you. Thank you to my aunt Lori and grandma Roxie for the phone calls, therapy sessions, and love and acceptance. Thank you to my aunt Erin, aunt Connie, uncle Tom, uncle Doug and younger cousins for being such a loving family. Thank you to cousin Harry Grant and his daughter Allie, for welcoming to California when I first moved here and being my family. Gracias a mi tia Majue por todo tu apooyo y todo lo que has hecho por mi. Gracias a mi tia Vicky, mi tio Juanqui, y todos mis primos en Bolivia por su cariño y apoyo. Gracias a Eliana Peracchio, por el amor y la amistad incondicional.

Thank you to Linabel Zhou, Xixi Zhou, Allen Bates, Cristian Gonzales and Alex Rutherford for being such caring and supportive long distance friends. I hope our adventures keep bringing us back together until we are wrinkled and gray-haired. Gracias a las bisses! Thank you to Adriana Pierola, Gabriel Armijo, Nathy Correa, Santiago Murillo, Valeria Olguin, y Adriana Avila por todas las llamadas, las risas, y el apoyo que me han dado los últimos años. Las quiero bisses.

Thank you to Maddie Meyers for showing me how to live life to the fullest, and thank you Cara Bailie for being a caring and loving friend. Thank you to Josh and Jessie Tindal, Jay Robinson, Myra Robinson, Jordan Rogers and the rest of the Circle for the late nights in

lab, the delicious southern food, and the welcoming southern charm. South Carolina will always be my home and in my heart.

Thank you to professor Gabi Kuenzli for all of your advice and support the last few years. Thank you for pushing me to be better and work harder. Thank you to Mr. Metts, and my undergraduate research advisors Dr. Chandra and Dr. Dougal for helping me achieve my dreams. Especially thank you to Dr. Chandra, for I would have never allowed myself to dream of earning a PhD if you had not believed in me.

Chapter 1

Introduction

1.1 Defining Microrobots and Potential Applications

As large scale automation has proven to be an inevitable path for many industries, this work explores a smaller-scale alternative towards the future of automation. Industrial robots are often used in manufacturing, to reduce labor costs and increase accuracy and precision. Even though useful in these industries, the size of large-scale robotics can be a disadvantage: they are likely to take more material, power, and a higher cost to build. More importantly, there are problems that only smaller (micro) robotic systems are able to resolve. For example, a swarm of microrobots could help archaeologists explore a newly found ancient site much faster and more delicately than they are currently able to. Section 1.1.1 discusses other applications for microrobots.

This dissertation defines microrobots as millimeter to centimeter scale systems, with minimum features in the micrometer scale. To provide an idea of scale, the average diameter of a human hair is 50-100 microns (µm) [1, 2]. The smallest feature used in this work is 2 microns. Such small systems can be connected and used in swarms, to establish mobile sensor networks, etc. Their small size is an advantage: they have a reduced mass and power load, they can crawl into smaller spaces, and if mass produced, their cost could be significantly less than that of current state-of-the-art robotic systems.

The ability to mass produce small, sub-10 centimeter robots that can walk, fly, jump, crawl, or swim, first yields the question to the imagination, "If I had a hundred robotic 'insects' that I could control, what would I do?". The answers thus far, have been limitless. The subsection below is not an extensive analysis, but merely a brief introduction to the futuristic visions of this work.

1.1.1 Miniaturization: A Solution to Macro-scale Problems

One of the most prominent examples of useful applications for microrobots presented in the field is search and rescue. This section goes into a specific example where microrobots would have been extremely beneficial, and then presents a second potential application to

use the robots. In 2010, a large earthquake collapsed a mine located in the Atacama Desert of Chile, trapping 33 miners 700 meters underneath the surface [3]. For 17 days, the miners survived rationing emergency supplies with no contact from the world above. After the 17 days, communication was possible through small holes, as well as food and supply delivery. However, it still took a devastating 69 days after the first collapse for the miners to be rescued [3].

Swarms of microrobots working together and communicating with each other at the same time have the potential to be used in disasters such as the one in Chile. Microrobots are able to crawl through much smaller spaces. Sensors, cameras, and an untethered system would give them the ability to collect the necessary information for exploration. Wireless communication capabilities among the robots would allow them to explore a large area deep into the ground and still be able to send signals all the way back to the surface in a timely manner. Microrobots could someday search for life after a disaster much faster than we are currently able to.

Although common, search and rescue is only one motivation for microrobot exploration. Another exciting example is applying the exploration skills to conduct archaeological research. Currently, archaeological research is conducted in horizontal or vertical excavations. A variety of archaeological excavation methods exist to help researchers unearth artifacts in a methodical way. For example, sites can be dug vertically in arbitrary levels (where soil is dug in 5cm, 10cm, or 20cm levels), or using "cultural" levels that depend on the site characteristics and exist naturally [4]. While these levels are predefined in the field to help prevent damaging any artifacts, they are not always cautious enough. Additionally, robotic systems are not often used to ensure that excavation can be done carefully and without having to use arbitrary levels. Microrobots could someday conduct large-scale surveying of buried pyramids, tunnels, and other archaeological sites before excavation. Robots with mechanisms such as grippers on them could be used to perform delicate digging in field. To perform any of the tasks described in this section, microrobots must be small, untethered, and easy to assemble, in order to be able to build not just one, but an entire team of them.

1.2 Anatomy of a Microrobot

The anatomy of a microrobot can be broken into three subsystems: body, power and brain, Fig. 1.1. The body of a microrobot can be defined as: 1) any actuator system used to produce the necessary forces and motion for the robot to move, 2) any sensing structures/systems that help provide information about the robot, and 3) any assembly or supporting structures that keep the robot pieces together in its (ideally robust) 3D form, such its "skeleton". In this work, the body of a microrobot is composed mainly of silicon, the actuators are silicon micro electro mechanical system (MEMS) motors, and every piece of the body is made using a fabrication process discussed further in this chapter. The power aspect of a microrobot is essential to provide the necessary energy for the sensors and actuators, as well as any other non-MEMS chips. The target power source for the microrobots in this dissertation is a

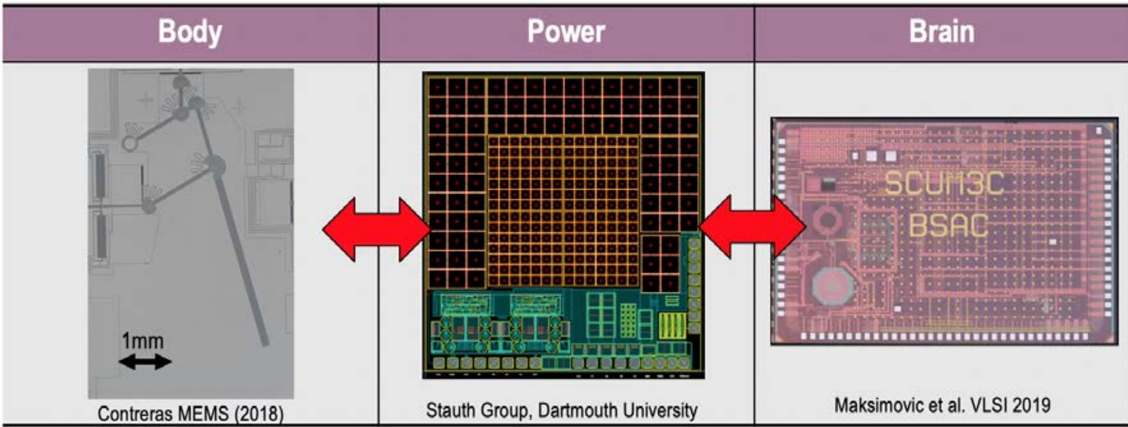

Figure 1.1: The anatomy of a microrobot can be broken into three simple parts: its body [5], power [6] and brain [7]

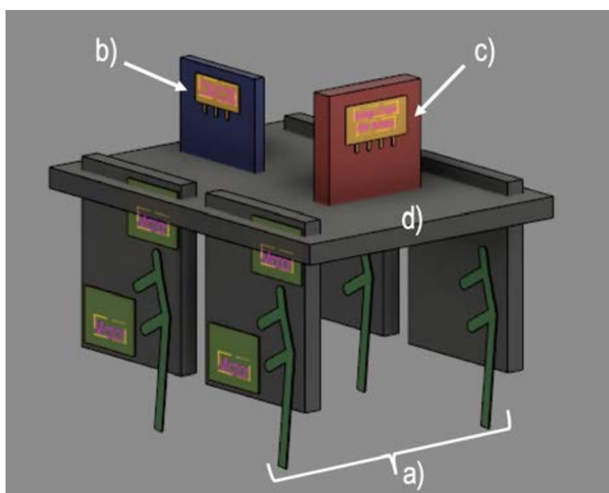

Figure 1.2: A silicon walking microrobot with: a) MEMS legs b) a CMOS chip, c) solar cells, and d) a MEMS hub chip for integration.

solar cell chip [6]. This chip was designed keeping microrobot electrical requirements and mechanical assembly in mind. Finally, a complimentary metal-oxide semiconductor (CMOS) chip can be used for control and communication. This CMOS chip takes the role of the "brain" of the robot: it can receive feedback and external signals to make decisions and specify the actions that each body part takes. This work uses the Single Chip micro Mote (SCµM) [7]. Design specifications and parameters of both the power and brain chips are further discussed in sections 3.2.2 and 3.2.1.

The ultimate goal of this work is to design microrobot components and integrated systems in ways that enable us to assemble them as easily as one can assemble Lego toys. Not only is it necessary to assemble MEMS chips into 3D structures, but these chips must also be

integrated with the CMOS and solar cell chips mentioned above. All three types of chips are made in different, usually incompatible, fabrication processes. In summary, the goal of this work is to create an autonomous walking microrobot, as shown in Fig. 1.2 with: a) four silicon MEMS legs, b) a CMOS chip for communication and control, c) a solar cell chip for power, and d) a central hub chip that helps connect all the parts mechanically and electrically.

1.2.1 The Importance of On-board Power and Control

To travel long distances and achieve the tasks mentioned in section 1.1.1, a microrobot must ultimately be completely autonomous and not dependent on external power or control sources. More importantly, due to the small size and weight of a microrobot, even a small wire tether (used to connect external power or control) is stiff enough to easily affect its motion dynamics [8, 9, 10]. To avoid any negative effects caused by wire tethers, and in addition to being able to move, a microrobot must also have on-board power and control.

Although the model in Fig. 1.2 has wireless solutions for power, control and communication, it is effectively still a "tethered" microrobot. In this design, every piece of the robot relies on the solar cells for electrical power, which is only produced when provided with enough solar power. Therefore, the robot is "tethered" to a light source. This is not an uncommon practice in the literature: similar approaches have been used to show liftoff in jumping, flying, and walking microrobots [11, 12, 13, 14]. However, it is important to acknowledge that these methods greatly limit the robot's mobility to staying within that light source, not to mention the ability for any robot to travel in small, dimly lit tunnels/holes underground. A viable solution to this would be to store the solar cell energy in a battery. Current work is being done to miniaturize batteries, using stencil printing and a based sealing method for packaging by Toor et al. [15]. These batteries are being specifically developed for microrobots, offering a promising solution to the current solar tethered microrobot described in this dissertation.

1.3 State-of-the-Art Walking Microrobots

As previously discussed, the strong potential of microrobots is based not only on their ability to perform small and precise tasks, but also in their numbers and ability to work together. One microrobot might be easily squashed by a shoe. Collectively, a thousand microrobots could someday pick up a human being. To achieve this goal, batch fabrication and production are essential. Currently, not one standard process and assembly method exists to build microrobots.

To more effectively analyze where the state-of-the-art microrobot research is in achieving batch fabrication and production, five metrics can be used. These are: 1) robot body length, 2) whether it has on-board power, 3) whether is has on-board control, 4) the number of manual assembly parts, and 5) the fabrication process used to create the parts. Based on these five metrics, the ideal microrobot would be as small as possible (sub-centimeter), have on-board power and control, be composed of as few parts as possible to simplify assembly, and

Current Microrobots	Goldberg IEEE RA-L (2018)	Qi MEMS (2017)	Vogtmann MEMS (2017)	Pierre Hilton Head (2018)	Contreras MEMS (2018)
Body Length [mm]	45	20	4	2.5	13
On-board Power	✓	✓	✗	✗	✗
On-board Control	✓	✗	✗	✗	✗
Manual Assembly Parts	16	23	7	5	5
Fabrication Process	Pop-up MEMS	Laser cutting & machining	Through-wafer Si, PDMS process	3D printed	Three-mask SOI process

Figure 1.3: Five state-of-the-art walking microrobots [16, 17, 18, 19, 5] are compared based on: robot body length, whether it has on-board power, whether is has on-board control, the number of manual assembly parts, and the fabrication process used to create the parts.

be fabricated in a standard process that could easily be translated into a batch fabrication process. Five state-of-the-art walking microrobots [16, 17, 18, 19, 5] are compared in Fig. 1.3.

The smallest design that includes on-board power and control is HAMR-F [16], a 4.5 cm four-legged robot that also carries a battery. The robot chassis and legs were fabricated using a non-standard pop-up MEMS process, and integrated with piezoelectric actuators and printed circuit boards (PCBs) for power, feedback sensing, control and communication. Even though the slightly larger size of the robot parts could make manual assembly easier, 16 different pieces still need to be assembled to build one HAMR-F. This is the second highest number of assembly parts among all five robots, and it is also the largest robot discussed.

Less than half the body lengh of the HAMR-F is the "electrostatic crawling insect" [17], a 2 cm six-legged microrobot that uses electrostatic actuation and sacrifices on-board control for its smaller size. This robot is manually assembled using 23 laser cut and machined parts, the highest number of parts among all five. Even though it technically has on-board power, this is defined as a single on-board capacitor that can be charged enough to enable the robot to crawl for up to 10 seconds.

At even smaller robot body lengths, it is clear that external magnetic actuation of microrobots becomes increasingly popular. Two great examples of sub-centimeter magnetic microrobots are a silicon and polydimethylsiloxane (PDMS) six-legged microrobot [18]

and a 3D printed four-legged microrobot [19], from Dr. Sarah Bergbreighter's lab. The silicon/PDMS microrobot is 4 mm long, has only 7 manual assembly parts, and is made using a non-standard through-wafer silicon and PDMS process. Further pushing size limits, the four-legged robot is a mere 2 mm, the smallest robot discussed. It also has only 5 assembly parts, which were 3D printed. Although both of these microrobots are no doubt pushing the size limits of this research, one indisputable downfall of the design is the method of actuation. Both robots are magnetically actuated, but do not have any on-board power or control: an outside magnetic field interacts with magnets in the robot legs. While this is still very useful in the field of medicine and other short distance applications, as long as microrobots remain tethered to power, control or communication sources, they will not be able to achieve the tasks described in section 1.1.1.

The HAMR-F and "electrostatic crawling insect" designs are much closer to achieving autonomy, but they are larger than desired and not made in standard fabrication processes. On the smaller end, magnetically actuated microrobots are made also using non-standard processes. However, at those sub-centimeter scales, on-board power and control are much more challenging to implement, and designs are normally confined to remaining tethered. One last, but not least, robot to study is a six-legged silicon hexapod [5] assembled using also only 5 parts made in a standard MEMS process. The robot parts were fabricated using a standard three-mask silicon-on-insulator process, described in detail in section 1.4.1 below. With a body length close to sub-centimeter, a low number of assembly parts, and the ability to fabricate it in a standard process, this silicon hexapod design has the highest potential to be one day batch fabricated and mass produced.

1.4 This Work

This dissertation focuses on developing new methods and designs for the assembly of a full-system silicon quadruped. Also using a standard three-mask SOI fabrication process, this work focuses on learning from the previous silicon hexapod [5] to achieve this goal. In chapter 2 of this dissertation, the zero insertion force (ZIF) MEMS socket is introduced as a solution for both MEMS-MEMS and MEMS-CMOS assembly. Chapter 2 describes the ZIF socket system and design, the new assembly method developed, contact resistance characterization of the socket, and MEMS-MEMS assembly and results. After confirming successful MEMS-MEMS assembly, Chapter 3 discusses the challenges, methods and results involved in integrating MEMS-CMOS systems. With both successful MEMS-MEMS and MEMS-CMOS assembly methods, Chapter 4 goes over the design, assembly and results of a full-system silicon quadruped microrobot. Finally, Chapter 5 concludes the dissertation by introducing a new potential fabrication process for improved microrobot design and discussing other future work.

1.4.1 Three-Mask SOI Fabrication Process

Cross-sections describing the three-mask SOI fabrication process used in this work can be seen in Fig. 1.4. The fabrication process used in this work is based on the standardized MEMSCAP SOI process, SOIMUMPs [20]. However, all of the fabrication was conducted in house at the UC Berkeley Marvell Nanofabrication Laboratory. The process begins with a bare SOI wafer that has a 40 micrometer (µm) SOI or device layer, a 550µm substrate, and 2µm of buried oxide in between. Both the device layer and substrate are single crystal silicon. The first pholithography step in the process utilizes the /METAL mask, after which a 550 nanometer (nm) stack of chrome-gold is evaporated and patterned using lift-off. Then, after the second photolithography step (/SOI mask), deep-reactive ion etching (DRIE) of silicon is used to anisotropically etch the patterns into the 40µm device layer. Similarly, DRIE of silicon is used to etch the /TRENCH mask patterns into the substrate layer. Finally, a timed hydrofluoric acid (HF) etch chemically removes the buried oxide layer and releases the device layer from the substrate in pre-specified areas, using etch holes.

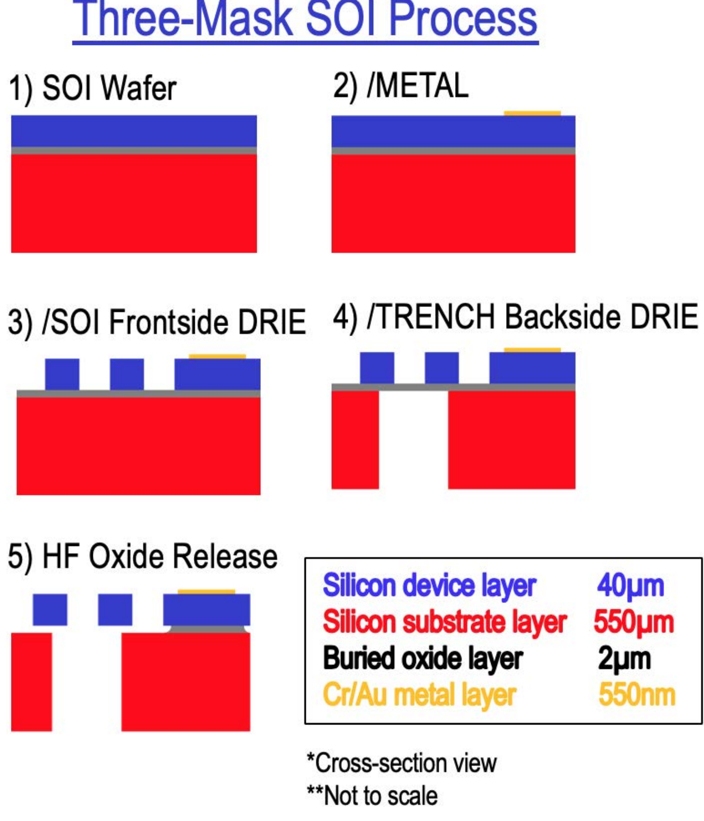

Figure 1.4: Cross-sections of the main steps in the three-mask silicon-on-insulator fabrication process used in this work.

1.4.2 Process Limitations and Assembly Challenges

Although there are many advantages to the standard process described above, it also comes with its limitations. Due to the nature of the top-down anisotropic DRIE etch used, out-of-plane motion is more challenging to design, and there is no 3D construction. In order to build a walking microrobot, manual assembly is tedious yet usually necessary after fabricating each chip. For example, it took on average about two hours to hand-assemble one silicon hexapod [5]. The device layer is most commonly used for routing electrical signals. This one routing plane limits the electrical connections that can be achieved, and forces the use of wirebonding or silver epoxy in order to accomplish any necessary cross-routing.

Having to rely on wirebonding or silver epoxy for electrical connections can be extremely tedious and ineffective. For example, to run the silicon hexapod legs [5] without any additional on-board power or control chips, nine individual signals had to be connected to wire tethers. In addition, the motor signals for each leg had to be wirebonded out in multiple areas due to the inability to cross-route any signals. Finally, all the motor signals were individually silver epoxied using through wafer 100µm pillars. Using silver epoxy is not only tedious, but can be messy and potentially detrimental to the small silicon structures. Although not well documented or studied, there are various anecdotal accounts of the epoxy out-gassing during the curing process and damaging MEMS devices. Due to a combination of the issues mentioned above, the resulting silicon hexapod was able to walk, but it was still heavily held back by tethers, and not every motor worked at the same time.

In order to assemble microrobots as easily as Legos, it will be important to develop an assembly method with low number of parts and assembly steps. This assembly method must be able to robustly connect the mechanical and structural pieces of the robot, while also reliably connecting every electrical signal needed to power and control the system. To work towards autonomy, it is not only necessary to integrate with MEMS chips, but it is also essential to easily integrate the robot MEMS parts with CMOS and solar cell devices. One option is to achieve this integration goal in the fabrication process itself, such as Bellew et al. [21]. However, this would increase the fabrication process steps, and is not currently a commercially available standard process. Using the three-mask SOI standard process, a modular and reversible approach to assembly could open the doors to create larger, mechanically and electrically interconnected structures from swarms of individual microrobots.

Chapter 2

Zero Insertion Force MEMS Socket

2.1 System Overview

Figure 2.1: A first iteration of the ZIF socket can be seen on top of a gold coated US penny.

As discussed, there is currently no quick, easy, and cleanroom-free process to integrate MEMS and CMOS chips in order to create the necessary 3D structures for microrobots discussed in Chapter 1. This chapter presents a zero insertion force (ZIF) MEMS socket, occasionally nicknamed Ziffy. A first iteration of a single ZIF socket chiplet can be seen in Fig. 2.1. To achieve 3D mechanical assembly, the socket uses previous work on energy storage in springs to clamp on to chips [22]. Electrical probes in the socket are designed to connect to the pads of the inserted chip, providing parallel electrical connection between the socket and any MEMS or CMOS chip of choice. A 3D model of the socket and inserted chip assembly be seen in Fig. 2.2.

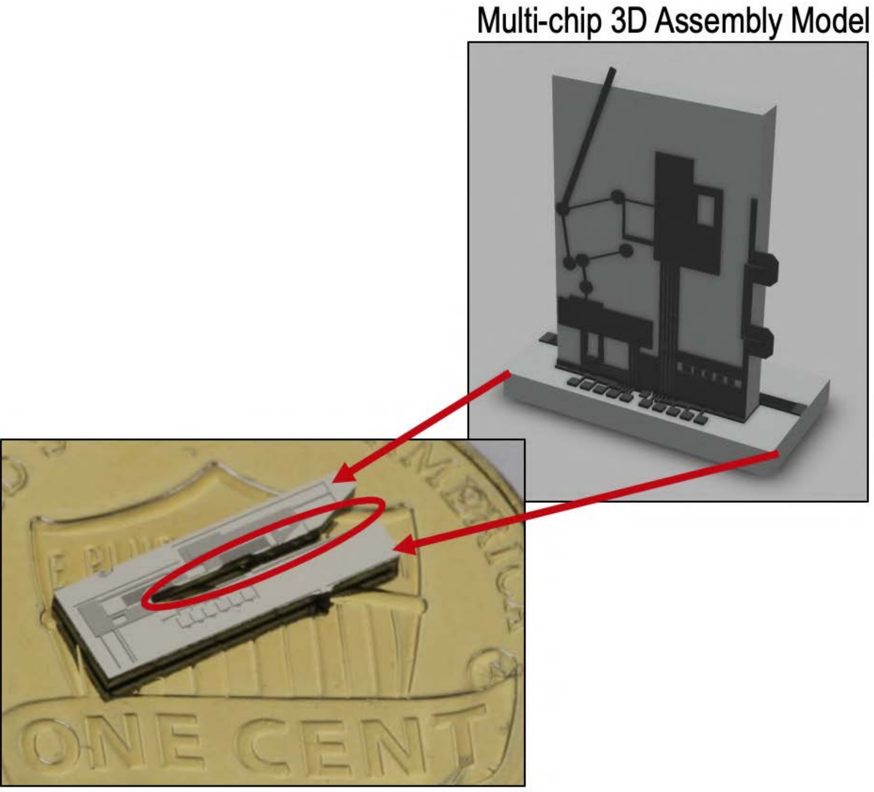

Figure 2.2: A 3D model of the socket and inserted chip assembly. The red arrows are used to indicate the correlation between the socket in the model and the socket from Fig. 2.1. The inserted chip in this model is a MEMS silicon microrobot leg based on the silicon hexapod legs [5].

Inspired by the classic childhood toy Legos, Ziffy aims to redirect microassembly solutions towards an effortless and fluid process where any researcher can build a microrobot without the need of a cleanroom. The ability to "snap" together MEMS devices with other MEMS and CMOS chips can reduce laboratory expenses and the overall tediousness of alternative microassembly approaches used today. Where wire-bonding requires 32 steps to make 32 electrical connections, Ziffy is designed to make all 32 connections in less than 10 assembly steps. Also, unlike conventional methods such as wire-bonding, Ziffy is capable of providing the system with stable mechanical connections in addition to electrical integration. This work is proof of concept that silicon microrobots can be pieced together using several chiplets, creating autonomous and moving 3D structures.

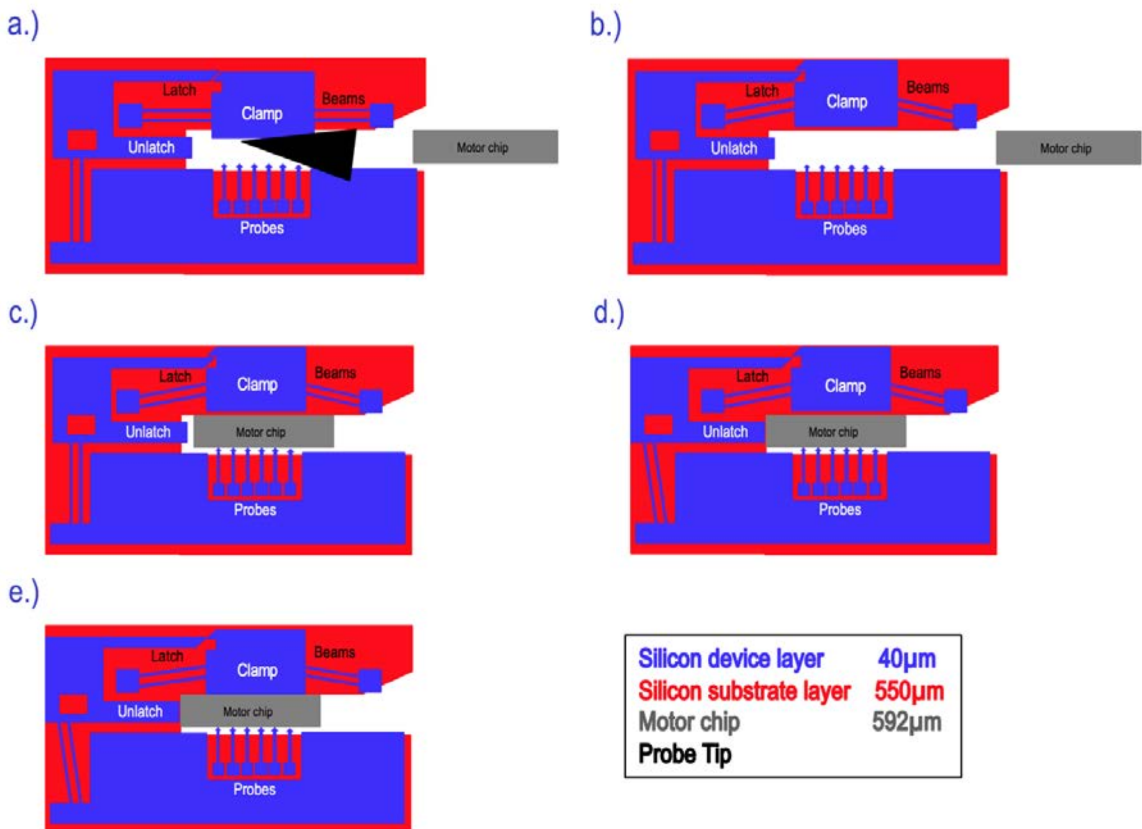

Figure 2.3: a.) Motor chip and ZIF MEMS socket in their initial, neutral state. b.) Clamp is pulled back and latched. c.) Motor chip is slowly inserted into socket. d.) Chip is inserted all the way into the socket, reaching horizontal alignment between the socket probes and the chip pads. e.) The unlatch structure is engaged: the clamp closes on the chip, providing the system with electrical contact and mechanical integrity.

2.1.1 Assembly Process

The ZIF MEMS socket has several subsystems: a) a clamp and spring structure, b) a latch and release structure, and c) probe tips. Each subsystem and its corresponding design methodology is further discussed in detail in the subsections below. To understand the design considerations for each subsystem, the assembly process using a ZIF MEMS socket and a MEMS motor chip is first explained. Both chips are designed and fabricated using the process described in section 1.4.1. Based on the work by Penskiy et al. [23], the MEMS chip is a linear electrostatic inchworm motor designed with gap-closing actuators (GCAs). This design is a high force linear motor that optimizes the single-mask actuator by Yeh et al. [24] by reducing the total number of control signals and total area needed.

Fig. 2.3 shows a top-down model of the microassembly process. The ZIF socket is face-up

parallel to the page, and the MEMS motor chip is at 90º to the ZIF socket, protruding out of the page. The ZIF socket assembly was designed to be manually conducted at a probe station, using tungsten probe tips on micromanipulators. First, the ZIF socket is securely placed on the chuck with glass slides that act as stops at the top and left sides of the socket. Then one of the tungsten probe tips is used to push the clamp up until it engages with the latch, Fig. 2.3a and b. This step pre-loads the clamped-clamped beams on either side of the clamp and creates space for the motor chip to be inserted. After loading the clamp and spring, the motor chip is carefully pushed to the left using either another tungsten probe tip or hand-held tweezers, Fig. 2.3c. When the contact pads on the motor chip are horizontally aligned with the probes on the ZIF socket, the motor chip will engage the unlatch mechanism, Fig. 2.3d. The clamp will snap against the substrate of the motor chip, clasping it into place.

Vertical alignment of the motor chip pads to the socket probes can be achieved by placing the center of the pads at the correct height in the motor layout. This height should be at least 572µm. This is equivalent to the sum of: the ZIF socket substrate thickness, 550µm, the oxide thickness, 2µm, and half the probe, or device layer thickness, 20µm. This height ensures a pad's center will align with the center of the 40µm thick socket probe contacting it.

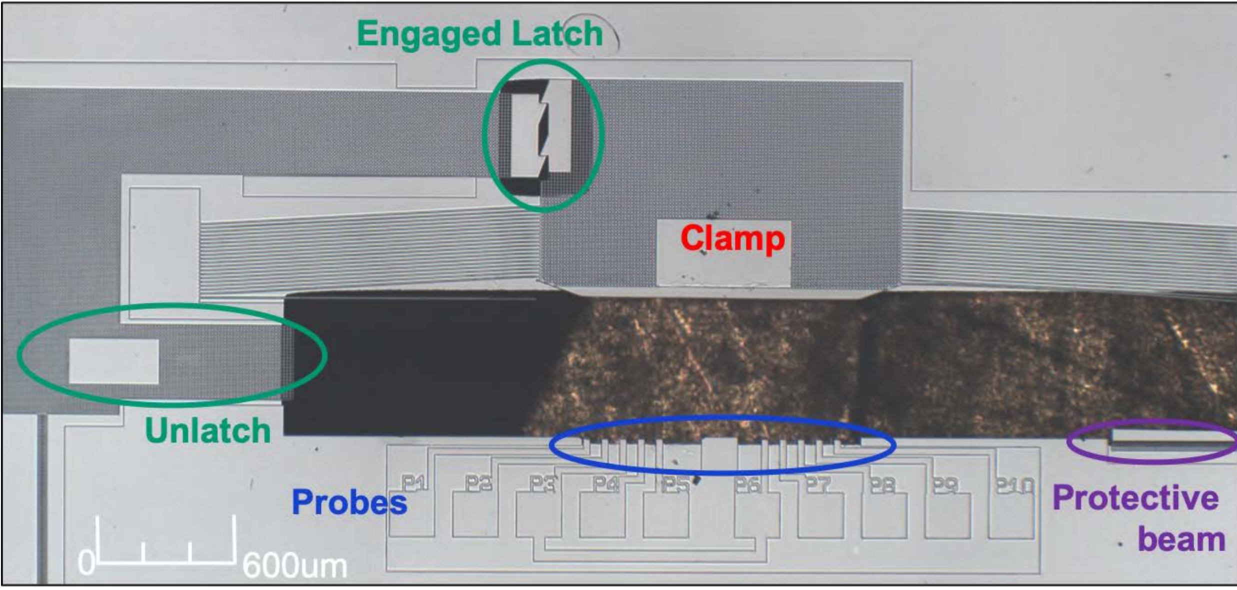

Figure 2.4: A top-down microscope image of the ZIF socket and its subsystems at the stage shown in Fig. 2.3b.

Once understanding the assembly process conceptually, it is easier to recognize each subsystem when observing images of the real fabricated devices. Fig. 2.4 is a top-down microscope image of the ZIF socket and its subsystems. This image shows the clamp pulled up and the latch engaged. In addition the the three main subsystems, it also shows a protective beam. This beam was added to push the motor chip away from the probes during assembly,

helping protect them from any potential collisions. The three subsystems and the protective beam were all designed in the SOI, or device layer.

2.1.2 Clamp and Spring Subsystem

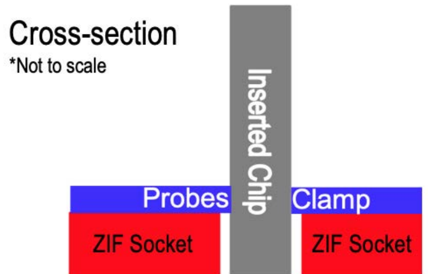

Figure 2.5: A cross-section of the final ZIF socket and motor chip assembly.

The clamp and loaded spring are the main mechanisms applying a force to hold the motor chip in place. A cross-section of the assembly described in Fig. 2.3 can be seen in Fig. 2.5. Additionally, a microscope image of the clamp and spring system can be seen in Fig. 2.6. In this image, the latch is engaged. The clamp is simply an SOI plate that the large tungsten probes can pull back using the large hole at the center of the plate. Looking very closely at Fig. 2.6, it is easy to see markings on the clamp right above the red "Clamp" letters. The tungsten probe scratched these markings on the clamp during the latching step. The latches then engage, storing energy in the spring. The spring is a series of fixed-fixed beams on either side of the clamp, anchored at the ends.

Figure 2.6: A top-down microscope image of the clamp and spring subsystem.

Each horizontal pair of beams attached to the clamp can be modelled as a fixed-fixed beam that is centrally loaded. This model takes into account the bending strain of the beams, and considers a small angle approximation [25]. However, due to the size and displacement of the beams that the ZIF socket uses, a non-linear term must also be included to account

for the axial stress on the beams [22, 26]. The force equation that includes both the bending and axial stresses can be seen below:

$$F(x) = \left(16\frac{Ew^3t}{L^3}x + \frac{8Ewt}{L^3}x^3\right)N \tag{2.1}$$

In Equation (2.1) above, F(x) is the total force with respect to the displacement x. E is the Young's Modulus of the material, 170GPa for silicon. The variables t, w, and L refer to the thickness, width and total length, respectively, of the beams. With the three-mask SOI process used to fabricate Ziffy, the thickness t of the beams is 40µm. The variable N refers to the total number of fixed-fixed beams in parallel.

In the commonly used design from Figs. 2.4 and 2.6, the beams are 3000µm long, 6µm wide, and N=20. At 100µm displacement, when the plate is pulled back and latched, the beams have a restoring force of about 240mN. This displacement was estimated to allow for enough spatial compliance when the motor chip is inserted, in order to avoid fracturing of the probe tips. When the motor chip is fully assembled, the displacement of the beams is about 50µm. This results in a restoring force of 30mN. This force is large enough to hold a 0.3x2.5x1.5mm^3 chip at 1000s of g's, where one g is the force of Earth's gravity.

2.1.3 Latch and Release Subsystem

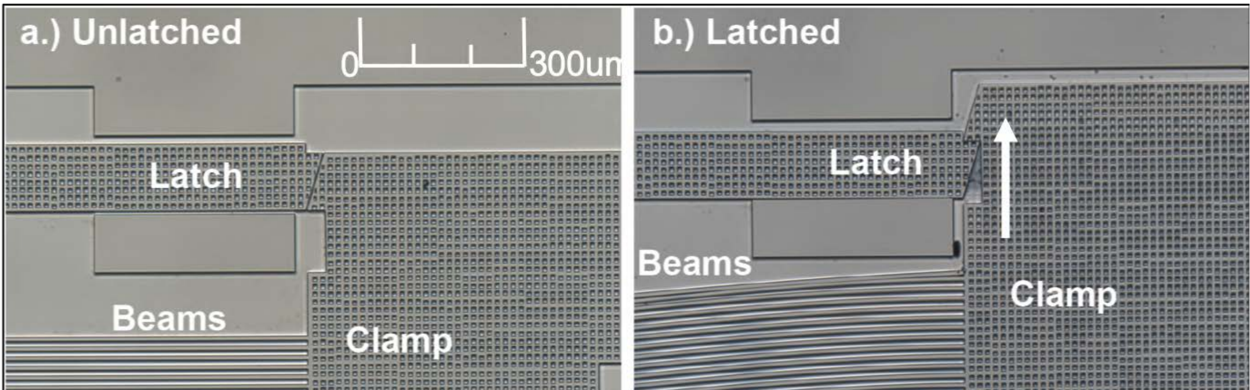

Figure 2.7: A top-down microscope image of the latch before and after engaging.

A before and after image of the latch can be seen in Fig. 2.7. Fig. 2.7 shows an older version of the latch, while Figs. 2.4 and 2.6 show the ZIF socket with an updated latch. Fig. 2.8 also shows a zoomed-in image of the updated engaged latch. The latch in Fig. 2.7 was modified to prevent fracture due to corner stresses created by the presence of the square etch holes used in this process. Instead of using etch holes, a trench hole was etched into the substrate. Additionally, a second latching triangle was added to distribute the clamp's spring load between the two. Both of these design decisions were made in order to increase the robustness of the latch.

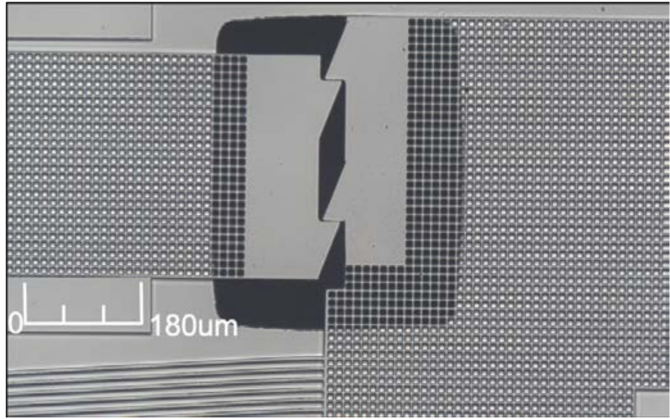

Figure 2.8: A zoomed-in microscope image of the engaged latch from Figs. 2.4 and 2.6.

The latch angle was designed and calculated to minimize sticking between the sidewalls. To achieve this, the tangent force, f_T, must be higher than the sidewall friction force, f_r, described in Equations 2.2 and 2.3 [27, 28]. The variable µ in this case is the coefficient of friction of the silicon sidewalls.

$$f_T > f_r \tag{2.2}$$

$$f cos(\theta) > \mu f sin(\theta) \tag{2.3}$$

Therefore,

$$cot(\theta) > \mu \tag{2.4}$$

Following Equation 2.4 above, the latch angle was calculated to be about 17º with a friction coefficient of µ = 0.3 [27]. Once the clamp is pulled back and latched, the motor chip can be inserted without constraints. When the chip is inserted all the way, it can push the unlatch structure, thereby releasing the clamp and activating the ZIF socket.

The requirement to push the unlatch mechanism in order to activate the socket can be seen as a feature rather than a limitation. The unlatch mechanism can be used to solve probe to pad alignment challenges. The socket was designed so that the pads and probes are in precise horizontal alignment after the motor chip has been inserted and when the unlatch mechanism is activated. A solution to vertical alignment for MEMS-MEMS assembly is discussed in section 2.3.1 and for CMOS-MEMS assembly in Chapter 3.

2.1.4 Probe Subsystem and Design

Fig. 2.9 shows the six probes (P1-P6) included in the ZIF socket to electrically connect to the motor chip. The left image shows the probe tips before assembly, and the right image shows the probe tips post assembly with the inserted chip. Two main factors allow one to

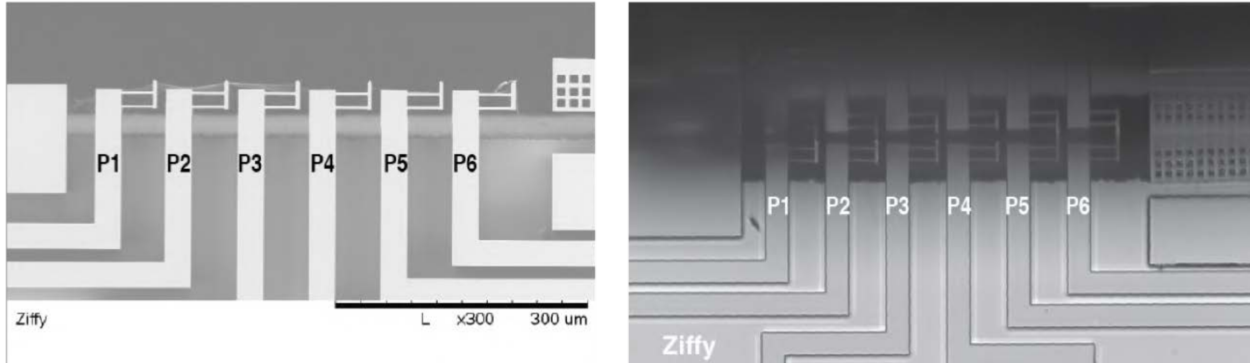

Figure 2.9: A top down microscope image of the six probes in the ZIF socket used to electrically connect to the motor chip. Left: the probes before assembly. Right: probes after assembly.

identify the difference between the two. First, the probes are reflected off the shiny silicon motor chip on the right image. Second, the beams on the left image probes are all straight while the beams on the right image probes are slightly bent, indicating the motor chip is pushing against them.

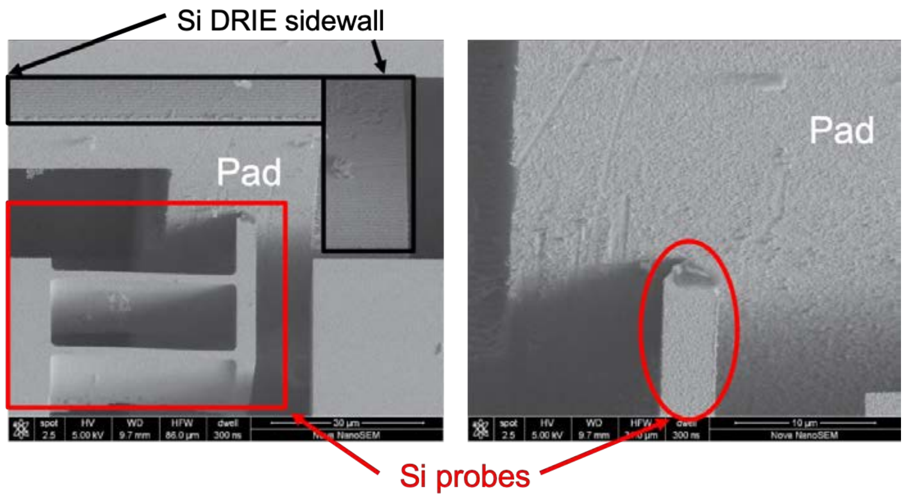

Figure 2.10: Two scanning electron microscope (SEM) images of a probe tip making contact with a pad. Left: zoomed-out. Right: zoomed-in to tip.

The probes were designed to have 1-2µm of compliance, and exert about 5mN of force on the motor chip. This force is expected to be large enough to breach any native oxide on the surface of the motor chip [29]. Two scanning electron microscope (SEM) images of a probe tip making contact with a pad can be seen in Fig. 2.10. To reduce the contact resistance between the probes and the pads, the probe tips can be coated with sputtered metal, or

routing lines can be defined using the evaporated gold from the three-mask SOI process in section 1.4.

2.2 Contact Resistance Characterization

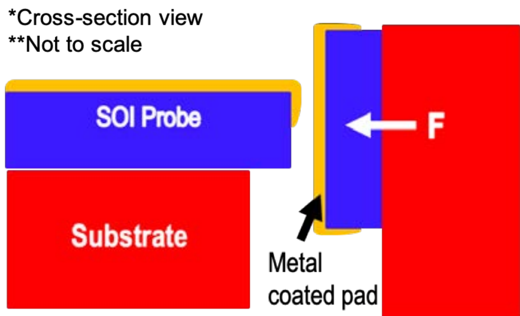

Figure 2.11: A drawn cross-section of a single ZIF socket probe against one pad on the inserted chip.

Low contact resistances are desirable for MEMS-CMOS and MEMS-MEMS assemblies to ensure the desired voltage and power values are provided according to the needs of each device. Exactly what is low enough depends on the specifications of each subsystem. The required resistances for a microrobotic platform using a CMOS chip (SCµM), solar cells (Zappy2) and MEMS motors are discussed in section 3.2.3 of the next chapter.

To understand contact resistance, we start by observing one ZIF socket probe against one pad on the inserted chip, Fig. 2.11. When the probes and pads are assembled, asperities (a-spots) on the surface of the connected ends will come into contact and eventually deform due to an applied force, F. When the contacts are covered by a residual, resistive film, three regimes of contact can be observed: 1) elastic, 2) plastic, and 3) compressive. Contact resistance is also defined as constriction resistance in the literature. Due to the higher forces (mN) used in this work, it is safe to assume the constriction resistance will not be in the elastic regime [30].

2.2.1 Holm's Contact Resistance Model

We can then model the contact resistance, Rc in the plastic regime using Holm's classic theory [31]:

$$R_c = \frac{\rho}{2r} \tag{2.5}$$

$$A = \frac{F}{H} \tag{2.6}$$

$$A = \frac{F}{H} = \pi r^2 \tag{2.7}$$

Equation 2.5 assumes a circular contact area with radius r, and material resistivity ρ for both the probe and the pad. In the plastic regime, the contact area can be approximated by Eqn. 2.6 to be equal to the applied load, F, of the contact divided by the material hardness, H [30, 31]. Assuming a circular contact area, the equation for the area of a circle can be equated with the previous approximation, Eqn. 2.7 [31, 32]. Finally, Eqns. 2.5 and 2.7 are used to derive the relationship between constriction resistance and a load contact force:

$$R_c = \frac{\rho}{2}\left(\frac{F}{H\pi}\right)^{-\frac{1}{2}} \tag{2.8}$$

It is important to note that Eqn. 2.8 can be used in the compressive regime if the exponential of the force, F, is equal to -1 instead of $-\frac{1}{2}$. Although not as common in the literature, this regime can be used to explain higher resistances since it implies the tested contacts were contaminated with resistive films [31].

2.2.2 Resistance vs Force Test Structures

To experimentally obtain resistance versus force measurements, we designed a test structure. Fig. 2.12 shows a 3D model of the two chips designed to assemble into the test structure. Two probes are side by side and attached to clamped-clamped beams, Fig. 2.12a. Fig. 2.13 shows a top-down microscope picture of the two probes. To measure a resistance between them, insert the chip, Figs. 2.12b and 2.14, with connected pads on two side pillars into the test structure and pushed against it, taking multiple steps. At the opposite end of the probes in Figs. 2.12a and 2.13 are Vernier scales used to keep track of the total displacement, x, as the chip is pushed.

Eqn. 2.9 is used to calculate the contact force, F at each step [22]. E is the Young's modulus of the material of the devices; E= 169GPa for springs fabricated parallel to the 110 plane of a (100) silicon wafer. The other constant is the thickness, t, which is defined by the device layer thickness of the process, t=40µm. The other parameters width (w), length (L), and number of beams (N) were set during the design to achieve the desired range of forces (F) and displacements (x) without fracturing. All device layer structures were designed with a maximum strain limit of 0.5% in mind.

$$F(x) = \left(16\frac{Ew^3t}{L^3}x + \frac{8Ewt}{L^3}x^3\right)N \tag{2.9}$$

To take resistance measurements, the inserted chip and test structure chip were 1) sputtered with Tungsten (W) and 2) evaporated with Gold (Au). The resistance was measured from probe 1 to probe 2 at each step. A similar test setup was used to obtain data for chips sputtered with Gold Palladium (AuPd). The AuPd sputtered chips had two probes designed

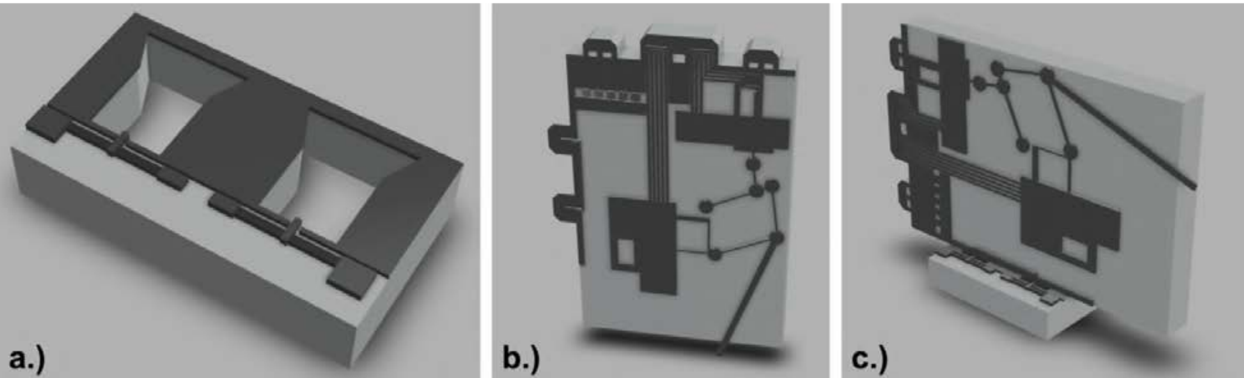

Figure 2.12: A 3D model of the resistance versus force test structures and assembly. a.) Two probes side by side on clamped-clamped beams. b.) A leg chip with pads on side tabs that can be inserted into the device from a). c.) The final assembly of the two chips used to take resistance vs force measurements.

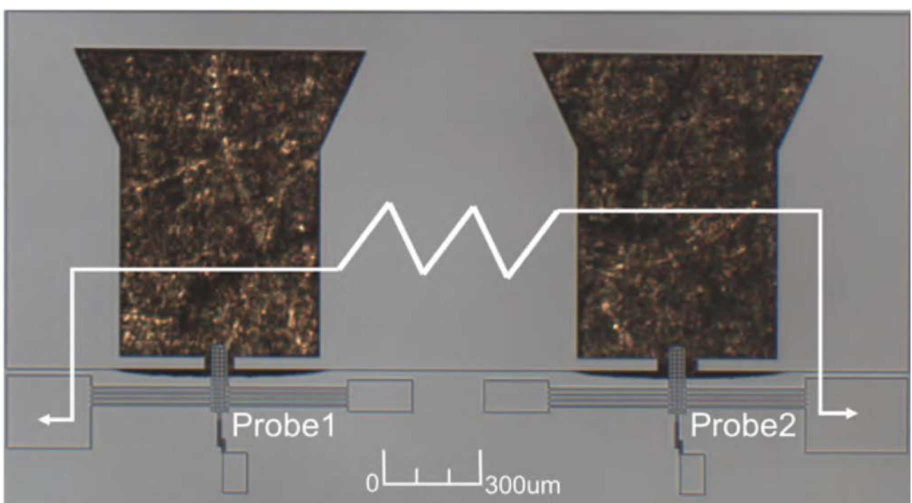

Figure 2.13: A top down microscope picture of the clamped-clamped test structure probes shown in Fig. 2.12a.

similar to the ZIF socket ones, with each probe tip connected to the ends of two clamped-guided beams in parallel. The equation describing the contact force, F, versus displacement, x, for these clamped-guided beams can be seen below:

$$F(x) = kx = N\frac{Ew^3t}{L^3}x \tag{2.10}$$

Fig. 2.15 shows a top-down drawing of the AuPd coated test setup. Figs. 2.16a and 2.16b show one single AuPd coated probe before and after engagement with the pads. Notice the reflection of the probe on the inserted, 90º vertical chip. To take the AuPd measurements,

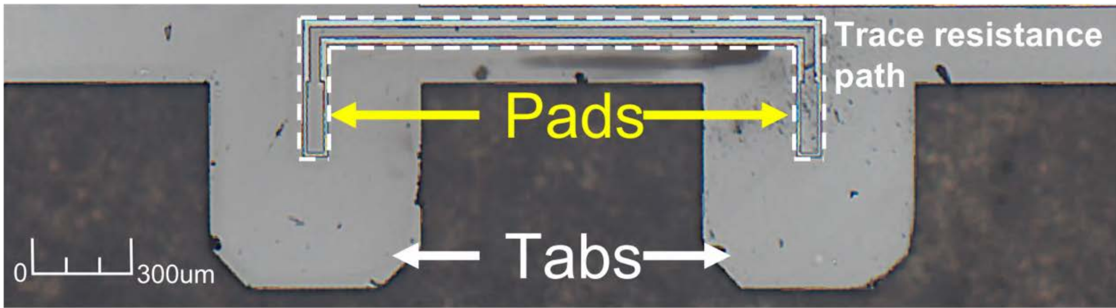

Figure 2.14: A top down microscope picture of the connected pads on the inserted chip. These pads are also on the side tabs of the leg chip in Fig. 2.12b.

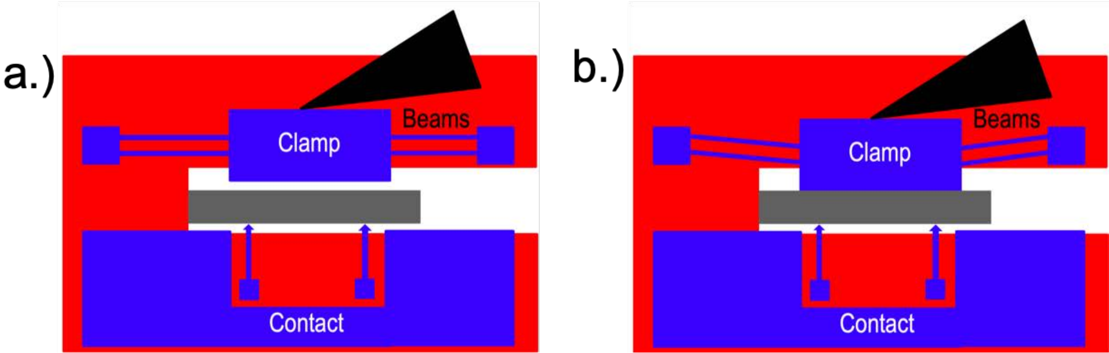

Figure 2.15: A top down representation of the Gold Palladium coated test chips with two probes attached to two beams in parallel. The gray block represents the inserted chip coming out of the page.

we used the actual ZIF socket probe design, which was less flexible than the test structures used for the W measurements. Therefore, the force regime for the AuPd structures was much smaller.

Since the total resistance measured will not only include the constriction resistance, but also the trace resistances, an initial resistance was added to the analytical model. This initial resistance is assumed to be equivalent to the trace resistances in the test structures. The initial resistance was calculated using the measured sheet resistance of the metal thin films and the test structure geometries. The sheet resistances were measured using a CDE ResMap four point probe. Furthermore, to account for the two contacts from both probe 1 and 2, the constriction resistance was multiplied by 2. The modified Holm's model is presented in Eqn. 2.11.

$$R_{total} = R_{trace} + 2R_c \tag{2.11}$$

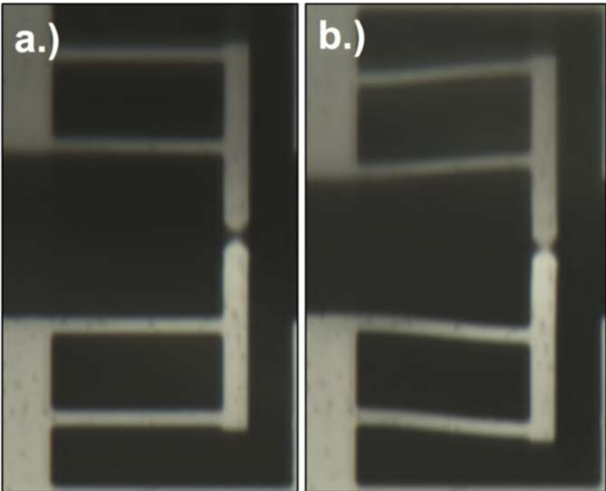

Figure 2.16: A top down microscope image of the AuPd sputtered probes before and after engagement. Notice the reflection due to the orthogonal chip.

2.2.3 Results

Figs. 2.17, 2.18, and 2.19 show the resistance vs force plots for the Tungsten (W), Gold (Au) and Gold Palladium (AuPd) test structures, respectively. All resistance measurements were conducted using a Keithley 2634B Source Meter. The W structures were sputtered with 40nm of metal, and had a measured sheet resistance of 3.13Ω/sqr. The Au structures were thermally evaporated with 100nm of the metal, and had a measured sheet resistance of 0.3Ω/sqr. A 5nm chrome film was used to adhere the Au to the Si chips. Its effect is taken into account in these calculations as part of the sheet resistance measurements. Finally, the AuPd structures were sputtered with 40nm of metal, and had a sheet resistance of 10Ω/sqr.

Due to the difficulty in measuring thin film hardness, the hardness, H, of the films was approximated based on the literature. 25GPa, 2GPa, and 1GPa were used for the W, Au, and AuPd films respectively [30, 32, 33, 34].

The measured resistance vs force lines are plotted against the modified Holm's model in Eqn. 2.11, for the plastic regime. The sputtered W had a calculated trace resistance of 315Ω, and fits the plastic regime as expected. Post experimentation, it was noticeable that the probe scratched against the W pad, Fig. 2.20a. Fig. 2.20b shows a scanning electron microscope (SEM) image of the triangular probe tip covered with W on top. The scallops caused by DRIE in the fabrication process can be seen on the Si sidewalls.

The evaporated Au had a calculated trace resistance of 30.3Ω. The total measured resistance was about 20Ω more than the model expected. A possible explanation is that Holm's model tends to underestimate the constriction resistance, as observed in the literature [32]. A lower range of forces could also be further studied for Au since it has a lower hardness value. A SEM image of the Au pad can be seen in Fig. 2.20c. The scratches were caused during insertion and testing of the chips.

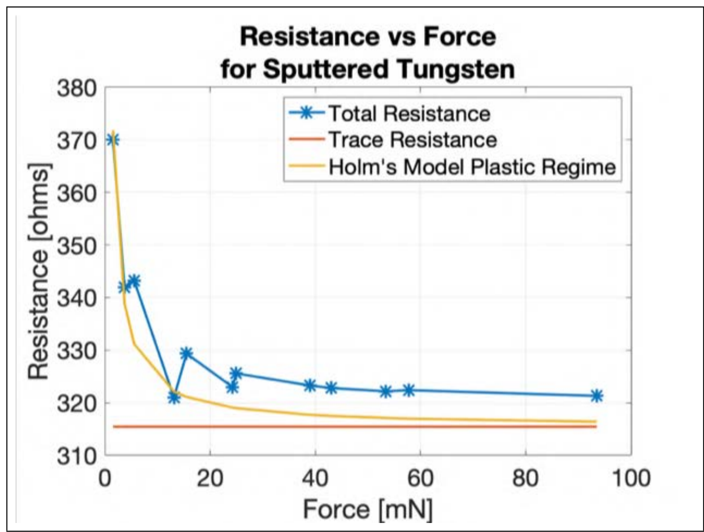

Figure 2.17: Plot of resistance vs force for Tungsten sputtered chips.

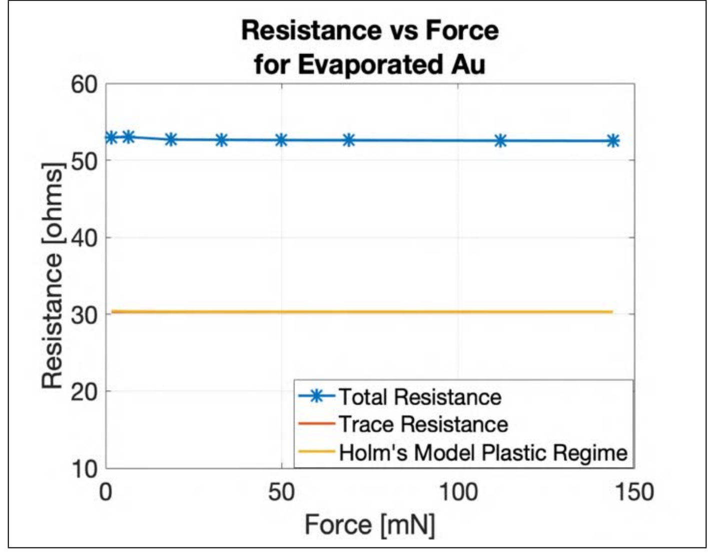

Figure 2.18: Plot of resistance vs force for Gold evaporated chips. The trace resistance is almost equivalent to the Holm's plastic regime resistance, and therefore not easily visible in this plot.

Finally, the sputtered AuPd had a calculated trace resistance of 320Ω, and is seen in Fig. 2.19. Previously, Gomez et al. [35] reported forces between 1-2mN were tested with the AuPd structures, and that it is possible that a higher range of forces needs to be tested to better fit the model. While the latter remains true, a small miscalculation in the spring constant equation was providing a smaller range of forces than what was actually tested. Fig. 2.19 shows a corrected plot from that published in [35], with the right range of forces.

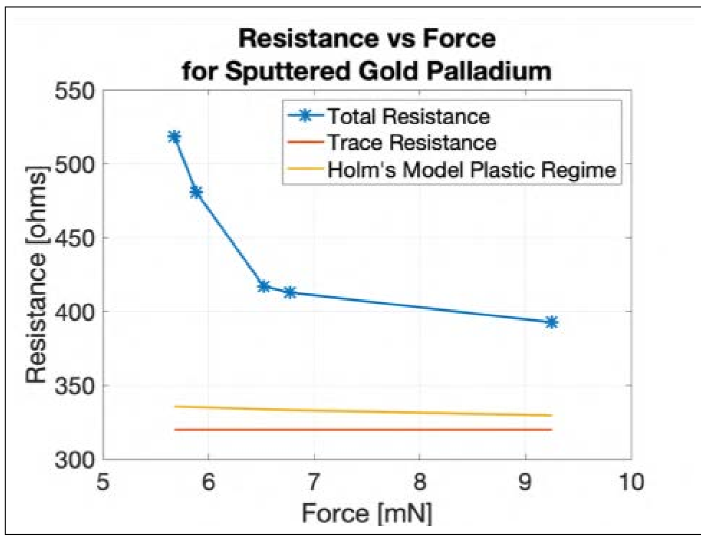

Figure 2.19: Plot of resistance vs force for AuPd sputtered chips.

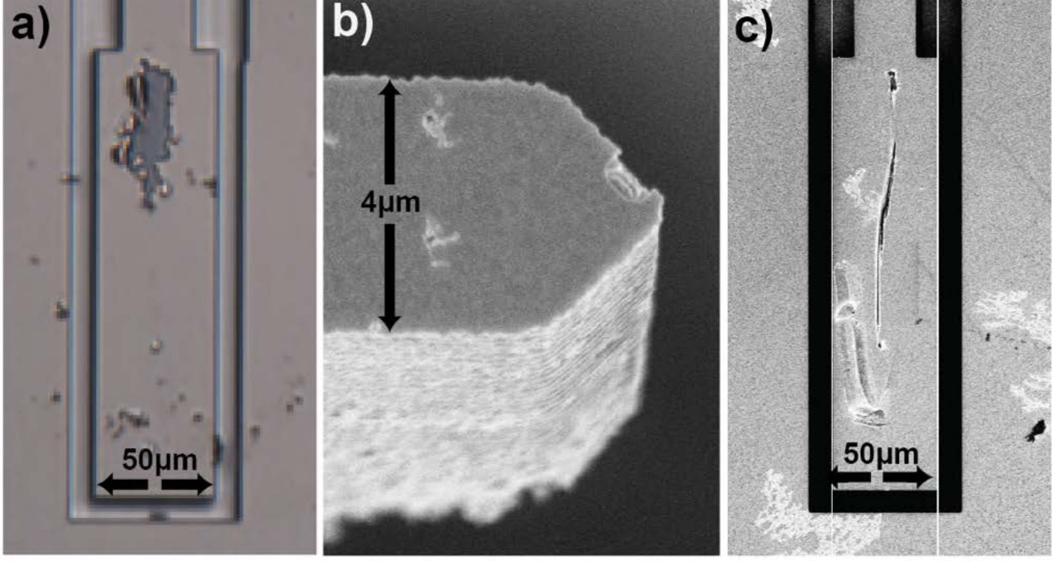

Figure 2.20: a) Microscope image of the Tungsten sputtered pad. The ZIF socket probe scratched against the pad. b) Scanning electron microscope (SEM) image of the Tungsten covered triangular probe tip. c) SEM image of the Gold evaporated pad.

2.3 MEMS-MEMS Assembly and Results

Various assembled systems were designed and tested to investigate the functionality of the socket: a ZIF socket with a motor chip, a ZIF socket with a leg chip, a double ZIF socket with two legs, and a hat chip with four ZIF sockets able to assemble with four legs. The

assembly steps described in Fig. 2.3 were used to assemble the systems. All inserted chips were tested and confirmed to be properly working prior to the assembly into the sockets.

2.3.1 Electrostatic Inchworm Motors

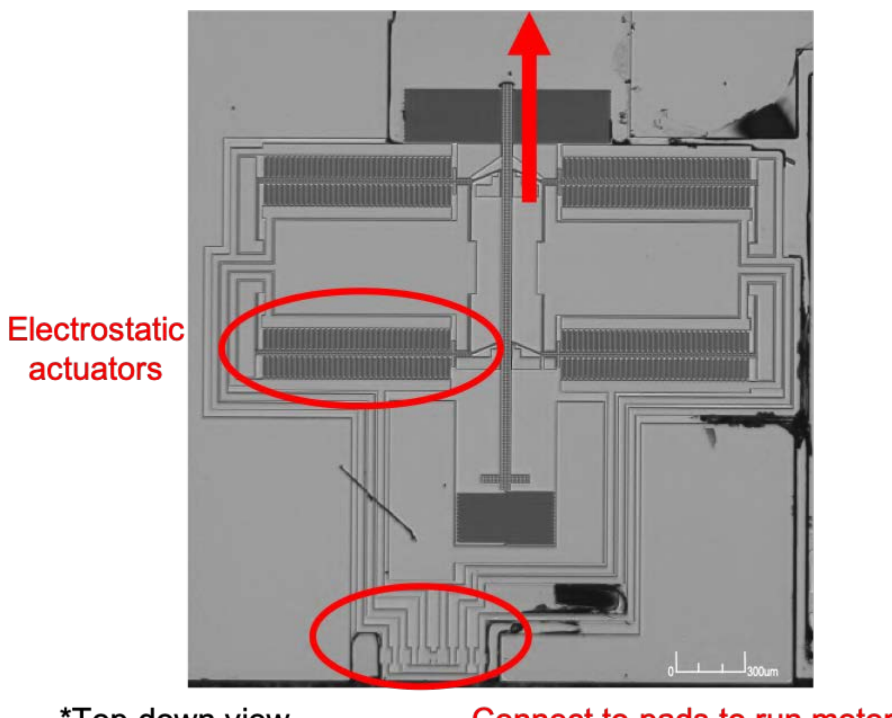

Figure 2.21: Microscope top-down picture of the linear electrostatic inchworm motor used for the first test assembly setup.

For the first test setup, a MEMS motor chip (Fig. 2.21) based on the design methodology used in [23], was assembled into a ZIF socket. The linear inchworm motor design and analysis is also explained in further detail in [8], where it was used to actuate silicon leg linkages for a one-legged and a six-legged robots. Each motor requires ground (GND) and two high voltage signals to run, one for the top set of actuators, and one for the bottom set. In [8], the left and right actuators for the motors are also disconnected from each other. This added an additional assembly: each motor required at least two wirebonds to connect all the actuators with each other. To resolve this, the motor routing was redesigned to connect the left and right sides, as seen in Fig. 2.21. The ZIF socket had six probes designed to contact the six pads on the motor chip, two for each signal or GND connection required.

An angled SEM image of the motor chip and ZIF socket assembly can be seen in Fig. 2.22. The ZIF socket probes are connected to larger pads labelled P1 to P6. Fig. 2.23 shows

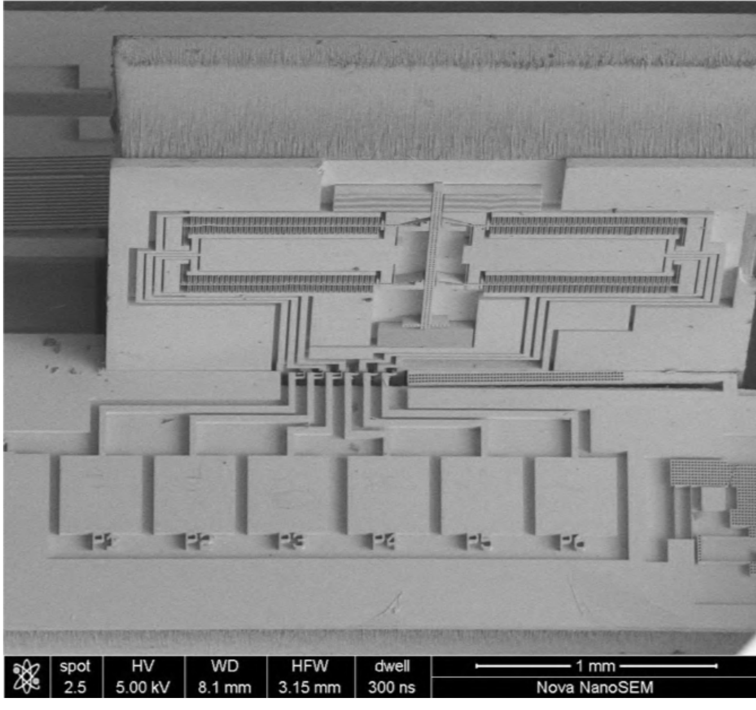

Figure 2.22: SEM of the motor chip and ZIF socket assembly.

the SEM of the motor chip and ZIF socket assembly from Fig. 2.22 next to the microscope image of the motor in Fig. 2.21. The top of the motor chip is labelled in both images. In the SEM image, the scalloping from the DRIE etch process is visible on the top of the motor chip. The red ellipses highlight the top and bottom gap closing actuators. The purple ellipses show the pads on the motor microscope picture, and the probes connected to the pads on the SEM image.

Post assembly, a 45º mirror was used to see the motor on the vertical chip moving through a microscope. A cross section of this setup can be seen in Fig. 2.24. After first confirming the six probes on the ZIF socket were engaged against the six pads, Fig. 2.25 on the motor test chip, the linear motor was actuated. Sample code used to run the motors can be found in **[TODO] add code to my Appendix? DC wrote it, but it's not in his or Craig's dissertations.** Using the 45º mirror, the vertically standing, moving motor shuttle could be seen through the microscope, Fig. 2.26.

The probe to pad horizontal alignment precision achieved was ± 20 µm, and an SEM image of the misalignment can be seen in Fig. 2.27. This misalignment is also about equal to the displacement required to engage the unlatch mechanism. In other words, it is possible the chips disengaged the latch during assembly. Then, the unlatch mechanism could have pushed back against the motor chip and created the misalignment during handling when preparing the 3D assembly for SEMs. The vertical alignment precision achieved was ±2µm, based on the minimum feature size of the device layer that is used to define the bottom edge

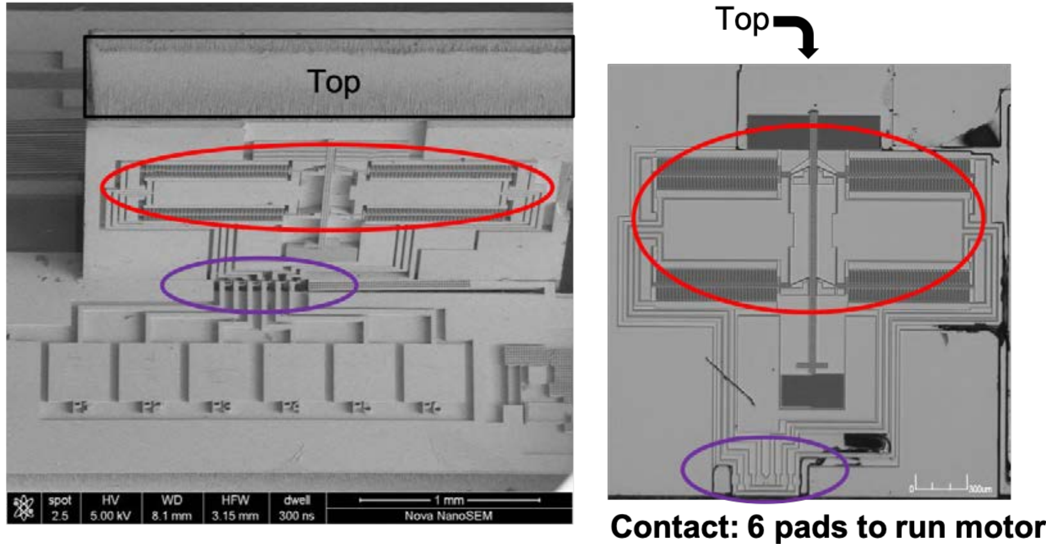

Figure 2.23: Cross-section of the top-down microscope setup used to see the motor chip and ZIF socket assembly from Fig. 2.22.

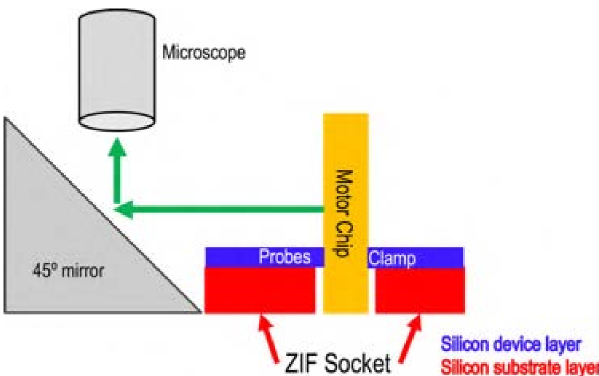

Figure 2.24: SEM of the motor chip and ZIF socket assembly from Fig. 2.22 next to the microscope image of the motor in Fig. 2.21.

of the motor chip. Vertical alignment in this assembly was also less challenging, since the motor chip pads could be designed to be located at the right height.

2.3.2 Silicon Legs and Steps Towards a Walking Microrobot

For the second test setup, a ZIF socket was assembled with a robotic leg with linkage design similar to that presented in [36] and developed in [8], Fig. 2.28a. Fig. 2.28b shows a 3D CAD model of the assembled system, used to verify the dimensions of the ZIF socket and inserted chip before fabrication and assembly. A similar setup to that in Fig. 2.24 was

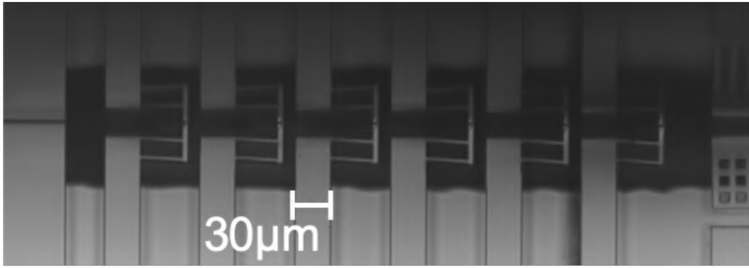

Figure 2.25: A top-down microscope image of the six ZIF socket probes engaged and reflecting off the vertical chip.

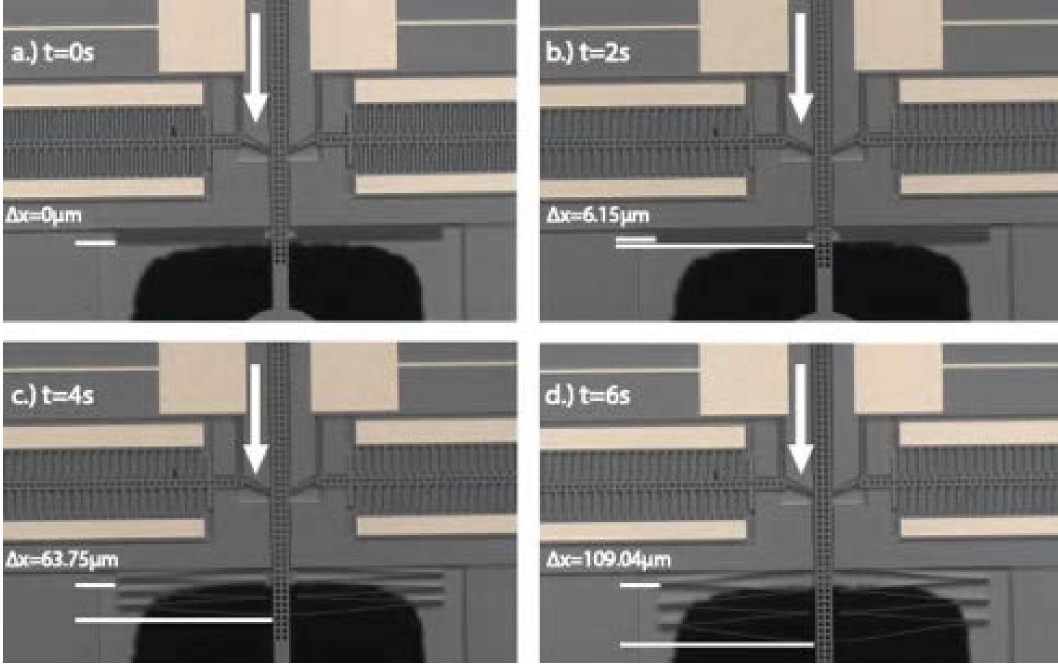

Figure 2.26: Snapshots of a video of the motor shuttle actuated through the ZIF socket. The video was taken using the setup in Fig. 2.24. The measured times and total shuttle displacements are noted. Displacement of the shuttle and the support springs is visible.

used to confirm the connection between the leg chip and the socket. The leg chip contains two motors: one for vertical actuation to push down and engage with the ground, and one for horizontal actuation to sweep back and take a step forward. This required a total of 5 electrical connections, 1 GND and 4 motor signals. Over etching in the process carved away at the fine teeth features of the motor shuttles more than the designed allowed for. The motors did not engage with the shuttle or push it forward. However, all electrical connection were confirmed to be successful: each individual gap-closing actuator was still activated.

Next, with a quadruped microrobot as the ultimate goal of this research, a double ZIF socket chip, Fig. 2.29 was designed to assemble with two legs at once. The resulting assembly

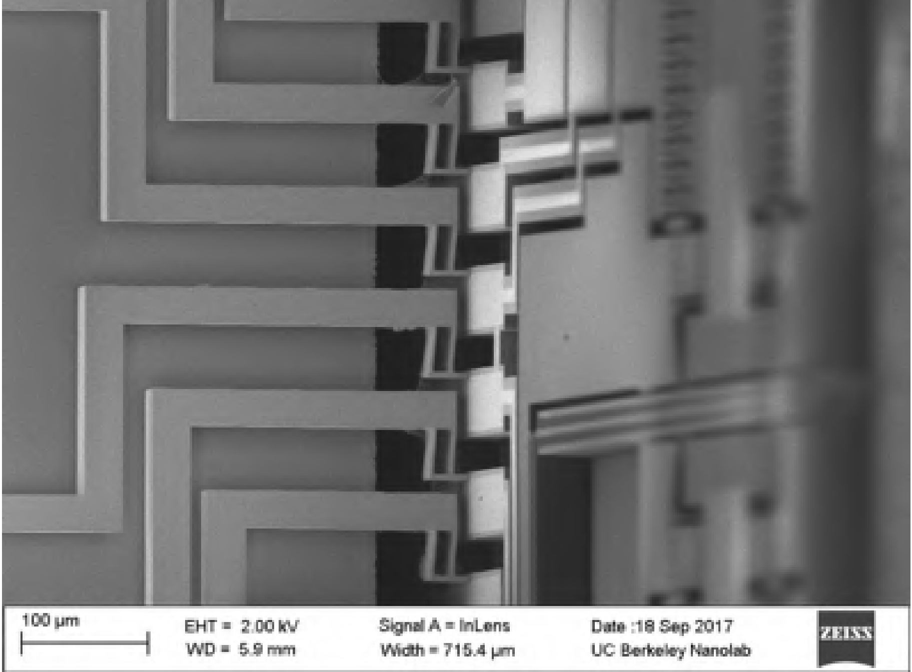

Figure 2.27: SEM image of the ZIF socket probes against the inserted chip pads, with a horizontal misalignment of 20µm.

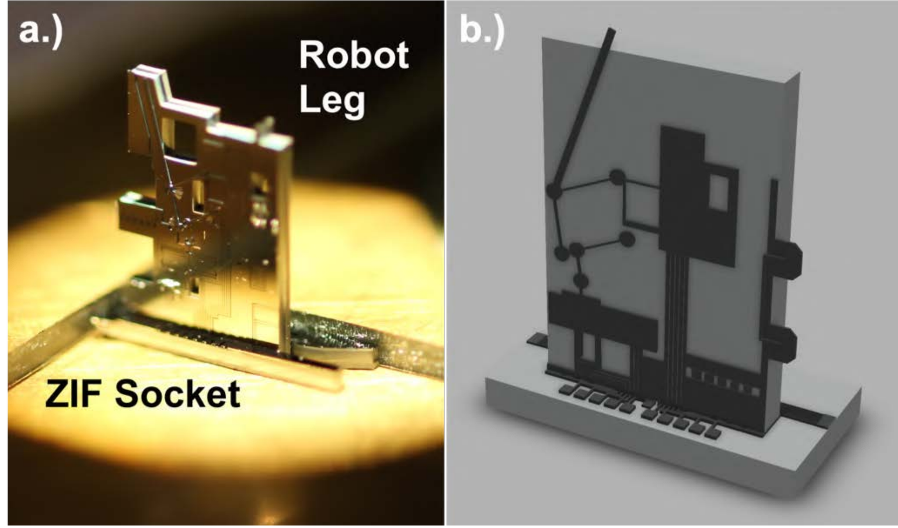

Figure 2.28: a.) A microrobot leg similar to the one presented in [36] assembled inside a ZIF socket. The leg is pointing up in this case. b.) A 3D model of the ZIF socket design and robot leg chip assembly seen in part a.).

can be seen in Fig. 2.30. Unfortunately in this case, the silicon leg linkages were damaged during handling and assembling. However, all the proper gap-closing actuators were again

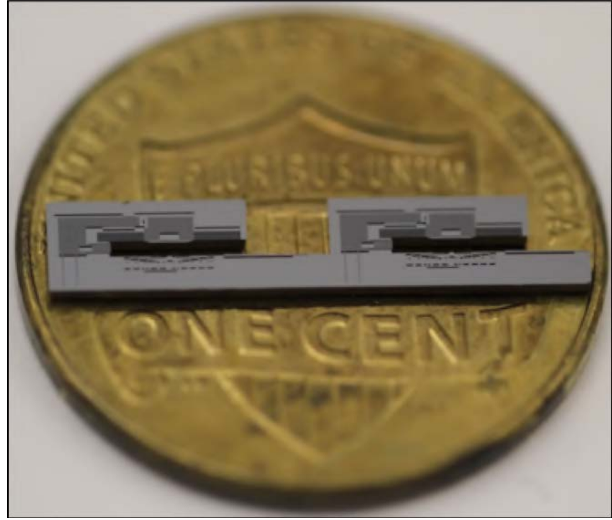

Figure 2.29: A picture of the double ZIF socket on a gold coated US penny.

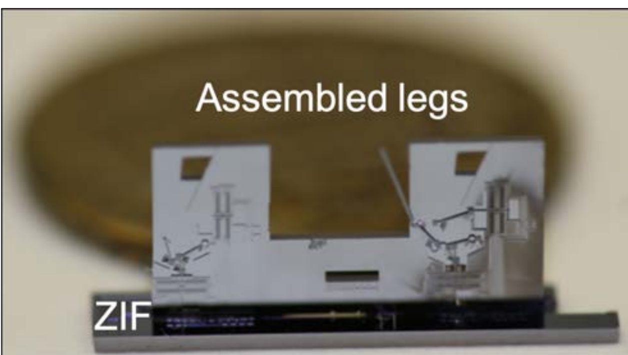

Figure 2.30: A double ZIF socket chip assembled with a chip containing two silicon legs.

actuated, therefore still making successful electrical connections through the ZIF socket.

Finally, a fully assembled silicon quadruped microrobot can be seen in Fig. 2.31 on the left. The robot was assembled using a hat chip with a double ZIF socket design for each side: one for the right legs, and one for the left legs. One double leg chip was designed to be able to fit into both the right and left sides of the hat chip. A Fusion 360 3D model of the robot can be seen on the right in Fig. 2.31. Due to a variety of non-ZIF socket related issues, the robot did not successfully walk. These challenges included: electrical shorts in the routing due to mistakes on the layout, an electrical short on one of the gap closing actuators also due to mistakes on the layout, and broken leg linkages due to manual handling of the chips.

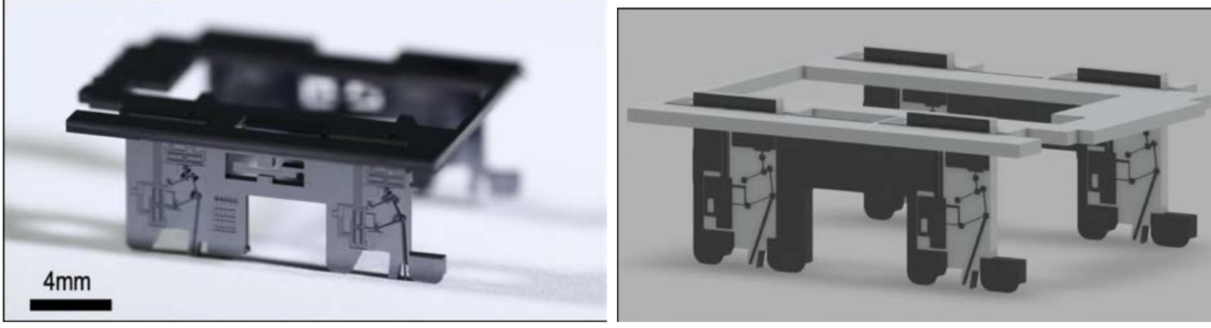

Figure 2.31: A fully assembled quadruped microrobot using two double ZIF socket assembly subsystems: one for the right legs, and one for the left legs.

Chapter 3

Modular Integration Platform for Autonomous Microrobots

3.1 MEMS-CMOS Assembly

Currently, the most popular methods used to integrate MEMS and CMOS devices require external tools and supplies. For example, wire bonding, flip-chip bonding, and silver epoxy are all commonly used approaches for electrical assembly. Wire bonding and flip-chip bonding both require a specialized machine in addition to the wire or metal material used for bonding. Although a machine is not necessary to use silver epoxy, only a hot plate for curing, at the micron scale accurate application of the epoxy without damaging any MEMS features can be extremely challenging. The three methods discussed also don't provide a mechanically sound solution to 3D assembly, which is necessary to build the microrobot structures discussed in section 1.2.1. This chapter presents the preliminary work conducted to custom design a ZIF MEMS socket for MEMS-CMOS assembly. The work is presented as part of an ultimately larger wireless system, and all the components for such a system are briefly discussed.

3.2 Components and Specifications for a Wireless System

When working with such small silicon devices, even some of the thinnest commercially available wires (60µm in diameter) can have a significant effect on a microrobot's actuation and mobility. Wire tethers have commonly been used in research to control and power MEMS silicon microrobots during actuation [5, 10, 9, 37]. To actuate just one of the motors described in section 2.3.1, at least three wire tethers are required: 2 square-wave actuation signals and 1 ground (GND) signal. To eliminate the need for wire tethers, this work proposes using ZIF sockets to integrate silicon MEMS devices with CMOS chips for control, and solar cell chips for power.

3.2.1 SCµM: Single Chip Micro Mote

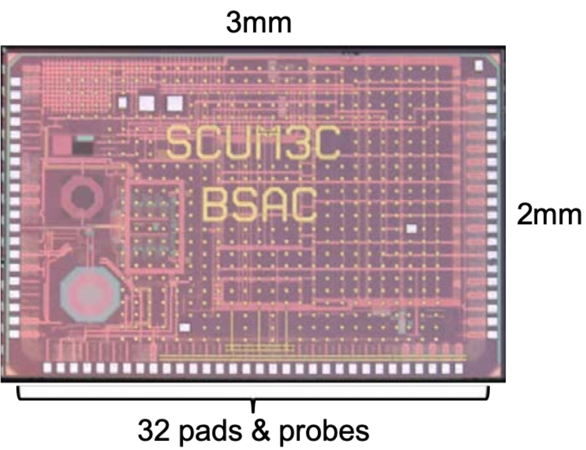

Figure 3.1: The single chip micro mote (SCµM) designed for microrobot control and communication [7, 38].

The single chip micro mote (SCµM), Fig. 3.1, [7, 38] is a CMOS chip designed for control, communication and any other necessary computing and processing for microrobots to function. SCµM is a system on chip (SoC) with an ARM Cortex-M0, a crystal free bluetooth low energy (BLE) beacon transmitter, and an 802.15.4 transceiver. These communication capabilities mean that someday, in theory, one could communicate with and control swarms of hundreds or thousands of microrobots using a cellphone.

There are 32 pads on the bottom of the SCµM chip to be able to assemble with 32 ZIF socket probes. The pads include connections to program the chip, which can also be remotely programmed through an optical bootloader. The other relevant available connections are: a) VBatt, which requires a minimum 1.2V for the SCµM battery power, b) VGPIO, which needs 3.3V to power the general purpose input/output (GPIO) pins, c) three different ground (GND) pads all connected to each other, and d) 16 general purpose input/output pins that can output signals of up to 3.3V peak-to-peak. The SCµM chip GPIOs can consume about 20mA of current [38]. SCµM is not able to provide enough voltage alone to run the MEMS motors from section 2.3.1, but any output control signal can be stepped up using high voltage buffers. Additionally, SCµM can receive feedback input signals of up to 3.6V to achieve closed loop control of MEMS motors or other microrobot parts.

To achieve accurate mechanical assembly with the ZIF sockets, the SCµM chip was also carefully characterized. The chip was measured to be 3mm by 2mm with a 310µm thickness. Fig. 3.2 shows a close-up diagram of the left most bottom pad of the SCµM chip. The 32 pads are each 53µm by 60µm on an 80µm pad pitch. The pads are 51µm ± 2µm above the bottom edge of the chip, and so on. These parameters helped inform the ZIF socket designs in section 3.5 to achieve an alignment accuracy of 2µm, which corresponds to the smallest feature size of the fabrication process used to develop the MEMS chips.

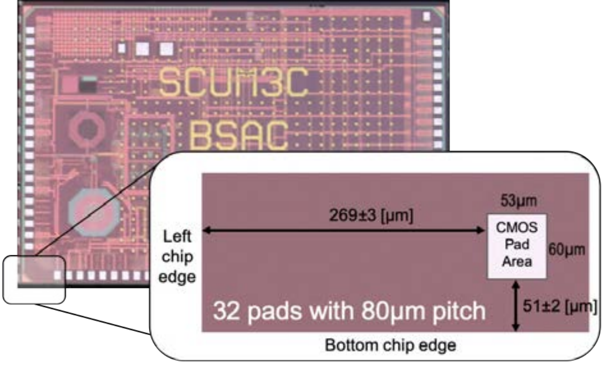

Figure 3.2: Pad alignment measurements for SCµM to assemble with the ZIF socket probes [7, 38].

3.2.2 Zappy2: A Solar-Cell Solution to Wireless Power

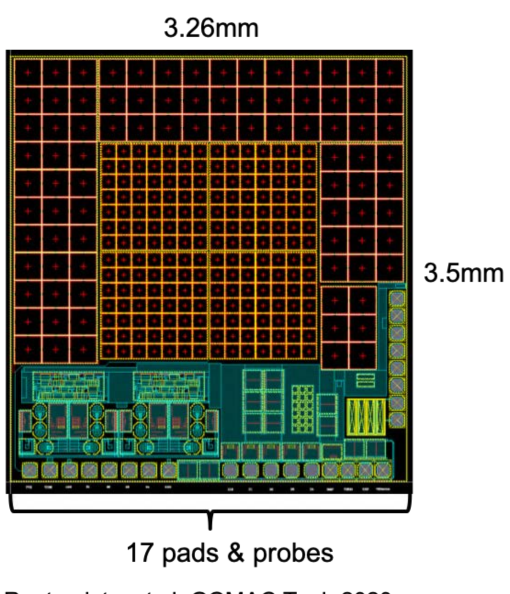

Figure 3.3: Zappy2: the solar-cell and high-voltage CMOS chip designed to power both SCµM and silicon MEMS actuators [6].

Zappy2, Fig. 3.3, is a 3.26mm by 3.55mm solar-cell and high-voltage CMOS chip able to provide all the necessary power to run SCµM and the intended silicon MEMS motors for microrobot actuation. It was fabricated using an X-Fab foundry SOI process [39]. It has 17 pads on the bottom edge of the chip, specifically placed there in order to connect all necessary signals to one ZIF socket with 17 probes. The 17 pads include: a) four digital control inputs for SCµM to control four high voltage buffers, b) four high voltage (120V)

outputs from the buffers to power a total of two silicon MEMS motors, c) three different GND pads connected to each other, d) one input clock signal that is nominally 100kHz and can be provided by SCµM, and e) three output voltage pads. The three voltage pads were designed for the following power outputs: 1) 3.3V, 20µA for the SCµM GPIO pins, 2) 1.8V, 270µA to power SCµM, and 3) a pad to probe the 120V, 3µA used for the output of the high voltage buffers.

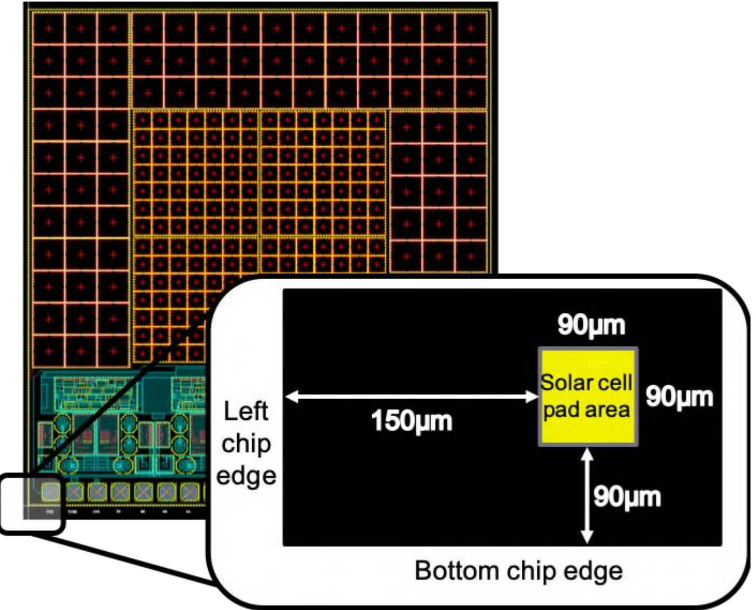

Figure 3.4: Pad alignment measurements for Zappy2 to assemble with the ZIF socket probes [6].

Similar to the SCµM chip, exact measurements for Zappy2 pad locations were recorded to help determine the design parameters of a custom ZIF socket. Fig. 3.4 shows a close-up model of the left most bottom Zappy2 pad. The pads are 90µm by 90µm on a 140µm pitch, 90µm from the bottom edge of the chip. To characterize both the SCµM and Zappy2 pads, an Olympus LEXT 3D confocal microscope was used. A 3D measurement of the chip provided the ability to know more accurately (±20µm) where the edges ended regardless of any small variations in the dicing process. Additionally, both the SCµM and Zappy2 pads recede slightly below the rest of the chip, which is covered by a protective glass layer. The confocal microscope made it possible to take 3D images of the pads and measure the receding. A scanning electron microscope (SEM) would have also been a viable 3D imaging tool for these measurements.

3.2.3 Parameter Considerations for ZIF Socket Design

When designing a custom ZIF socket for a chip, there are a few parameters that need to be taken into account in both the physical/mechanical space and the electrical space. In the physical realm, the chip thickness is used to determine the ZIF socket opening width to allow the chip to be inserted without opposing forces. The chip width is used to inform the necessary clamp width to increase the contact area between the two. The main subsystem of the ZIF socket that changes based on the inserted chip is the set of probes. The ZIF socket probes are designed to match the pitch of the inserted chip pads. Because of the assembly method of this ZIF socket, the distance from the left most edge of the chip to the left most pad is used to the determine the position of the left most socket probe in relation to the unlatch mechanism of the ZIF socket. In other words, the left most edge of the inserted chip will engage the ZIF socket's unlatch mechanism when the probes are aligned to the pads.

Finally, the recessed pad distance is used to design the probes. Both the SCµM and Zappy2 chips are coated in a protective and insulating layer, usually made of oxide. The deposition of this layer tends to be one of the last steps in the process. After the protective coat is applied, the oxide is etched away at the metal pads of the chips to allow for electrical connections. This creates a topography difference between the pads and the rest of the chip. The pads are recessed back from the rest of the chip by a value equal to the thickness of the protective layer, which was measured and taken into account. The intended goal of the design is to provide enough compliance for movement and robustness during assembly, but also sufficient strength to ensure the minimum needed force is applied to achieve a low contact resistance. Exactly how to define an acceptable "low" contact resistance is explained below.

As mentioned in section 2.2, the applied probe force is directly related to the resulting probe to pad contact resistance. If Zappy2 is able to provide SCµM with 1.8V for power, and SCµM requires a minimum battery voltage of 1.2V to operate, that implies a maximum allowable voltage drop, Vmax of 0.6V [7, 38]. SCµM has a maximum operating current, Imax of up to 3mA. The parameters Vmax and Imax can then be used to calculate the maximum total contact resistance a ZIF socket can have for the system to turn on, Rmax= 200 Ohms. Even the largest estimated resistance in the initial ZIF socket contact resistance vs force test setups from section 2.2 was under 100 Ohms at about 5-10mN of applied force, indicating a valid path in the design decisions towards MEMS-CMOS integration.

3.3 First ZIF Socket Designs and Assembly Challenges

The first attempt to assemble a CMOS chip with a silicon ZIF socket can be seen in Fig. 3.5. Unlike the ZIF sockets from Chapter 2, this first iteration did not involve a side funnel for the inserted chip to slide in. Rather, the CMOS chip was lowered down into the socket manually, holding onto the chip with a vacuum wand. This CMOS chip had 19 pads to connect to 19 probes on the ZIF socket. Although the ZIF socket held the chip in place, this assembly approach was unsuccessful due to misalignment between the pads and probes, with a vertical

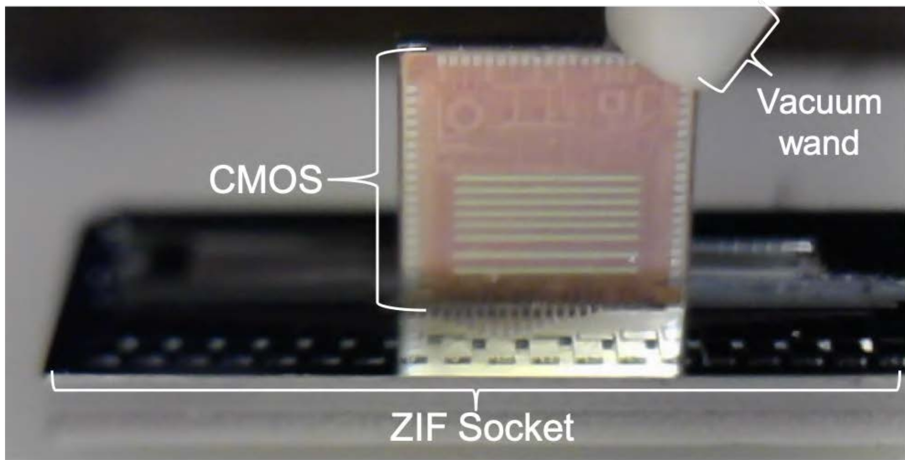

Figure 3.5: The first iteration of a ZIF socket assembled with a CMOS chip.

misalignment of about 100µm. If the z axis is the axis in/out of the page, the CMOS chip would also rotate about the z axis, so some pads made contact with the probes on one side but not on the other. This rotation during manual assembly raised the need for a stabilizing platform for the CMOS chip to rest on.

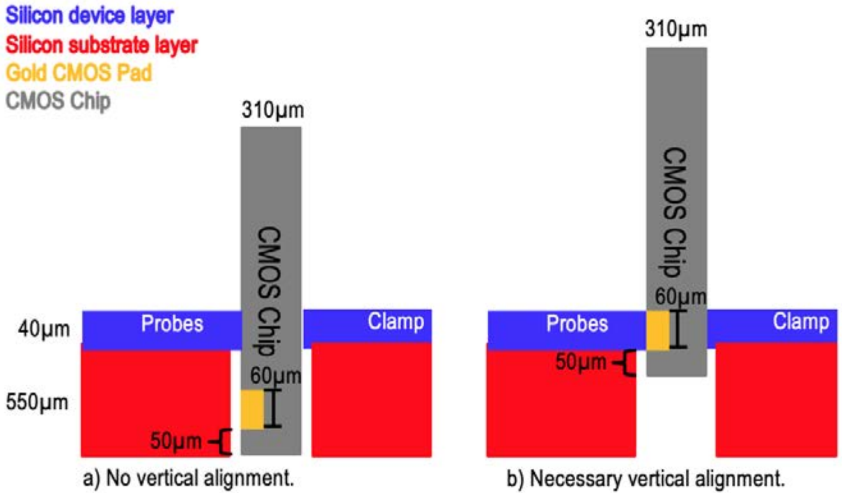

Figure 3.6: A cross-section model depicting the vertical misalignment between the SCµM chip pads and the MEMS ZIF socket probes.

Updating the original ZIF socket design from Fig. 3.5 to a design resembling the one in Chapter 2, precise horizontal alignment of <2µm can be achieved. However, this assembly method does not resolve the vertical alignment issue for the SCµM and Zappy2 chips. The SCµM and Zappy2 pads are located about 30µm and 90µm, respectively, above the bottom

edge of the chip. Using the same assembly method from Chapter 2 leaves a significant vertical misalignment, Fig. 3.6, that cannot be ignored. The CMOS chip needs to be raised some way in order to properly connect it to the socket probe tips. A solution to this vertical alignment issue is discussed in the next section of this chapter.

3.4 MEMS Cassette: a Solution to Vertical Alignment

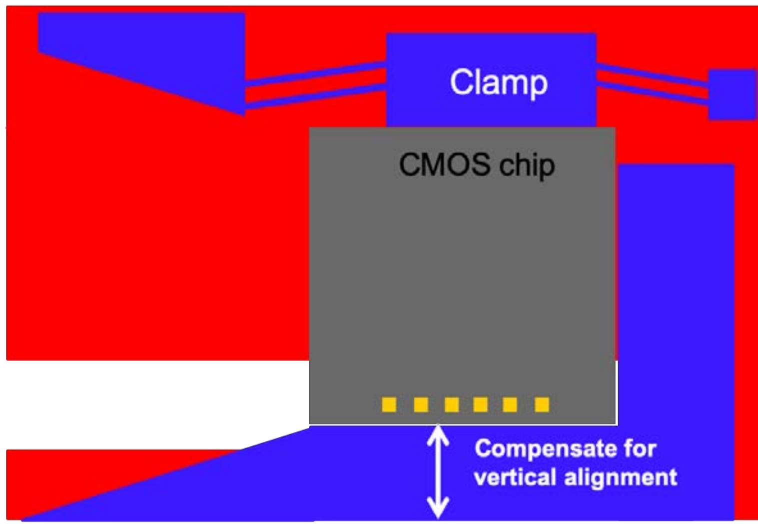

Figure 3.7: A top-down model of the proposed MEMS cassette.

To resolve the vertical alignment challenges mentioned in the previous subsection, a MEMS cassette holder for CMOS chips was developed. The MEMS cassette is intended to raise the CMOS chip to the correct height where vertical alignment can be accomplished. A clamp similar to the one on a ZIF socket holds a CMOS chip vertically in place, Fig. 3.7. The clamp pushes against the top side of the CMOS chip. The bottom side of the CMOS chip sits on the sidewall of a spacer included in the cassette's silicon device layer. This device layer spacer is anchored to the substrate, and designed to compensate for the pad height in order to help achieve vertical alignment between the pads and probes, Fig. 3.8b. The anchor also acts as a stabilizing platform, ensuring the chip cannot rotate about the z axis (in/out of the page) like in the first iteration of this assembly. The smallest feature size of the fabrication process used is 2µm, but the alignment and etch precision is down to ± 0.5µm for the device layer. Therefore, ± 0.5µm is also the theoretical minimum vertical alignment precision possible if using a cassette in this process. This is assuming that the SOI wafer substrate and device layer thickness is consistent throughout wafers, which is not always the case. Taking a possible 15µm of variation in thickness for the SOI wafer substrate from the manufacturer, the minimum vertical alignment precision would be ± 15.5µm.

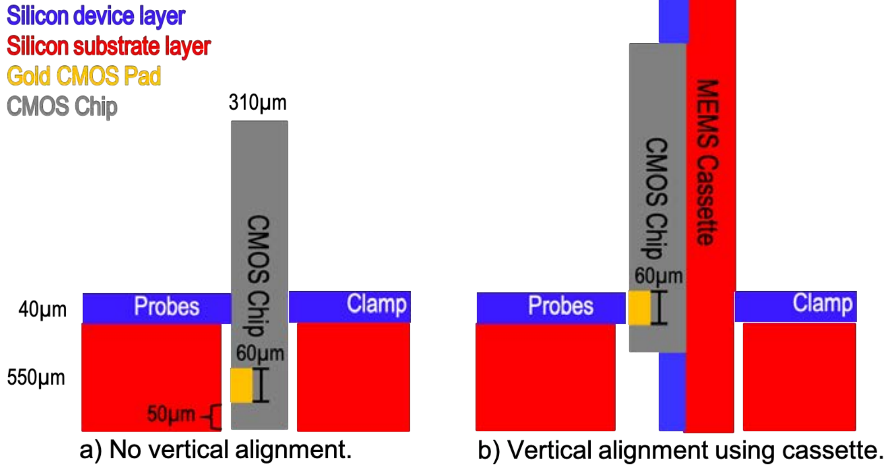

Figure 3.8: A cross-section model of the proposed MEMS cassette. SOI and substrate are not to scale for the MEMS cassette or ZIF socket.

With different pad locations, SCµM and Zappy2 require two different cassette designs, or one that is able to adjust for both height requirements. Fig. 3.9 on the left shows a model of a modular MEMS cassette designed to fit both chips. Fig. 3.9 on the right shows the MEMS cassette that was fabricated consistently using the same process described in section 1.4.1. In this setup, the SCµM chip fits inside a hole in the cassette's SOI, with its back parallel to the cassette substrate and the pads facing out of the page. The bottom side of the chip sits on top of the SOI vertical alignment spacer anchored to the substrate. This alignment spacer raises the chip to the desired height, y, where the pads will be vertically aligned to the ZIF socket probes.

The cassette was designed to clamp down on either SCµM or Zappy2 with an intended clamping force of 30mN due to the clamp's loaded springs. Since the chips are different sizes with different pad properties, the cassette was designed for the clamp to push against the top of the solar chip, and two spacers above and below SCµM were added so it could also fit, Fig. 3.9. The spacers are anchored to the substrate by weak springs, which can be easily broken off to use the cassette with the Zappy2 chip instead.

Unfortunately, the second spacer fell off during experimentation. In Fig.3.9 on the right, the SCµM chip is held in the cassette with a 200µm blob of silver epoxy on the back. The epoxy was kept far from any MEMS features during assembly and curing, and was kept contain within the needed area. To achieve simultaneous, one-step MEMS-MEMS and MEMS-CMOS assembly, the cassette also has a linear inchworm MEMS motor built into it [23].

The motor was designed to integrate with a motor ZIF socket to the right of the CMOS one. This motor has an end-stop detection resistive feedback sensor that can connect to SCµM through an integration platform, which has not yet been tested or demonstrayed. The feedback sensor is an anchor on the device layer of the cassette, covered with Au to reduce the contact resistance. The motor shuttle, which is connected to ground, makes contact

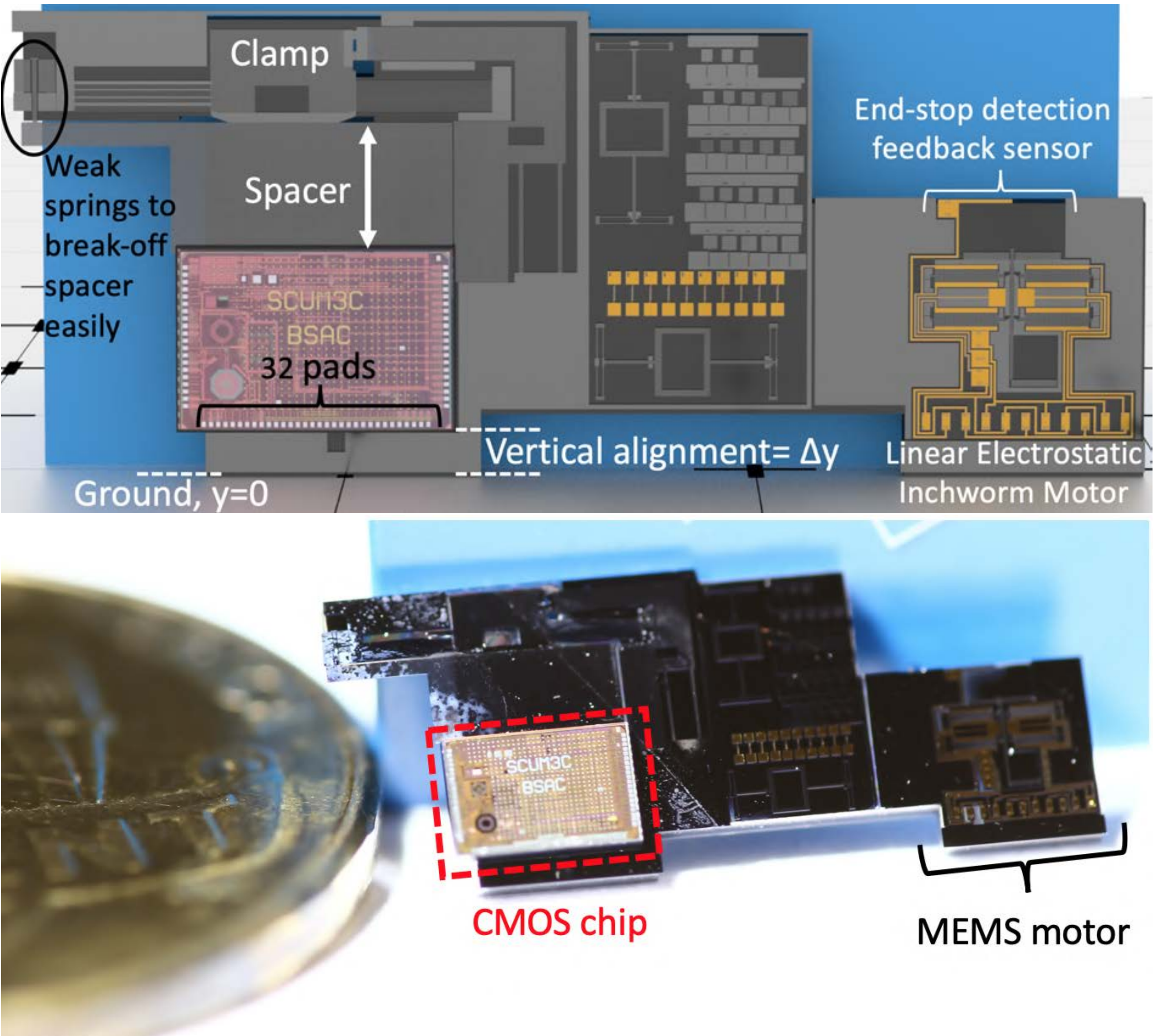

Figure 3.9: Top: A 3D model of the SCµM chip in the MEMS cassette. Bottom: A picture of the SCµM chip in the MEMS cassette, which was designed with a MEMS linear motor.

with the sensor at end-of-travel. Probe tips on the integration platform connect the other end of the sensor (a contact pad on the cassette) directly to a normally high GPIO pin on SCµM. The SCµM pin is designed to pull to ground at contact, and the chip should be able to use this feedback to control the motor. The integration platform is further described in the next section. The cassette allows for one-step, simultaneous double-ZIF socket assembly of a MEMS-MEMS subsystem and a MEMS-CMOS subsystem, similar to the double-ZIF socket assemblies designed to fit in with two microrobot legs at once in Chapter 2.

3.5 Modular Silicon Integration Platform for Autonomous Microrobots

3.5.1 System Description

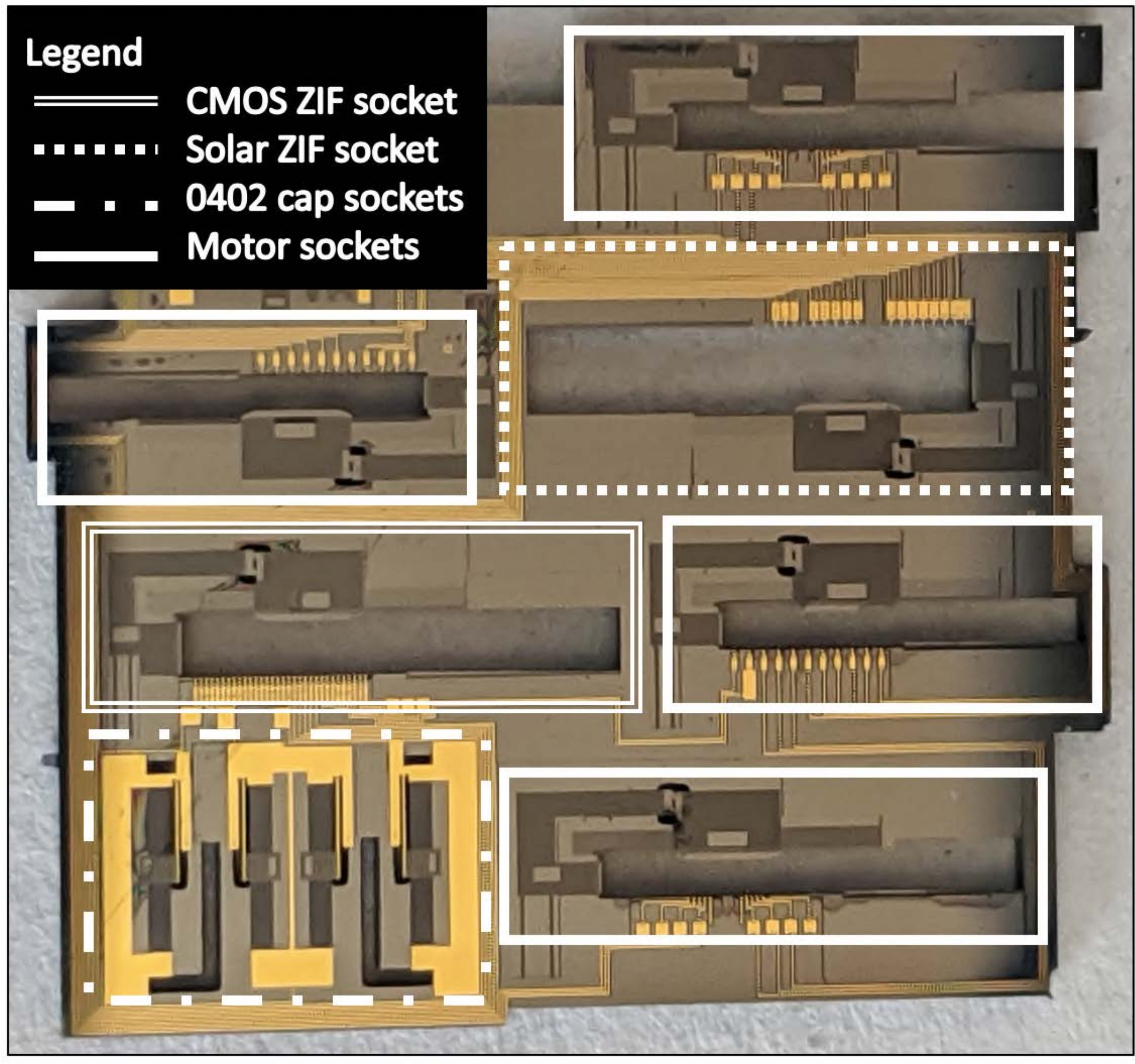

Figure 3.10: Full MEMS ZIF socket system designed for wireless microrobotic platforms. It can integrate with CMOS chips, solar chips, MEMS motors, and 0402 capacitors.

Fig. 3.10 shows a top down picture of a modular platform designed to bring together all the necessary components for a wireless microrobotic system. The CMOS and solar ZIF sockets were designed to fit around the SCµM and Zappy2 chips, respectively, and their

corresponding MEMS cassettes. The motor sockets next to the CMOS and solar ZIF sockets correspond to the motors included in the MEMS cassette from Fig. 3.9. These motors' shuttles are wired on the platform directly to a SCµM GPIO pin (normally high) to send end-stop detection feedback. Due to the motor design, the shuttle is normally grounded, and intended to pull the pin to ground when end of travel is reached. The two motors are wired, and therefore controlled, independently of each other. The other two motor sockets were designed to drive four motors, two of which are tied to one of the cassette motors, and two are tied to the other. The motors were wired in this way to demonstrate the simplest control signal configuration required for a microrobot to walk and move sideways: left motor/leg and right motor/leg.

3.5.2 Methodology and Results

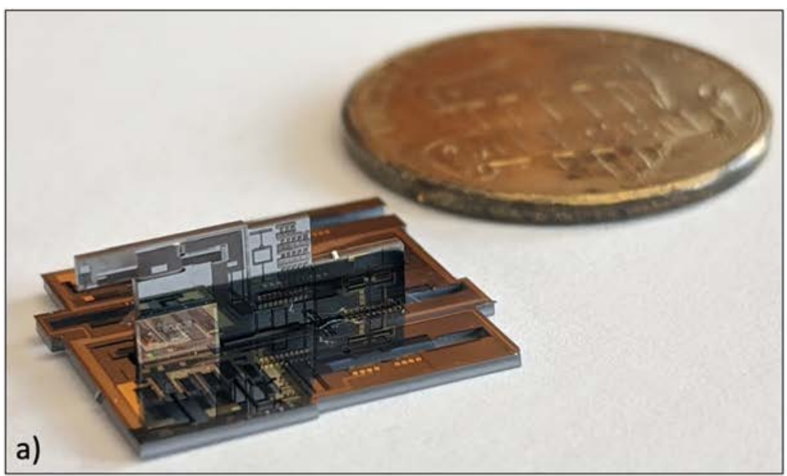

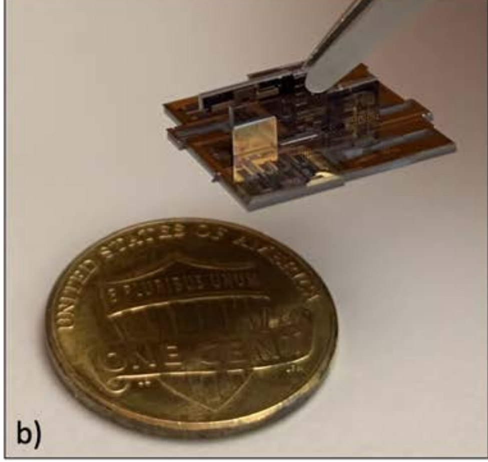

Figure 3.11: a) MEMS-CMOS assembly using a MEMS cassette to hold a CMOS chip, inserted into a ZIF socket. b) The system is being held up by a tweezer at one end of the cassette. The two clamps exert enough force on the cassette for the system to not disassemble.

After being assembled together, the cassette and SCµM subsystems were inserted and integrated into the ZIF socket, Fig. 3.11a. Fig. 3.12 shows a 3D model of the assembly in Fig. 3.11. The cassette and SCµM were first manually inserted from the top down into the sockets, pushed all the way to the right so no physical contact would be made with any socket probes. After insertion, the cassette and SCµM configuration was slowly pushed to the left until the two left most edges of the SCµM chip and cassette motor chip engaged the unlatch mechanisms holding back the socket clamps. The sockets and cassette were all designed so both unlatch mechanisms could engage at the same time, releasing the clamps simultaneously. The CMOS ZIF socket clamp pushes against the back of the cassette with the designed 30mN of force. The second clamp, on the motor ZIF socket, also pushes against the cassette substrate. The combined force of the two clamps was enough to manually (with

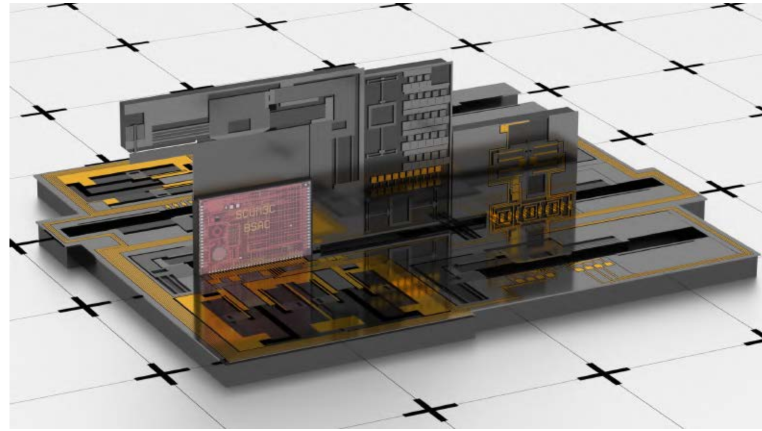

Figure 3.12: A 3D model of the MEMS-CMOS assembly using a MEMS cassette to hold a CMOS chip, inserted into a ZIF socket.

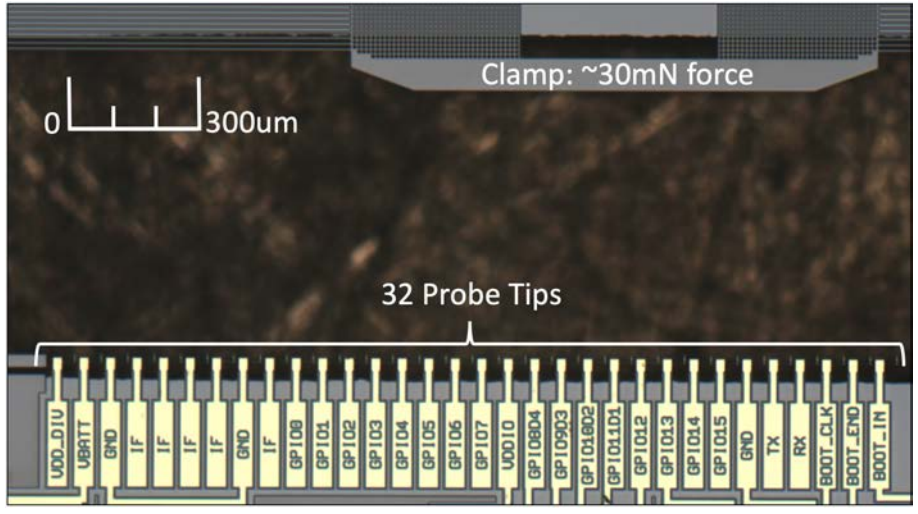

Figure 3.13: Top down microscope image of the 32 probe tips and the clamp on the CMOS compatible ZIF socket.

tweezers) pick up the assembled system by an edge of the cassette, Fig. 3.11b. This assembly could be rotated around and manipulated without falling apart, all while being held into place by only the two ZIF socket clamps.

A top down microscope image, Fig. 3.13, shows the 32 ZIF socket probes, before assembly, designed to precisely align with the 32 SCµM pads. Less than five assembly steps was required to make all 32 connections. To confirm probe to pad alignment after assembly, a 45º mirror was angled with tape in front of the fully assembled system, and under a microscope, using the setup seen in Fig. 3.14a. A top down microscope image first taken directly above the probe tips without an angled mirror confirms that they are engaged, Fig. 3.14b. The key giveaway to confirm the probe tips are engaged is their shape. The two fixed-guided beams

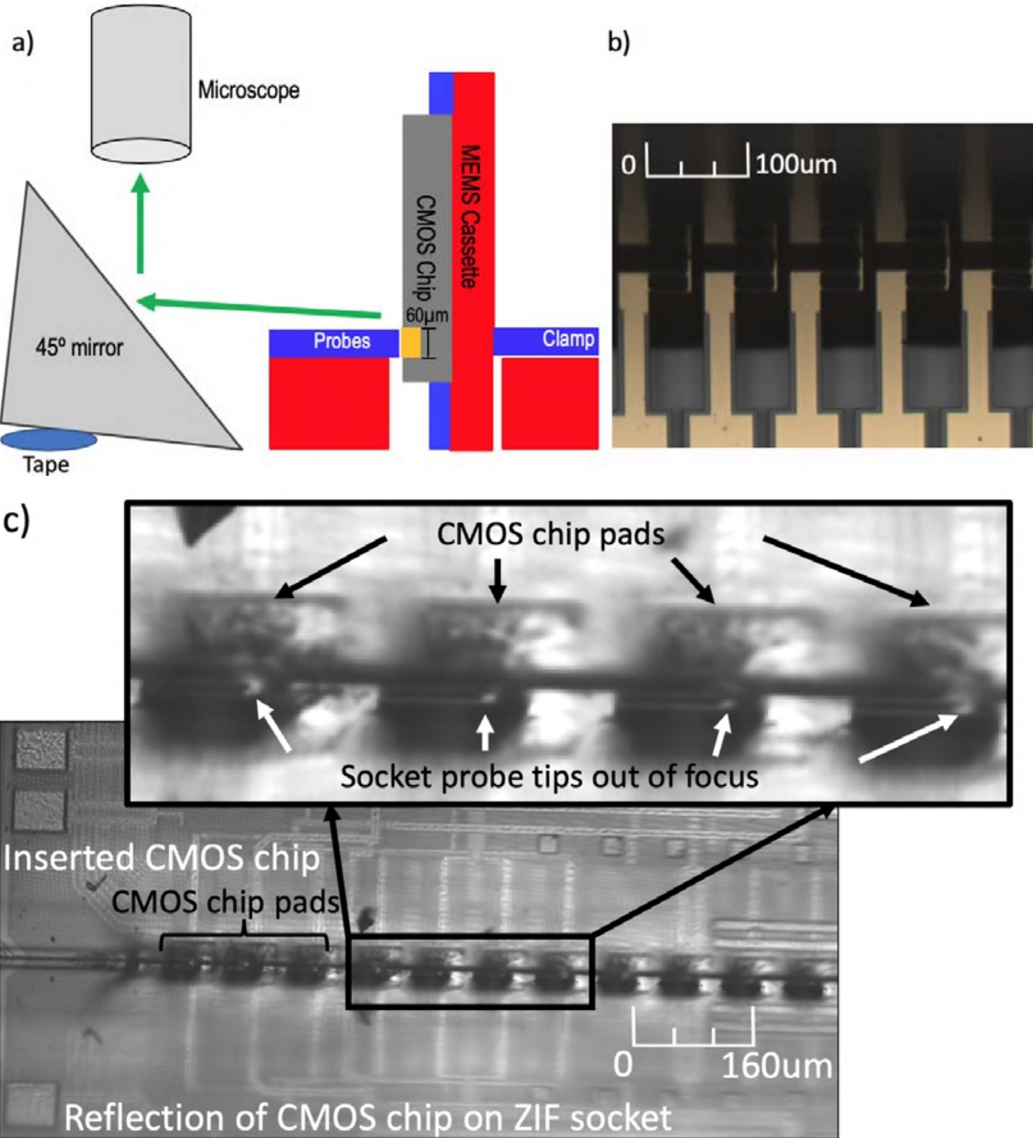

Figure 3.14: a) The test setup used to confirm alignment between the probes and pads. The 45º mirror is slightly angled with tape to be able to see the connection. b) The engaged ZIF socket probes after assembly. The probe tips at the top of the image are simply the reflection of the vertical CMOS chip. c) Microscope image from the setup in a). The SCµM pads are 53µm by 65µm pads on an 80µm pitch. The image is shown in grayscale to more easily recognize the probes.

that make up each probe tip are not straight, but rather curved due to the applied clamping force. Additionally, the reflection of the probe tips occurs due to the shiny surface of the inserted chip. When the probe tips look as if they are in contact with their reflection, it can be deduced that the inserted chip is also engaged with them. Moving the microscope to

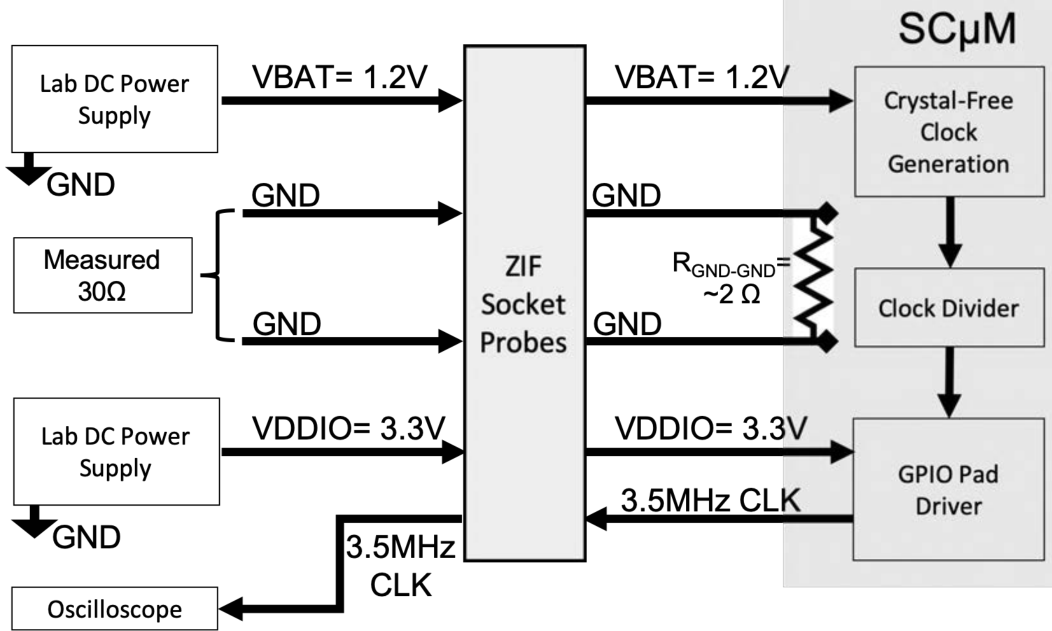

Figure 3.15: A schematic of the setup used to read a CLK signal from the SCµM chip.

the position in Fig. 3.14a, Fig. 3.14c shows the interface where the inserted SCµM chip is perpendicular to the ZIF socket, and the probes make contact with the pads. The SCµM pads (black arrows) can be seen above the probe tips (white arrows) in the close-up image in Fig. 3.14. The probes are out of focus due to the angle of the mirror, yet precisely aligned and centered to the SCµM pads as designed and intended.

Although very encouraging, qualitative results such as a system that can be manually manipulated without falling apart, Fig. 3.11b, or accurate alignment of probes to pads, Fig. 3.14a,b, are not enough to validate MEMS-CMOS integration. Two electrical test experiments were conducted to confirm electrical connections were properly achieved between the ZIF socket and the SCµM chip, Fig. 3.15. As mentioned in section 3.2.1, SCµM has multiple ground (GND) pads on the bottom row connected to each other. The resistance between two of the GND pads was measured before and after assembly using a Keithley 2634B Source Meter. Before assembly, the measured resistance, $R_{GND-GND}$, was about 2-3 ohms. Post assembly and through the ZIF socket probes, the measured resistance, $Ra_{GND-GND}$, was about 30 ohms. If $R_{GND-GND}$ is 2 ohms, the total contact resistance of the ZIF socket can be calculated to be $R_{totalcontactresistance}$= 28 ohms. Since two probes are used, the contact resistance for one ZIF socket probe is calculated to be about $R_{contactresistance}$= 14 ohms. This value is well under the maximum resistance allowed for the system to work that was estimated in section 3.2.3.

Fig. 3.15 shows the second test setup used to confirm successful MEMS-CMOS electrical integration after assembly. When SCµM is powered with 1.5V for battery power, GND, and 3.3V for the GPIO pins, the ARM Cortex M0's 3.3MHz clock signal can be seen output at

Figure 3.16: The 3.6MHz clock signal seen out of SCµM's GPIO 12 pin.

GPIO 12 pin. The ZIF socket probe tips were designed with large pads anchored to the substrate at the end not connected to SCµM for testing purposes. Tungsten probes at a probe station were used to connect to these large device layer pads on the ZIF socket, essentially also connecting to SCµM all through the ZIF socket. After the assembly, the two voltages and GND were applied through the ZIF socket, and the output from GPIO 12 was connected to an oscilloscope. A clock signal of roughly 3.6MHz was seen, Fig. 3.16, indicating successful MEMS-CMOS integration using ZIF sockets. Both the resistance measurements and clock signal test setups were dis- and re-assembled, and reproducible at least three times times. In addition, the SCµM chip pads were disconnected from the probes and reconnected about five times by pushing the cassette and SCµM configuration back with a probe tip. This was done to confirm the electrical connections made through the ZIF socket were easily repeatable without having to re-do the entire assembly.

Chapter 4

Walking Silicon Microrobot

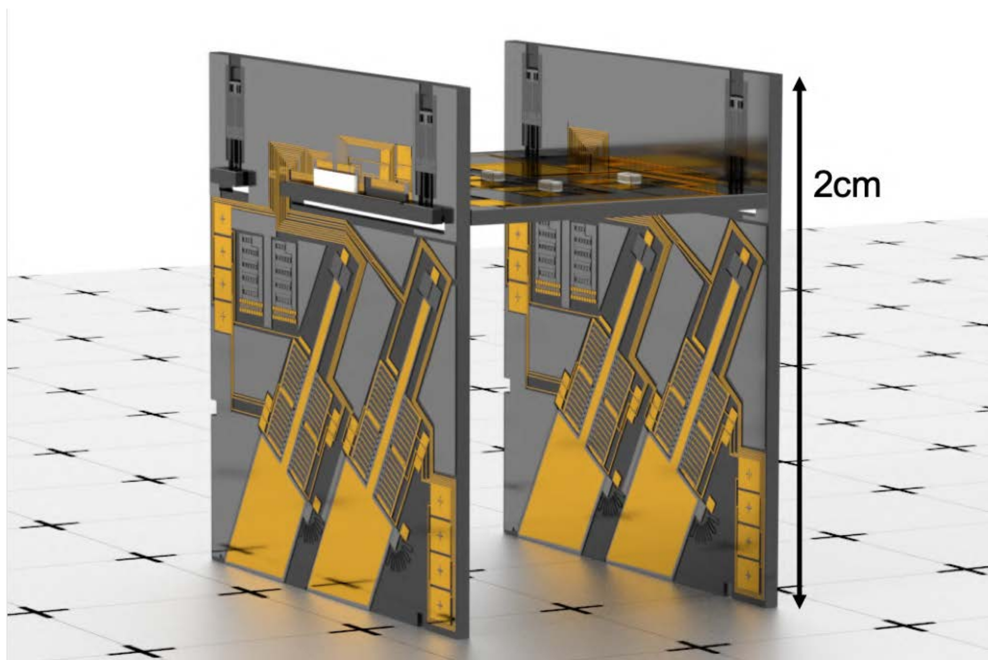

Figure 4.1: A 3D model of the walking silicon microrobot designed in this chapter. All the 3D renderings in this chapter were made using Blender.

Having shown successful MEMS-MEMS and MEMS-CMOS assembly using ZIF sockets and a MEMS cassette, it is possible to design and fabricate a completely untethered, full system walking microrobot. This chapter discusses the design considerations for a 2cm x 2cm x 1.5cm silicon microrobot fabricated using the same three-mask SOI process and manual assembly, Fig. 4.1. An improved assembly approach that uses a new version of ZIF sockets and assembly latches is also introduced. The microrobot discussed in this chapter has not yet been tested since it is currrently in fabrication, but preliminary results for the new assembly latches are presented.

4.1 Full System Overview

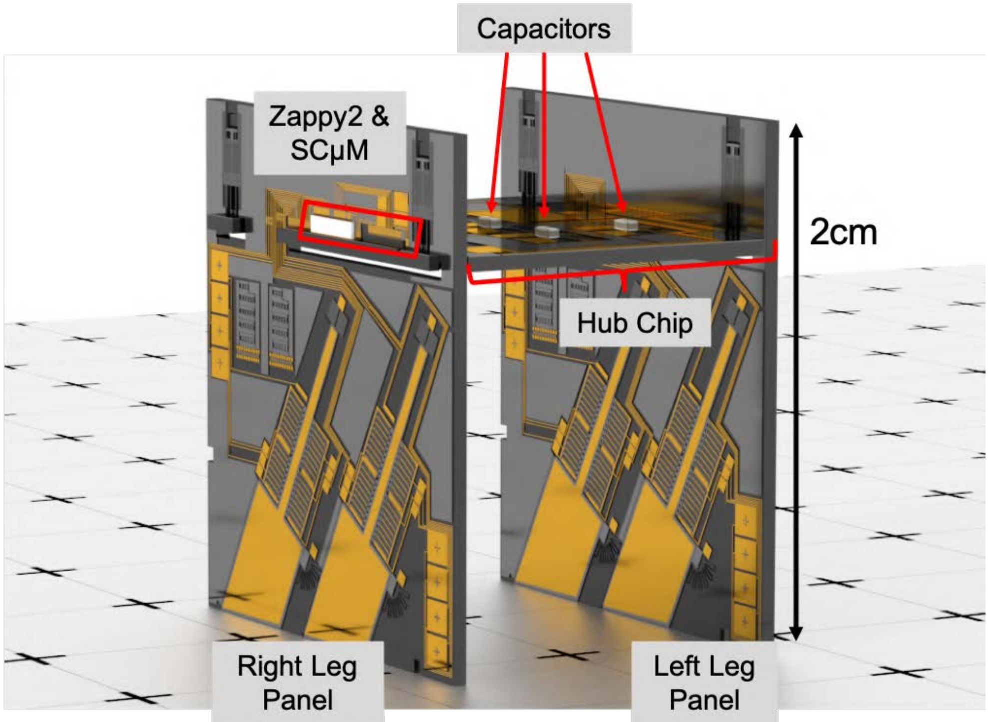

Figure 4.2: A copy of the 3D model in Fig. 4.1 with each individual component labelled.

The microrobot designed in this chapter includes a central hub chip that holds SCμM and Zappy2, two leg panels, four ceramic capacitors, and cassettes for both SCμM and Zappy2, Fig. 4.2. The electrical setup for the system is detailed further in the next subsection. In the physical space, in order to design for successful walking, it was important to ensure that the total robot payload is not too high to overcome the output force of the leg motors. The motors used in these legs are high force (millinewton) electrostatic actuators based on the designs developed in [37], [40]. The output force is directly proportional to the voltage squared, and up to 15mN of force has been shown at 100V [40].

Table 4.1 shows a tabulated summary of each component and its total mass and weight in milligrams and millinewtons, respectively. SCμM, Zappy2, and the ceramic capacitors were each individually weighed. Because the hub chip and leg panels have not yet been fabricated, their total mass was estimated using the layout area. 40μm was used as the device layer thickness, 550μm for the substrate thickness, and 2300 kg/m^3 for the density of silicon in the calculations from Table 4.1. The total weight of the final system was estimated to be about 17.3 mN.

Each leg in this robot was designed with one motor from [40], and there are two legs per side. More detail on the leg chips can be found in the sections below, but having a broad

understanding of the expected output forces is important for the overall design. The robot was designed with both the front and back legs for each right or left leg panel tied together. In other words, the right and left sides of the robot were designed to be able to output 30mN of force each, well over the estimated total weight of the entire system. Having confirmed that the appropriate motors and components are used in the mechanical space, being able to properly connect all the correct electrical signals is the next important step.

Payload		
Component	Total Mass [mg]	Total Weight [mN]
SCμM	4.3	0.04
Zappy2	17.3	0.17
Left Leg Panel	665	6.52
Right Leg Panel	661	6.48
Hub Chip	371	3.64
805 Capacitor (100nF)	17.2	0.17
805 Capacitor (100μF)	26.2	0.26
0402 Capacitor (22μF)	3.8	0.04
Total	**1766 [mg]**	**17.3 [mN]**

Table 4.1: Summary of system payload.

4.1.1 Full System Circuit

Fig. 4.3 shows a full system schematic of the electrical connections used for the control and power of the robot. The left side of the body represents the left leg panel, which contains the back and front legs. Two signals, B1 and B2, are used to run the motors through silicon jumpers. The silicon jumpers are essentially ZIF socket probes, modeled as resistors since their main electrical characteristic is contact resistance. All subsystems are also grounded through these jumpers. Very similar to the left side, the right side body contains the back and front legs connected to the motor signals, B3 and B4, through silicon jumpers. Unlike the left side though, the legs on the right side of the body contain a resistive end-of-travel sensor. This sensor is directly connected to a normally high input pin in SCμM, GPIO13, and pulled to ground when the motor shuttle has reached its end-of-travel.

The hub chip section of the schematic contains Zappy2, SCμM, the external capacitors, and the silicon jumpers in the legs used to directly wire Zappy2 and SCμM pads together. SCμM is powered using at least 1.2V for VBAT, and its GPIO pad driver is powered using 3.3V for the GPIO voltage, VDDIO. GPIOs 8-11 are used to output the control signals for the motors, but the output voltage is 3.3V– too low to actually actuate the motors. Therefore, the output of each GPIO 8-11 is connected to a high voltage buffer in Zappy2, HV Buffer

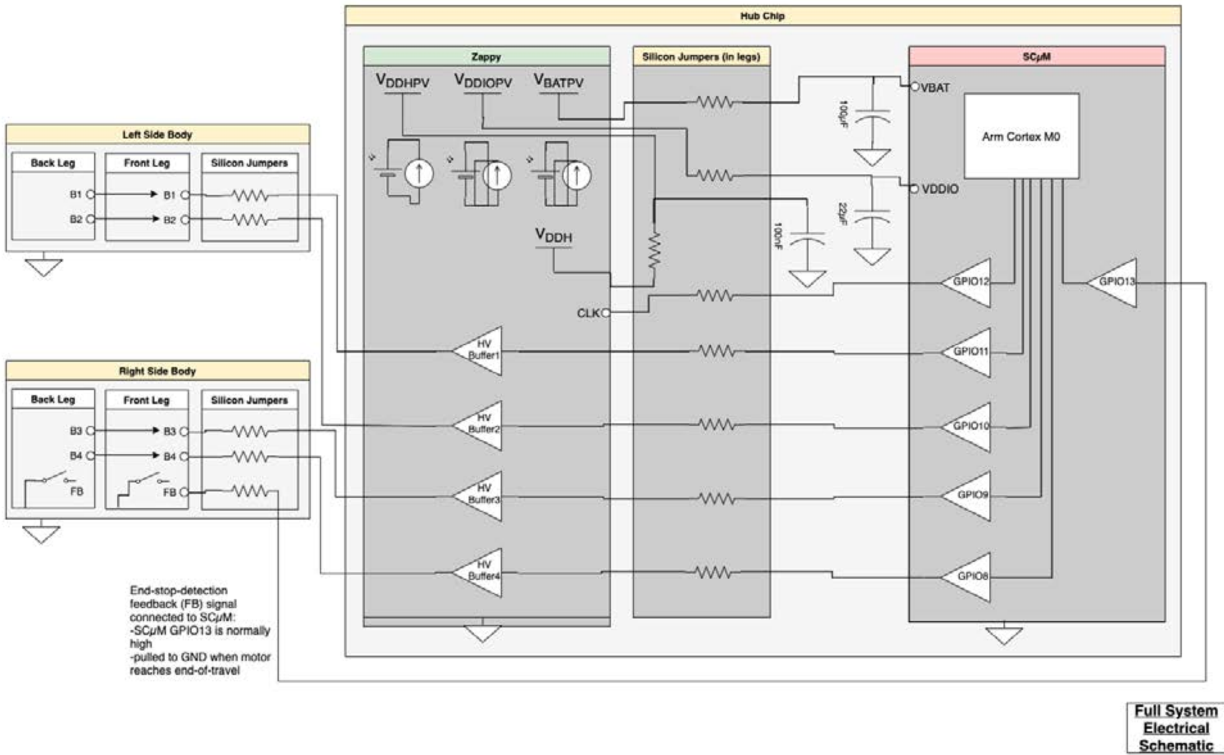

Figure 4.3: A complete electrical circuit schematic for the walking microrobot system.

1-4. Finally, SCμM provides Zappy2 with a CLK signal required for its internal digital state machine [41], output from GPIO12.

Zappy2 plays a large role in bringing all the pieces together in the electrical space. The solar cell outputs for the three power domains are: V_{DDHPV} for the high voltage buffers, V_{DDIOPV} to power SCμM's GPIOs, and V_{BATPV} to power SCμM. All the solar cell outputs are each connected through the silicon jumpers to capacitors, which are used to stabilize the system during any transients, such as SCμM turning on/off. The high voltage output in Zappy2 is wired through the jumpers back to Zappy2's input pad for the high voltage buffers. Finally, the high voltage buffers step up the 3.3V outputs from GPIOs 8-11 to 119V signals, B1-B4. The grounds of Zappy2, SCμM, the ceramic capacitors and the leg motors are also connected together. With the understanding of how all the subsystems are connected to each other, the next section takes a deeper dive into the design and assembly of the hub chip.

4.2 Hub Chip

Fig. 4.4 shows a top down 3D rendering of the hub chip without any assembled external components. The slots for Zappy2 and SCμM were both designed with clamps similar to the cassette design in Chapter 3. In this case, the hub chip acts as the cassette, and the

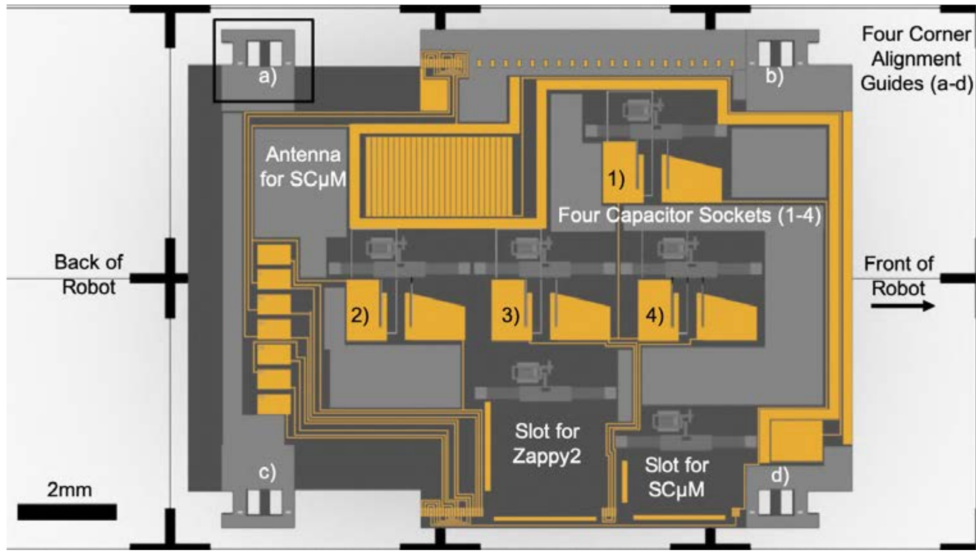

Figure 4.4: 3D Model: A top down view of the hub chip without external components.

"inserted" chips, Zappy2 and SCμM are facing up. This design decision is also favorable since it increases the amount of light Zappy2 will be exposed to, versus when on its side. Four capacitor sockets were included to clamp down on to ceramic capacitors. Three of them are for Zappy2's output voltages, and one is used for other debugging on SCμM. The four corners of the hub chip each contain alignment guides for the legs, so that the leg chips can be accurately assembled manually.

4.2.1 Antenna Design

An antenna was designed to connect to SCμM for wireless transmission, Fig. 4.5. The frequency the antenna was designed for is 2.4GHz, to be compatible with the standard 802.15.4 radio operation. This frequency corresponds to a wavelength of 12cm. The antenna was designed at half the wavelength, $\lambda/2 = 62.4$mm. A thin routing line connects the antenna to a device layer pad next to SCμM, at which point wire bonding is necessary to make a final connection, since the leg sockets only probe the bottom part of the SCμM chip. A wider ground loop was also included in the SOI layer around the antenna, in order to help isolate it from any parasitics in the hub chip.

4.2.2 Assembly and External Components

The first step in the assembly process is inserting all the external components in their individual slots or sockets. The top image in Fig. 4.6 shows the hub chip with the inserted external components and after assembly with the right and left leg panels. All the clamps in the hub chip were designed to exert about 30mN of force on each component– the beam design is the same one used in Chapter 2. However, the latch and release system was updated

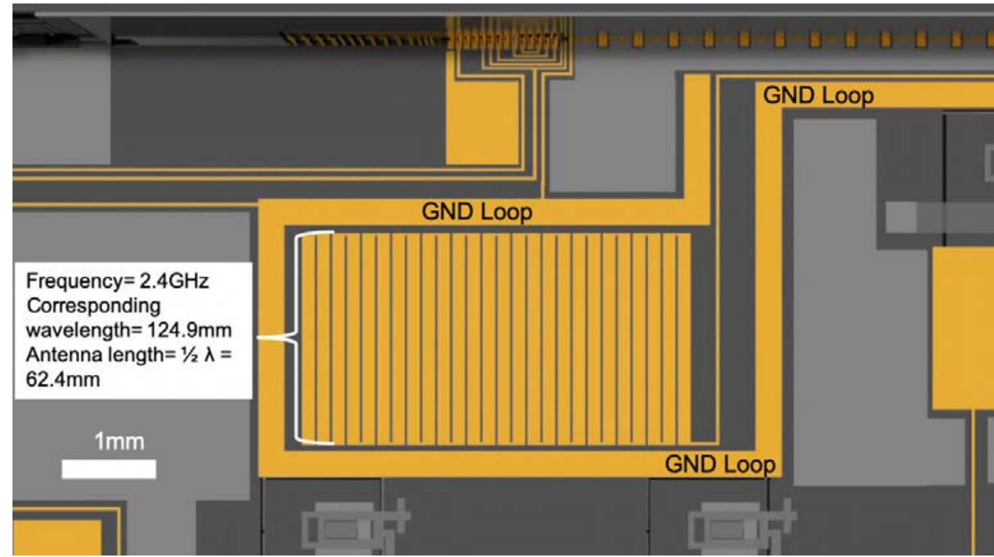

Figure 4.5: 3D Model: A top down view of the device layer antenna on the hub chip, designed to connect to SCµM.

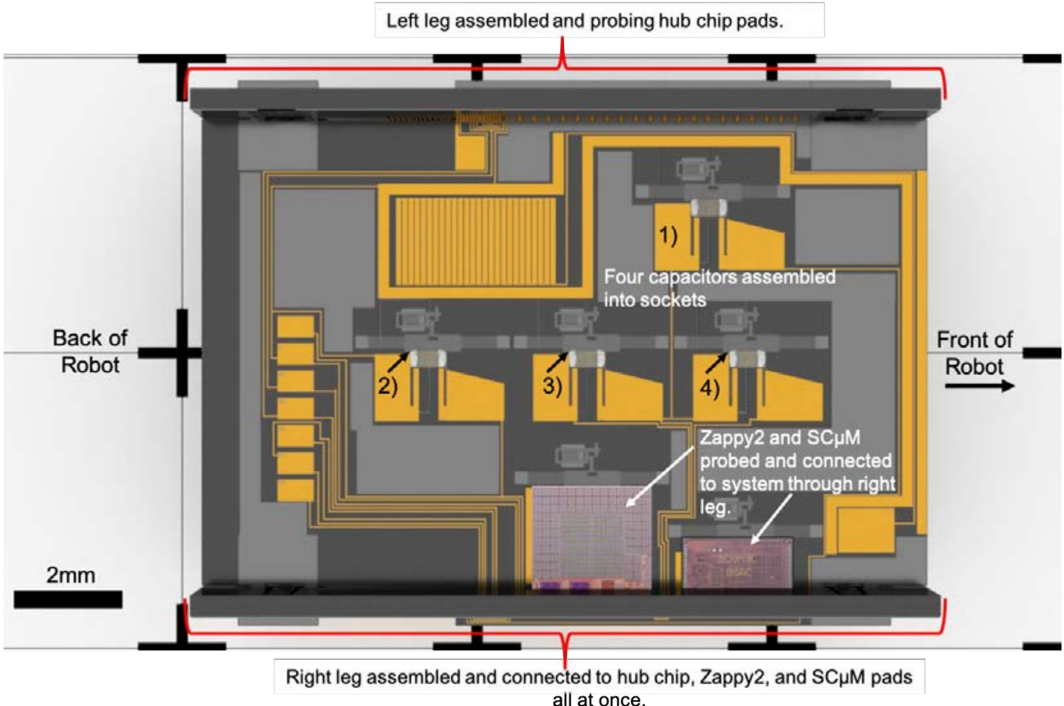

Figure 4.6: 3D Model: A top down view of the hub chip with the assembled external components and two leg panels.

to a smaller form factor. The capacitor sockets were designed with two device layer probes to make contact with each end of the capacitor. The clamp pushes the entire capacitor against the probes, isolating the mechanical from the electrical structures in these socket designs.

4.3 Leg Chips

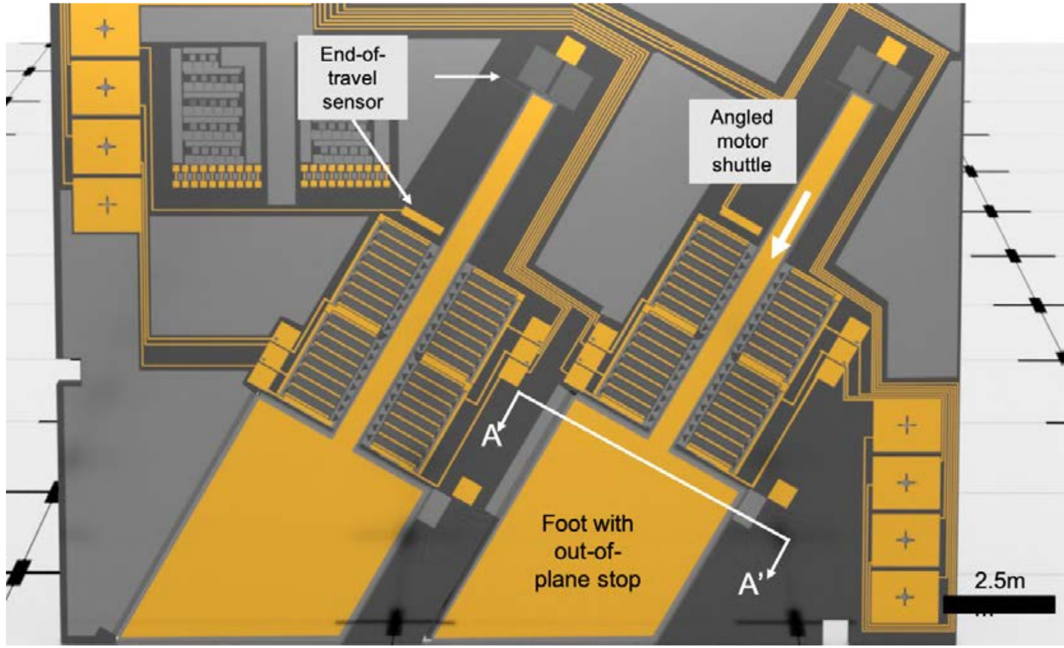

Figure 4.7: 3D Model: A top down view of the bottom portion of right leg panel.

Each leg panel was designed with three main objectives in mind: 1) actuation and leg design in order to move forward, 2) ZIF sockets and probes to electrically connect with the hub chip, SCµM, and Zappy2 chips, and 3) robust yet simple and streamlined mechanical assembly. Fig. 4.7 shows a top down rendering of the bottom potion of the right leg panel, which contains the linear MEMS actuators and two legs. Each leg contains one motor designed to output up to 15mN of force at 100V, based on the high force motor design in [40]. However, in this leg design, the shuttle of the actuator is 0.68mm, wider than in [40], in order to increase its robustness. Each motor shuttle is also angled so that the robot would be able to move forward with only one stroke. Therefore, the resulting leg has only one degree-of-freedom.

Previous leg designs such as the one in the silicon hexapod [5] used two motors to create walking motion with a two degrees-of-freedom leg: one downward to push the robot off the ground, and one to the side to create the sweeping motion required to move forward. By angling the legs with only one motor, the design in this chapter intends to create a similar step, but requiring fewer control signals. As mentioned above, the legs in each panel are

tied together, so one step can be taken on the left side, and another one on the right side at different times. This simplifies the total number of control signals needed to only four while theoretically still being able to move forward and sideways (left/right).

The end-travel-sensor can also be seen in Fig. 4.7. A small SOI beam attached to the shuttle near the top anchored springs acts as the resistive MEMS sensor. This beam travels with the shuttle and makes contact with an end-stop-detector anchored SOI pad. The pad is directly connected to GPIO13 through the leg panel probes, which can be set to normally high. Since the motor shuttle is always grounded, this feature can be used to pull GPIO13 to GND and act as a sensor feedback signal. The SCµM GPIO13 pad can be set to be normally high, and pulled low by the resistive contact with the grounded motor shuttle.

Finally, since the same fabrication process from section 1.4.1 is used to make the hub chip and two leg panels, out-of-plane motion is still an issue. Two potential solutions were designed to prevent the legs from popping out of plane during actuation. The first solution was to design a cap for the leg chips, which can be silver epoxied or flip-chip bonded on to the legs using the large "+" marked pads on the left and right sides of the panel. The second solution was to interweave the device and substrate layers of the foot with those of the leg panel using methods previously used in literature [42, 40]. Both examples also using a two layer SOI and subtrate fabrication process, Kilberg et al. created a structure that could hold an assembled MEMS air foil, and use a MEMS motor to rotate it without popping out of plane [42]. Schindler et al. developed a gripper mechanism with the central motor shuttle attached not only to the SOI layer, but also to the substrate layer [40]. Up to 3mm of the substrate and shuttle displacement was demonstrated.

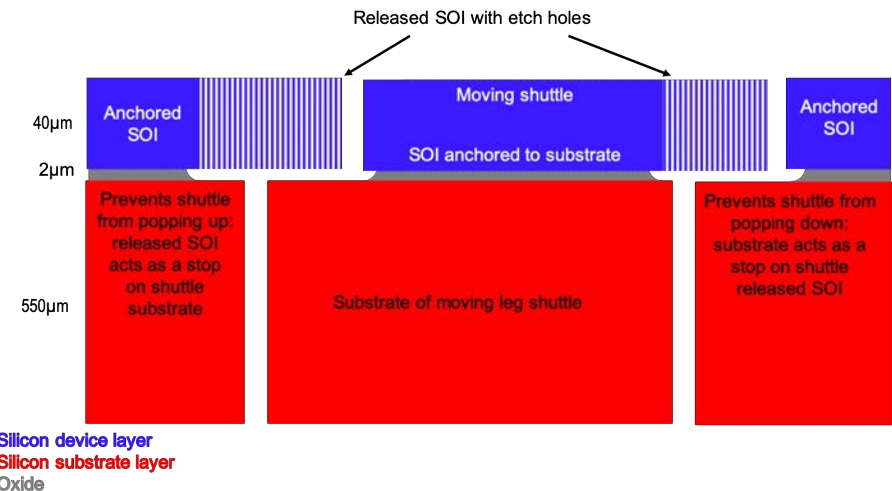

Figure 4.8: A drawing of the foot cross-section, A-A' from Fig. 4.7.

To better explain what "interweaving" the two layers really means, Fig. 4.8 shows cross-section A-A' from Fig. 4.7. On the left side of the foot, an SOI piece is partially anchored down to the leg panels and partially released with etch holes above the substrate of the foot.

This prevents the feet and shuttles from popping up (when referring to the cross-section). On the right side of the foot, an SOI piece is anchored to the shuttle's substrate layer, but is released and overhangs on top of the leg panel's substrate layer. This was designed to prevent the foot from popping down. Solely in regards to assembly, this second solution is more preferable since it requires less assembly steps and parts than the first one. However, it is important to be aware that friction forces from the stop could negatively affect the leg design and reduce actuation efficiency. In general past test structures have shown that friction at such small scales might be negligible [43, 8], but the silicon sidewall friction values have not yet been thoroughly characterized.

4.3.1 ZIF Sockets and Silicon Jumpers

Both the right and left legs contain all the necessary jumpers required to make the connections from Fig. 4.3. In this system, the left leg only connects to the hub chip directly, but the right leg was designed to connect to the hub chip as well as SCµM and Zappy2 all at once. Fig. 4.9 shows two renderings of the top right part of the right leg panels. The top rendering depicts the chip in its state before assembly. Two different sockets were made for Zappy2 and SCµM. Each socket design was based on the thickness of each chip, and contains probes to make contact with the bottom row of each chip. Additionally, SOI alignment tabs were included to slide into slots in the hub chip, resulting in an alignment accuracy that corresponds to the minimum feature DRIE etch accuracy of the SOI layer in the fabrication process, ±0.5µm.

The bottom 3D rendering in Fig. 4.9 shows the chips in their post-assembly state. Zappy2 and SCµM sit on the hub chip sockets. The leg chip probes make contact with the SCµM, Zappy2 and hub chip pads from the top down, connecting the entire system in one assembly step without any wire bonding or silver epoxy. The last step after assembly is the manual engagement of the latches at each one of the four corners. The latches were designed for manual engagement using tweezers, or at a probe station using a probe tip. A deeper dive into the latches can be found in the next section.

4.3.2 Substrate Latches

Studies and designs have been carried out to create strong mechanical connections between micro parts using snap-in and lock mechanisms. In some cases, these 3D structures also provide an electrical connection [44, 45, 27, 46, 47]. However, with the exception of [44], most of these connections are demonstrated using a specific application and are limited to simple architectures. Furthermore, unlike the examples in the literature, the latches used for mechanical assembly in this robot are designed in the more robust and thicker 550µm silicon substrate layer. Most of the subsystems designed in this chapter have not yet been tested or fabricated, but test structures for proof-of-concept and preliminary results for the latches were. Fig. 4.10 shows on the left a microscope picture of a fabricated latch, and a corresponding drawing of said latch on the right. The fabricated latch shown has a beam width of 40µm. SOI springs are used to anchor the latch to the leg panel, as well as pull it up

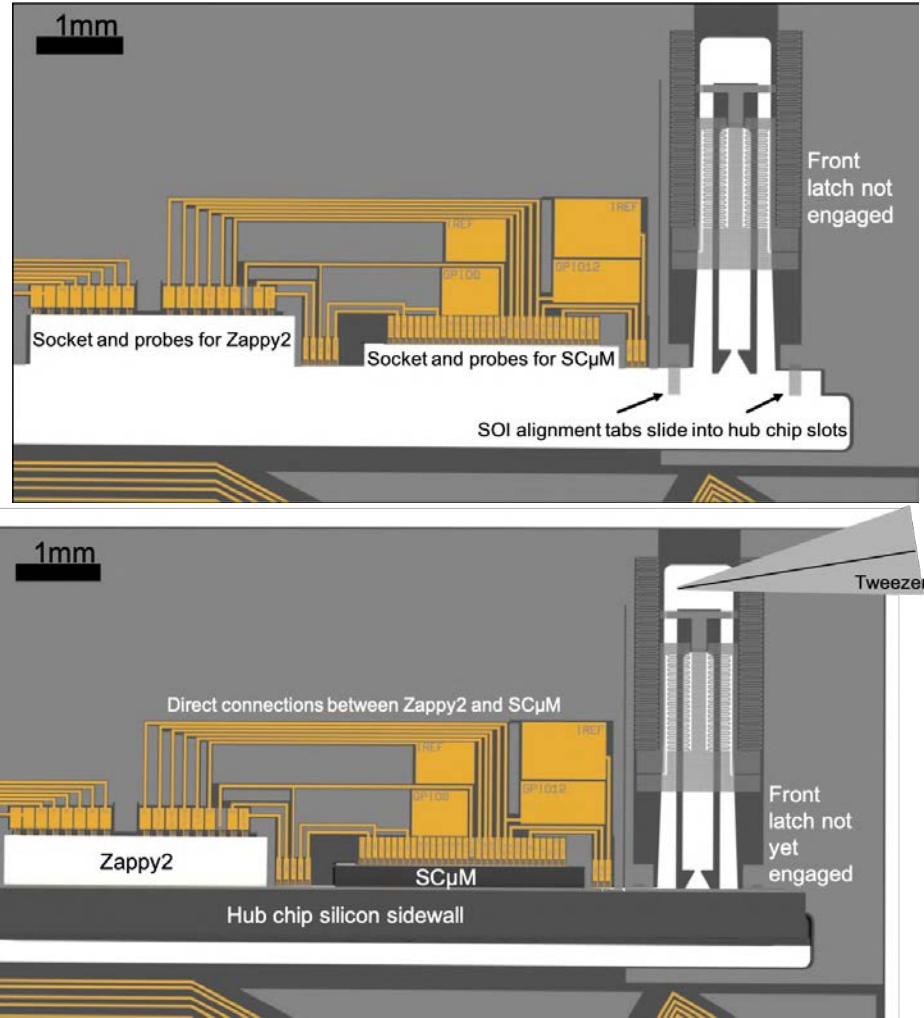

Figure 4.9: 3D Model: A top down view of the sockets, probes and assembly latches designed into the right leg. Top: before assembly with the hub chip. Bottom: after assembly with the hub chip, SCµM and Zappy2.

after engagement. These springs pull the hub chip into the probes with the necessary force, to mechanically integrate it with the leg chip at 90º.

In the MEMS world, it is not as common to use the substrate layer of an SOI wafer for mechanical structures as it is to use the device layer. For example, some of the first ever substrate springs were just recently demonstrated by Schindler et al. [37, 48]. The maximum strain for the single crystal silicon substrate is not a well characterized parameter, but it was an important one to consider when designing assembly latches like these. If not designed properly, the latches could break due to too much applied strain.

As a first attempt to characterize the substrate strain and physically assemble two chips using this new method, a latch test structure chip was developed along with a test hub chip

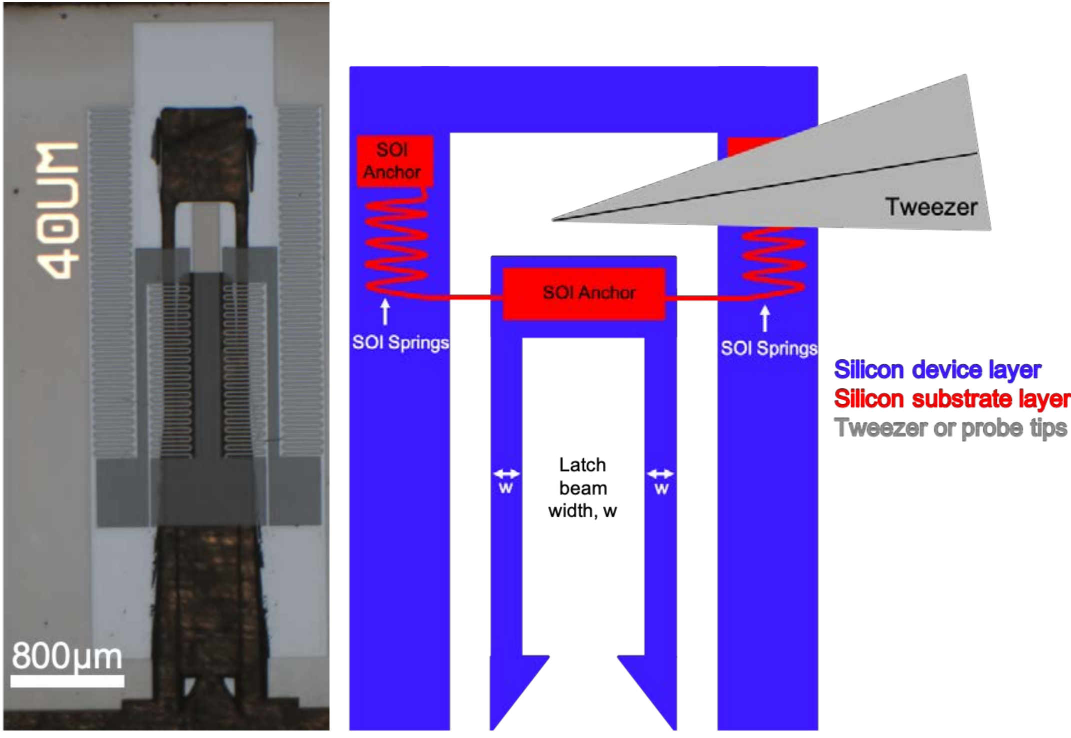

Figure 4.10: Left: a microscope picture of a fabricated latch. Right: a corresponding schematic. The 40µm gold marking indicates that the beam width of this latch was designed as 40µm wide.

Figure 4.11: Left: a camera picture of the fabricated latch test structures, with the first latch engaged. Right: a microscope image of the bottom ends of the first latch poking through the hub chip, as well as reflecting off of it.

structure, Fig. 4.11. The latch test structure chip contains five latches with increasing beam widths, while all other parameters are held constant. This corresponds to an increasing applied strain on the latches during assembly. In Fig. 4.11, the first latch has been pushed down and is engaged. The latch ends can be seen underneath the hub chip in the camera image on the left, and a microscope image on the right shows a closer view at the latch ends. Similar to the ZIF socket probes after assembly, the latch ends reflect off of the hub chip in the microscope image on the right.

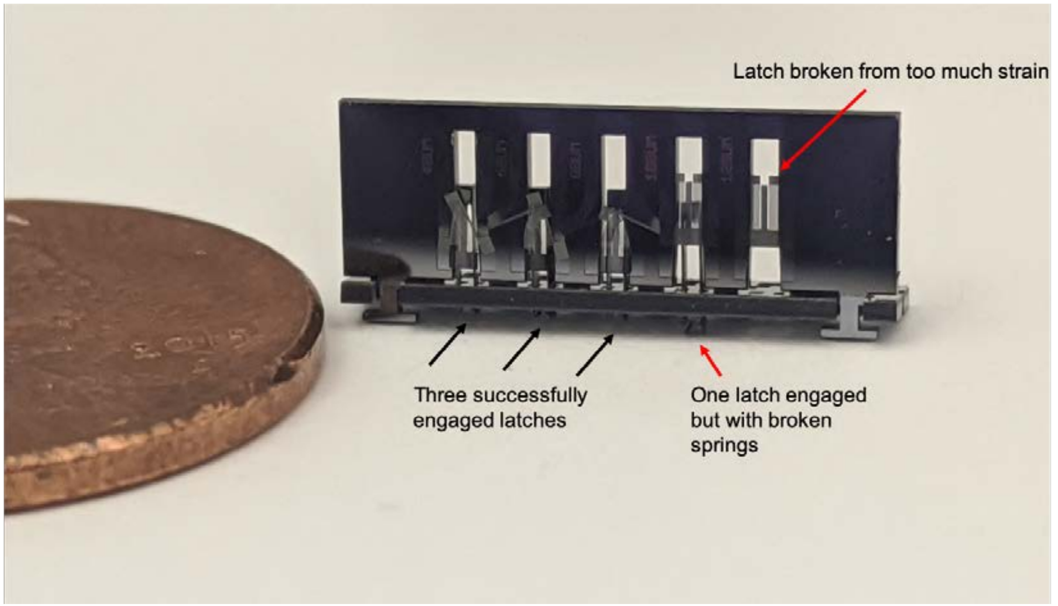

Figure 4.12: A summary of the results from testing the latch test structures.

Fig. 4.12 shows a summary of the results from the latch test structures. The resulting assembly has been placed next to a US penny. All of the five latches were engaged manually and using fine tip tweezers. The first three latches (w= 40µm, 60µm, 80µm) engaged successfully and pulled on to the hub chip. The third latch (w=100µm) also engaged successfully and without breaking. However, the SOI springs attached to the fourth latch broke off from the anchor, and the latch is therefore not pulling on the hub chip. The fifth latch broke from too much strain on the latch beams. Fig. 4.13 shows a plot of the calculated strains [%] (x- left axis), and theoretical forces applied on the latch during assembly [mN] (o- right axis), vs the increasing latch beam widths [µm]. The strain and force values corresponding to the first three engaged latches in circled in black. The broken latch can also be seen, circled in red. As seen on the plot, this fifth latch design corresponds to a designed maximum strain of 0.37%.

With test structures such as these, it is possible to begin to better characterize the maximum strain of the silicon substrate, and therefore optimize the latch design used for assembly. The results in Fig. 4.13 only show the theoretical strain and force values that the latches were designed for. No process effects such as overetching, footing or tapering from the deep DRIE backside etching of 550µm of silicon were taken into account for these

calculations. The next steps for these test structures should be to better characterize the etch profile and resulting beam width and shape. This way, more accurate calculations for maximum strain can be made. The next steps with the assembly latch design should be to develop a new set of test structures that take a closer look at the strain between the latches that engaged without any issues, versus the one that broke.

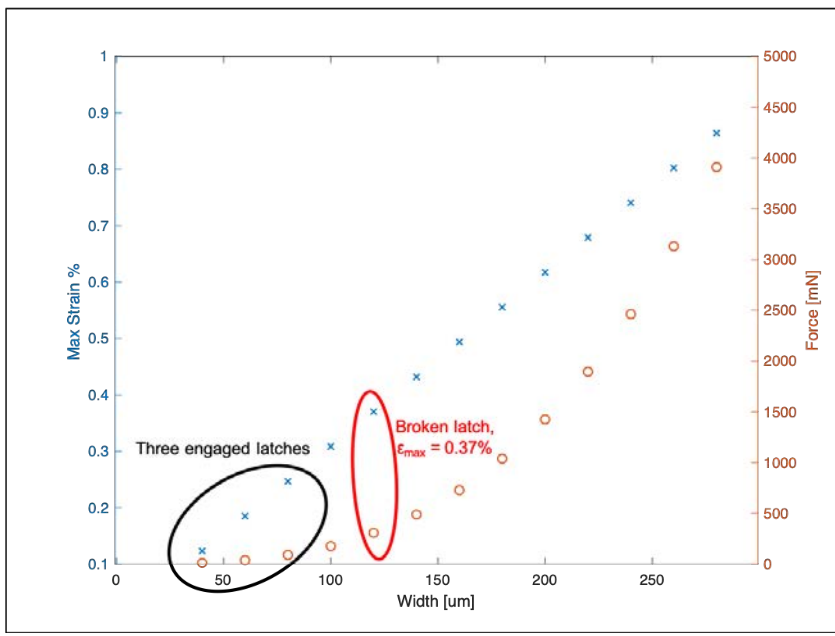

Figure 4.13: A plot of the calculated strains and theoretical applied forces on the latches vs the increasing latch beam widths.

Chapter 5

Conclusion

The ability to easily assemble microrobots and MEMS devices is a large step towards the ability to mass produce such systems. This work has shown that it is possible to mechanically integrate microrobots and MEMS devices manually and electrically as easily as it is to put together Legos. It is no longer necessary to take individual assembly steps, such as wire bonding or silver epoxying, to connect each signal together for all the subsystems. The assembly for tens of electrical signal connections all at once using ZIF sockets has been demonstrated, reducing the total number of assembly steps.

This work presented both MEMS-MEMS and MEMS-CMOS assembly using silicon ZIF sockets made in a three-mask SOI fabrication process. Using test structures, the contact resistances for the socket probes were shown to be as low as 14 ohms. MEMS-MEMS assembly was validated by integrating both a MEMS linear electrostatic motor and a microrobot silicon leg with ZIF sockets. Proof-of-concept for MEMS-CMOS assembly was demonstrated by integrating the SCµM chip with a ZIF socket, using the help of a MEMS cassette for vertical probe-to-pad alignment. Finally, an untethered full system microrobot was designed, and first results for a new substrate latch assembly method were presented. The full system is currently in fabrication.

Although this work confirmed the ability to assemble MEMS and CMOS devices in the 3D space, the fabrication process used to make the ZIF sockets, hub chip, and MEMS actuators, still comes with its disadvantages. With the current three-mask SOI process, there is still only one routing layer, an issue that in this work was resolved using silicon jumpers. Additionally, the device layer features are still able to pop out-of-place. This second issue was solved by the interweaving of the substrate and device layers, shown in the design of the quadruped foot from section 4.3. However, being able to fabricate MEMS structures with an additional second routing layer would prevent the need for creative solutions like the ones above. The section below briefly discusses the design of a seven-mask SOI fabrication process that could allow for a third routing plane on the MEMS devices.

5.1 Seven-Mask SOI Process

A third plane on top of the MEMS' device layer could be useful for: 1) an electrical cross routing plane, 2) a protective cap layer for the device layer, and 3) a second device layer. A few similar fabrication processes can be found in the literature and commercially available: the MEMSCAP polyMUMPS process [49], the Sandia National Laboratories Summit V process [50], and the epi-seal process fabricated at Stanford University [51, 52]. All of these have more than just two layers of silicon that can be used as a device layer or cap, depending on the process. However, the polyMUMPS and Summit V processes use thin (1-2µm) layers of polysilicon for the devices [49, 50], which would be a disadvantage to achieving higher force motors since it reduces the actuator capacitor overlap area [8]. Finally, the epi-seal process offered at Stanford university is a step closer to the desired cross-section. However, instead of using a backside etch to separate the devices into chiplets, this process fully encapsulates the devices and then dices them apart [51, 52]. This approach keeps the device layers contained, something very useful for sensor applications, but not as desirable for the microrobot applications in this work.

Cross sections for part one of the seven-mask fabrication process steps can be seen in Fig. 5.1. (Misalignment is exaggerated in the cross sections.) The seven-mask process begins with two SOI wafers, twice as many as the three-mask SOI process. The second SOI wafer will be used in two parts: the device layer will become a routing layer for the MEMS devices, and the substrate layer can be used as a handle wafer during one of the etching steps in the fabrication process. This is discussed further below.

Step two in the process is the low pressure chemical vapor deposition (LPCVD) of silicon nitride on both of the wafers. Just 0.5µm of silicon nitride can act as an optional insulation layer between the device and the routing layers. This nitride can be defined using reactive ion etching (RIE). This etch is defined using the first two masks, Device Si_xN_y and Routing Si_xN_y. In step number three, a 0.5µm metal gold layer is evaporated using e-beam evaporation, and defined using liftoff as well as the Device MET and Routing MET masks.

Fig. 5.2 shows part two of the process. After depositing and defining the two layers, the masks named Device SOI and Routing SOI can be used during the photolithography portion of the frontside silicon DRIE etch, step four. To anchor the silicon routing layer to the device layer, step five is a gold-gold wafer bond. Using a wafer bonder such as the AML AWB-08 Wafer Bonder found in the Marvell Nanolab, anecdotally 10µm of alignment precision can be easily achieved, and the tool's alignment limit is 2µm. This bond not only mechanically integrates the two layers together, but also electrically connects them wherever silicon nitride was not placed to act as an insulator.

At this point, the silicon substrate holding the routing layer can be used as a handle wafer for the top substrate etch. The first etch for the top substrate in this process is a potassium hydroxide- KOH blanket thinning. This step was designed to reduce the substrate layer thickness to 100µm in order to reduce the overall mass of the resulting chips, as well as improve the aspect ratio of the DRIE backside substrate etch. The device and routing layers can be bonded with a ring around the entire wafer in order to protect the devices inside the

bonded wafer. After the substrate thinning, the handle wafer can be used for the second substrate etch: DRIE etching of the now 100µm thick layer. With an etch aspect ratio of 20:1, this would result in a new backside minimum feature size of 5µm.

Finally, the last step in the process is the oxide release. Because there are various unknowns to this etch, it is important to note that this part of the process is overly simplified in the cross sections, as well as in this section. There are two objectives to this last etch: 1) release the device layer from the 100µm thickness substrate wherever it has the required etch holes, and 2) release the routing layer from the handle wafer. The two objectives do not necessarily align with each other, since the routing layer has to release entirely from the handle wafer, but the device layer may need to stay anchored in places to the substrate.

This section does not intend to provide an answer to this challenge, but rather provide initial ideas that have been born throughout the design of this process. One possible solution is designing the routing and device layers with different sized etch holes. Additionally, the handle and routing wafer could be purchased so that the bond between the two layers is not as strong as the bond between the device and substrate wafer. This is not a well studied approach, but rather a cleanroom anecdote from past experience. Another possible issue with this step is the flow of HF inside the chambers now created between the bonded layers. More work needs to be conducted to examine if this would have any effect on etch rates and variances throughout the wafer.

5.2 Microrobot and IoT Researcher Responsibilities and Considerations

As highlighted in section 1.1.1, microrobots have the potential to be used for the betterment of humanity and research. However, as researchers and engineers, it is important to be conscious of the potential repercussions the developed technology can have. This is a preventative and mindful approach to developing technology rather than a reactive one. As microrobots continue to be developed in the MEMS field and beyond, accessibility to these systems has the potential to grow. As more micro systems and internet-of-things (IoT) devices are put out into the world, it is important to be aware of the potential environmental impact these devices can have. If they are not designed to be sustainable systems, these systems can become yet another contributor to environmental pollution. For the most part, the MEMS chips used in this project are harmless since they are made of silicon. Additionally, designing easily assembled modular systems allows for the reuse of microrobot parts if one subsystem is broken.

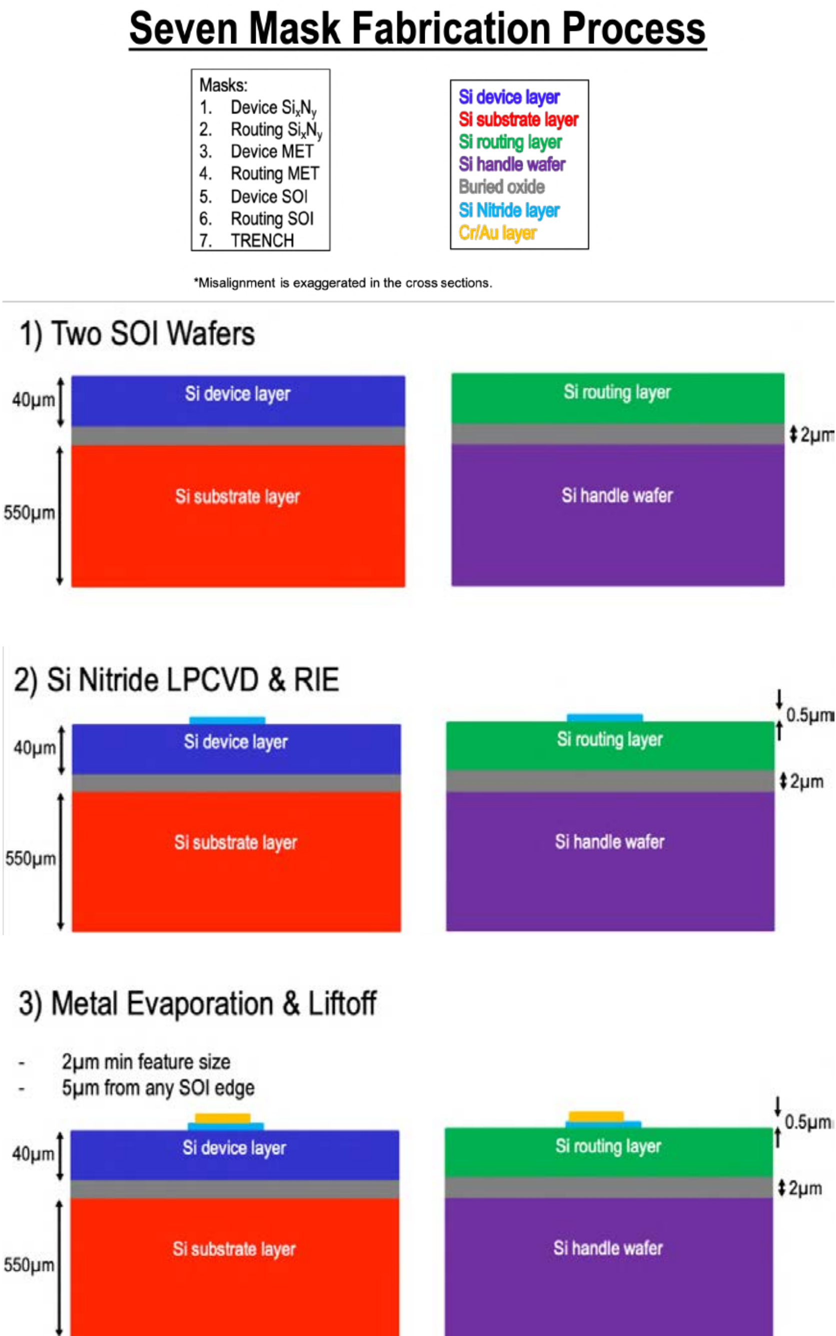

Figure 5.1: A step-by-step cross section of the seven-mask SOI process designed to add an additional routing and device layer, part 1.

Figure 5.2: A step-by-step cross section of the seven-mask SOI process designed to add an additional routing and device layer, part 2.

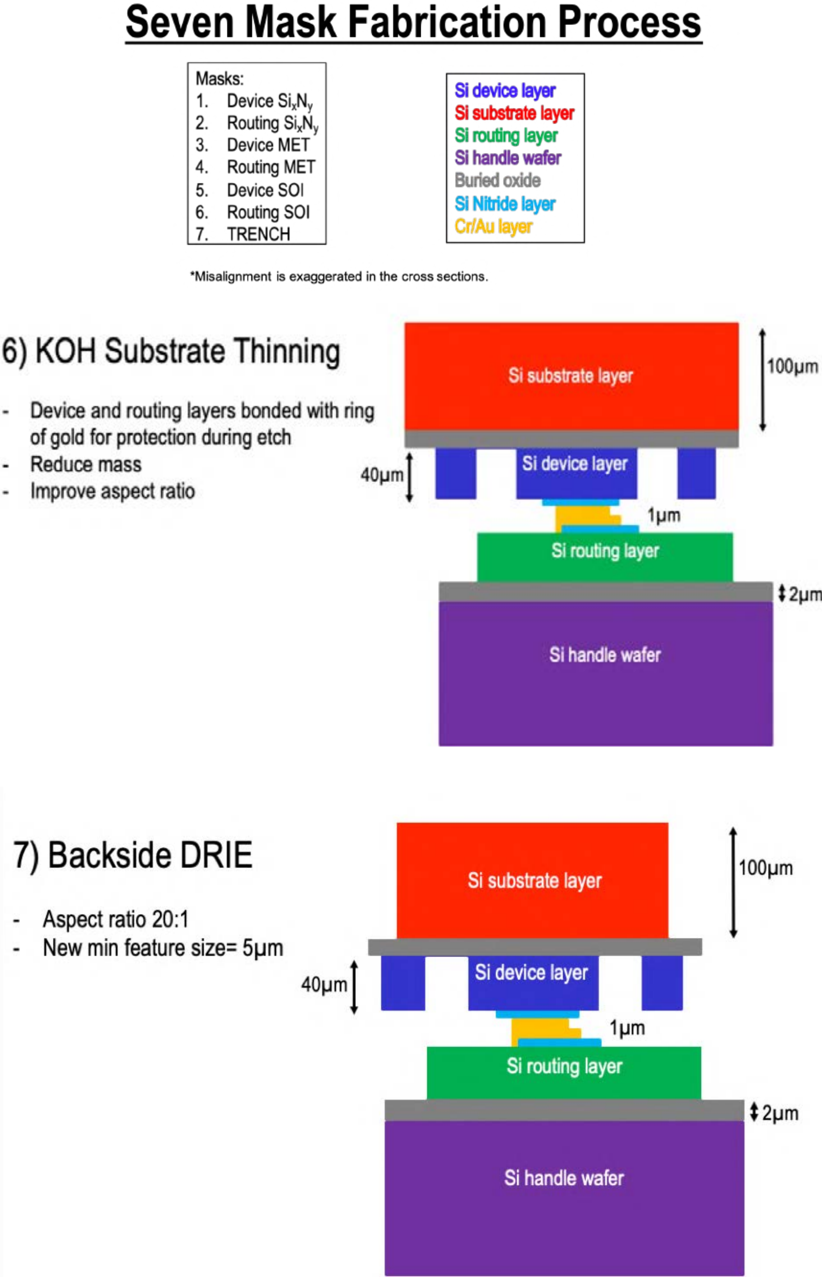

Figure 5.3: A step-by-step cross section of the seven-mask SOI process designed to add an additional routing and device layer, part 3.

Figure 5.4: A step-by-step cross section of the seven-mask SOI process designed to add an additional routing and device layer, part 4.

Bibliography

[1] G. Loussouarn, I. Lozano, S. Panhard, C. Collaudin, Charles el Rawadi, and G. Genain. "Diversity in human hair growth, diameter, colour and shape. An in vivo study on young adults from 24 different ethnic groups observed in the five continents". In: *European Journal of Dermatology* 26 (2016), pp. 144–154.

[2] C.R. Robbins. *Chemical and Physical Behavior of Human Hair*. Springer Berlin Heidelberg, 2012. ISBN: 9783642256110. URL: https://books.google.com/books?id=WLq0mUHSU7cC.

[3] Richard Pallardy. *Chile mine rescue of 2010*. URL: https://www.britannica.com/event/Chile-mine-rescue-of-2010. (accessed: 11.17.2020).

[4] Colin Renfrew, Paul G Bahn, and Paul G Bahn. *Archaeology: theories, methods and practice*. Vol. 2. Thames and Hudson London, 1991.

[5] Daniel S Contreras and Kristofer SJ Pister. "A six-legged MEMS silicon robot using multichip assembly". In: *Hilton Head Workshop*. 2018.

[6] J. S. Rentmeister, K. S. J. Pister, and J. T. Stauth. "A 120-330V, sub-µA, Optically Powered Microrobotic Drive IC for DARPA SHRIMP". In: *GOMACTech2020*. 2020.

[7] Filip Maksimovic, Brad Wheeler, David C Burnett, Osama Khan, Sahar Mesri, Ioana Suciu, Lydia Lee, Alex Moreno, Arvind Sundararajan, Bob Zhou, et al. "A crystal-free single-chip micro mote with integrated 802.15. 4 compatible transceiver, sub-mw ble compatible beacon transmitter, and cortex m0". In: *2019 Symposium on VLSI Circuits*. IEEE. 2019, pp. C88–C89.

[8] Daniel S. Contreras. "Walking Silicon: Actuators and Legs for Small-Scale Terrestrial Robots". PhD. EECS Department, University of California, Berkeley. URL: http://www2.eecs.berkeley.edu/Pubs/TechRpts/2019/EECS-2019-18.html.

[9] JT Greenspun and K Pister. "First leaps of an electrostatic inchworm motor-driven jumping microrobot". In: *Hilton Head Solid-State Sensors, Actuators, and Microsystems Workshop, Hilton Head Island, SC*. Vol. 3. 2018.

[10] Daniel S Drew, Nathan O Lambert, Craig B Schindler, and Kristofer SJ Pister. "Toward controlled flight of the ionocraft: a flying microrobot using electrohydrodynamic thrust with onboard sensing and no moving parts". In: *IEEE Robotics and Automation Letters* 3.4 (2018), pp. 2807–2813.

[11] Palak Bhushan and Claire Tomlin. “An Insect-scale Untethered Laser-powered Jumping Microrobot”. In: *arXiv preprint arXiv:1908.03282* (2019).

[12] Johannes James, Vikram Iyer, Yogesh Chukewad, Shyamnath Gollakota, and Sawyer B Fuller. “Liftoff of a 190 mg laser-powered aerial vehicle: The lightest wireless robot to fly”. In: *2018 IEEE International Conference on Robotics and Automation (ICRA)*. IEEE. 2018, pp. 1–8.

[13] Noah T Jafferis, E Farrell Helbling, Michael Karpelson, and Robert J Wood. “Untethered flight of an insect-sized flapping-wing microscale aerial vehicle”. In: *Nature* 570.7762 (2019), pp. 491–495.

[14] Seth Hollar, Anita Flynn, Colby Bellew, and KSJ Pister. “Solar powered 10 mg silicon robot”. In: *The Sixteenth Annual International Conference on Micro Electro Mechanical Systems, 2003. MEMS-03 Kyoto. IEEE*. IEEE. 2003, pp. 706–711.

[15] Anju Toor, Albert Wen, Filip Maksimovic, Abhinav. M. Gaikwad, Kristofer S.J. Pister, and Ana C. Arias. “Stencil-printed Lithium-ion Micro Batteries for IoT Applications”. In: *Nano Energy* (2020), p. 105666. ISSN: 2211-2855. DOI: https://doi.org/10.1016/j.nanoen.2020.105666. URL: http://www.sciencedirect.com/science/article/pii/S2211285520312398.

[16] Benjamin Goldberg, Raphael Zufferey, Neel Doshi, Elizabeth Farrell Helbling, Griffin Whittredge, Mirko Kovac, and Robert J Wood. “Power and control autonomy for high-speed locomotion with an insect-scale legged robot”. In: *IEEE Robotics and Automation Letters* 3.2 (2018), pp. 987–993.

[17] Mingjing Qi, Yangsheng Zhu, Zhiwei Liu, Xiaoyong Zhang, Xiaojun Yan, and Liwei Lin. “A fast-moving electrostatic crawling insect”. In: *2017 IEEE 30th International Conference on Micro Electro Mechanical Systems (MEMS)*. IEEE. 2017, pp. 761–764.

[18] Dana Vogtmann, Ryan St Pierre, and Sarah Bergbreiter. “A 25 mg magnetically actuated microrobot walking at> 5 body lengths/sec”. In: *2017 IEEE 30th International Conference on Micro Electro Mechanical Systems (MEMS)*. IEEE. 2017, pp. 179–182.

[19] Ryan St Pierre, Walker Gosrich, and Sarah Bergbreiter. “A 3D-printed 1 mg legged microrobot running at 15 body lengths per second”. In: *Solid-State Sensors, Actuators, and Microsystems Workshop, Hilton Head, SC*. Vol. 3. 2018.

[20] Allen Cowen, Greg Hames, DeMaul Monk, Steve Wilcenski, and Busbee Hardy. *SOI-MUMPs Design Handbook, Revision 8.0.* publisher: MEMSCAP Inc. URL: http://www.memscap.com/__data/assets/pdf_file/0019/1774/SOIMUMPs.dr.v8.0.pdf. (accessed: 11.17.2020).

[21] Colby L Bellew, Seth Hollar, and KSJ Pister. “An SOI process for fabrication of solar cells, transistors and electrostatic actuators”. In: *TRANSDUCERS’03. 12th International Conference on Solid-State Sensors, Actuators and Microsystems. Digest of Technical Papers (Cat. No. 03TH8664)*. Vol. 2. IEEE. 2003, pp. 1075–1078.

[22] J Greenspun, T Massey, and KSJ Pister. "The MEMS Hammer A tool to study microfracture". In: *Hilton Head 2016 Solid State Sensor and Actuator Workshop Technical Digest*. 2016.

[23] I Penskiy and S Bergbreiter. "Optimized electrostatic inchworm motors using a flexible driving arm". In: *Journal of Micromechanics and Microengineering* 23.1 (2012), p. 015018.

[24] Richard Yeh, Seth Hollar, and Kristofer SJ Pister. "Single mask, large force, and large displacement electrostatic linear inchworm motors". In: *Journal of Microelectromechanical Systems* 11.4 (2002), pp. 330–336.

[25] Stephen D Senturia. *Microsystem design*. Springer Science & Business Media, 2007.

[26] Joseph T. Greenspun. "Mechanical Energy Storage for Self-Destructing Motes and Jumping Microrobots". PhD. EECS Department, University of California, Berkeley.

[27] M Last, V Subramaniam, and KSJ Pister. "Out of plane motion of assembled microstructures using a single-mask SOI process". In: *The 13th International Conference on Solid-State Sensors, Actuators and Microsystems, 2005. Digest of Technical Papers. TRANSDUCERS'05.* Vol. 1. IEEE. 2005, pp. 684–687.

[28] Rama Prasad, Karl F Bohringer, and Noel C MacDonald. *DESIGN, FABRICATION, AND CHARACTERIZATION OF SINGLE CRYSTAL SILICON LATCHING SNAP FASTENERS FOR MICRO ASSEMBLY*. Tech. rep. Cornell University, 1995.

[29] J Liu, M Noman, JA Bain, TE Schlesinger, and GK Fedder. "Lever-based CMOS-MEMS probes for reconfigurable RF IC's". In: *2009 IEEE 22nd International Conference on Micro Electro Mechanical Systems*. IEEE. 2009, pp. 1111–1114.

[30] Gabriel M Rebeiz. *RF MEMS: theory, design, and technology*. John Wiley & Sons, 2004.

[31] Ragnar Holm. *Electric contacts: theory and application*. Springer Science & Business Media, 2013.

[32] MB Read, JH Lang, AH Slocum, and R Martens. "Contact resistance in flat thin films". In: Institute of Electrical and Electronics Engineers. 2009.

[33] HL Sun, ZX Song, DG Guo, F Ma, and KW Xu. "Microstructure and mechanical properties of nanocrystalline tungsten thin films". In: *Journal of Materials Science & Technology* 26.1 (2010), pp. 87–92.

[34] M Wen, QN Meng, WX Yu, WT Zheng, SX Mao, and MJ Hua. "Growth, stress and hardness of reactively sputtered tungsten nitride thin films". In: *Surface and Coatings Technology* 205.7 (2010), pp. 1953–1961.

[35] Hani C Gomez, Craig B Schindler, Harry L Clark, Joseph T Greenspun, and Kristofer SJ Pister. "Zero Insertion Force MEMS Socket: 3d Multi-Chip Assembly for Microrobotics". In: *2019 20th International Conference on Solid-State Sensors, Actuators and Microsystems & Eurosensors XXXIII (TRANSDUCERS & EUROSENSORS XXXIII)*. IEEE. 2019, pp. 1732–1735.

[36] Daniel S Contreras, Daniel S Drew, and Kristofer SJ Pister. "First steps of a millimeter-scale walking silicon robot". In: *2017 19th International Conference on Solid-State Sensors, Actuators and Microsystems (TRANSDUCERS)*. IEEE. 2017, pp. 910–913.

[37] Craig B Schindler, Joseph T Greenspun, Hani C Gomez, and Kristofer SJ Pister. "A jumping silicon microrobot with electrostatic inchworm motors and energy storing substrate springs". In: *2019 20th International Conference on Solid-State Sensors, Actuators and Microsystems & Eurosensors XXXIII (TRANSDUCERS & EUROSENSORS XXXIII)*. IEEE. 2019, pp. 88–91.

[38] Alex Moreno, Filip Maksimovic, Lydia Lee, Brian Kilberg, Craig Schindler, Hani Gomez, Daniel Teal, Dillon Acker-James, Andrew Fearing, Kristofer Pister, et al. "Single-Chip micro-Mote for Microrobotic Platforms". In: ().

[39] *X-FAB: SOI*. URL: https://www.xfab.com/technology/soi/ (visited on 12/18/2020).

[40] Craig B Schindler, Hani C Gomez, Dillon Acker-James, Daniel Teal, Wei Li, and Kristofer SJ Pister. "15 Millinewton Force, 1 Millimeter Displacement, Low-Power MEMS Gripper". In: *2020 IEEE 33rd International Conference on Micro Electro Mechanical Systems (MEMS)*. IEEE. 2020, pp. 485–488.

[41] Jan S. Rentmeister, M. Hassan Kiani, Kristofer S.J. Pister, and Jason T. Stauth. "A 120-330V, sub-μA, 4-Channel Driver for Microrobotic Actuators with Wireless- Optical Power Delivery and over 99% Current Efficiency". In: *2020 IEEE Symposium on VLSI Circuits*. Honolulu, HI, USA: IEEE, 2020.

[42] Brian Kilberg, Daniel Contreras, Joseph Greenspun, Hani Gomez, Eric Liu, and Kristofer SJ Pister. "MEMS Airfoil with Integrated Inchworm Motor and Force Sensor". In: *Hilton Head*. 2018.

[43] Daniel S Contreras and Kristofer SJ Pister. "Durability of silicon pin-joints for microrobotics". In: *2016 International Conference on Manipulation, Automation and Robotics at Small Scales (MARSS)*. IEEE. 2016, pp. 1–6.

[44] Nikolai Dechev, James K Mills, and William L Cleghorn. "Mechanical fastener designs for use in the microassembly of 3d microstructures". In: *ASME International Mechanical Engineering Congress and Exposition*. Vol. 47144. 2004, pp. 447–456.

[45] David Hériban and Michaël Gauthier. "Robotic micro-assembly of microparts using a piezogripper". In: *2008 IEEE/RSJ International Conference on Intelligent Robots and Systems*. IEEE. 2008, pp. 4042–4047.

[46] Mohammad Mayyas, Ping Zhang, Woo Ho Lee, Dan Popa, and JC Chiao. "An active micro joining mechanism for 3D assembly". In: *Journal of Micromechanics and Microengineering* 19.3 (2009), p. 035012.

[47] Kenneth Tsui, Aaron A Geisberger, Matt Ellis, and George D Skidmore. "Micromachined end-effector and techniques for directed MEMS assembly". In: *Journal of Micromechanics and Microengineering* 14.4 (2004), p. 542.

[48] Craig B. Schindler. "Jumping Silicon Microrobots With Electrostatic Inchworm Motors and Energy Storing Substrate Springs". PhD. EECS Department, University of California, Berkeley. URL: https://www2.eecs.berkeley.edu/Pubs/TechRpts/2020/EECS-2020-73.html.

[49] Allen Cowen, Busbee Hardy, Ramaswamy Mahadevan, and Steve Wilcenski. *PolyMUMPs Design Handbook*. publisher: MEMSCAP Inc. URL: http://www.memscap.com/__data/assets/pdf_file/0019/1729/PolyMUMPs-DR-13-0.pdf.

[50] MEMS Technologies Department. *SUMMiT V (TM) Five Level Surface Micromachining Technology Design Manual*. publisher: Microelectronics Development Laboratory Sandia National Laboratories. Oct. 2012. URL: https://www.sandia.gov/mesa/_assets/documents/design_documents/SUMMiT_V_Dmanual.pdf.

[51] Aaron Partridge and Markus Lutz. *Episeal pressure sensor and method for making an episeal pressure sensor*. US Patent 6,928,879. Aug. 2005.

[52] Rob N Candler, Matthew A Hopcroft, Bongsang Kim, Woo-Tae Park, Renata Melamud, Manu Agarwal, Gary Yama, Aaron Partridge, Markus Lutz, and Thomas W Kenny. "Long-term and accelerated life testing of a novel single-wafer vacuum encapsulation for MEMS resonators". In: *Journal of Microelectromechanical Systems* 15.6 (2006), pp. 1446–1456.